

An *Akouemma hemisphaeria* Organic Macrofossils Colony Hosting Biodiversity Assemblage on the Seafloor of Okondja Basin (Gabon) dated at 2.2 Ga

Edou-Minko A^{1*}, Moussavou M¹, Sato T^{2*}, Tchikoundzi C¹, Sawaki Y³, Ndong Ondo S¹, Ortega R⁴, Maire R⁵, Kaestner A⁶, Mbina Mounguengui M¹, Roudeau S⁴, Fleury G⁷, Carmona A⁴, de Parseval PH⁸, Makaya Mvoubou¹, Musavu Moussavou B¹, Ogandaga Agondjo M¹, Sasaki O⁹ and Maruyama S²

¹Université des Sciences et Techniques de Masuku, BP. 901 Franceville, Gabon

²Earth-Life Science Institute (ELSI), Tokyo Institute of Technology, 2-12-1 O-okayama Meguro-ku, Tokyo, Japan

³Department of Earth and Planetary Sciences, Tokyo Institute of Technology, 2-12-1 O-okayama Meguro-ku, Tokyo, Japan

⁴CENBG, Univ. Bordeaux, CNRS, IN2P3, UMR 5797, F-33170 Gradignan, France

⁵UMR 5319 Passages, Maison des Suds, CNRS-Université Bordeaux-Montaigne, France and Honorary Research Fellow, University of the Witwatersrand, Johannesburg, South Africa

⁶Laboratory for Neutron Scattering and Imaging, Paul Scherrer Institut, CH-5232 Villigen - PSI, Switzerland

⁷Muséum d'Histoire Naturelle de Toulouse, 35 Allée Jules Guesde, 3100 Toulouse, France

⁸Géosciences Environnement Toulouse (GET), Observatoire de Midi-Pyrénées Université de Toulouse, CNRS, IRD, 14 Avenue Edouard Belin, F-31400 Toulouse, France

⁹Tohoku University Museum, Université de Tohoku, 6-3 Aoba, Aramaki, Aoba-ku, Sendai, Japan

Abstract

A colony of silico-carbonate *Akouemma* nodules found in Akou River sedimentary formations of the Palaeoproterozoic Okondja Basin consists of two groups, spheroidal (ovoid) nodules and elongated nodules. These nodules, which consist of two hemispheres separated by a median disc, are composed essentially of micro-quartz associated with calcite of extra-polymeric substance (EPS) type, clay minerals, organic carbon and oxides and sulphides of iron. They contain tubular microfossils, pluricellular clusters, microorganisms and vesicles, and have undergone considerable deformation by mutual lateral compression in tabular beds. They were interpreted as biogenic nodules hosting microorganisms.

We provide the following additional supporting evidence: *Akouemma* nodules exhibit internal fibro-radial fabrics initially composed of fibres and carbon particles; the initially well-organized structures are decaying and are in particles and fragments that are dispersed in the undeformed siliceous mass. These internal fabrics are strongly highlighted by Al- K- (Ti)-rich clay minerals that are often in close association with fibres and carbon particles. They had likely a vegetative reproduction by duplication.

We infer that the *Akouemma* nodules are macrofossils of sessile soft-plastic body organisms. These macrofossils, recently dated at 2.2 Ga, are designated "*Akouemma hemisphaeria*" and bring a new vision to the "large colonial organisms" found in the Franceville Basin.

Keywords: Macrofossils; *Akouemma hemisphaeria*; Internal fibro-radial carbon; K-rich clay mineral; Syn-sedimentary deformation; Microorganisms; Palaeoproterozoic; Okondja basin; Gabon

Introduction

The sedimentary formations of the Francevillian Group of Gabon are very well preserved and are among the few non-hydrothermal, non-metamorphic Palaeoproterozoic formations in the world. The FB Formation of the Francevillian Group is characterized by smectite/illite-rich clay minerals that are both randomly ordered and ordered, suggesting a low grade of diagenesis [1]. These formations contain a biodiversity of micro- and macrofossils [2-8], and current research shows macrofossil-like material distributed from FB1 to FD in the Francevillian Group (Franceville, Lastourville, Okondja and Booué Basins) including specimens from the Akou River in Okondja Basin (Figure 1).

The Okondja Basin is one of four Francevillian Basins (Figure S1) in which deposits are marked by a high abundance of organic matter. Its fossiliferous FB2b formations, dated at 2.2 Ga [9], are composed of repeated alternations of sandstones, basaltic lavas, siltstones, pyroclastic sandstones, black shales and mafic intrusions [10] (Figure 1). These basins exhibit highly negative $\delta^{13}\text{C}_{\text{org}}$ values ranging between -21 and -46‰ [11-13] and $\delta^{13}\text{C}_{\text{carb}}$ values of diagenetic carbonate nodules and carbonate formations between -7 and 10‰ [6,14] with highly positive values being observed in the dolomitic carbonate formations of the Lastourville Basin [6].

We report remarkably preserved nodules (7-62 mm in length and 7-33 mm in diameter) localized near the top of subunit FB2 at the Akou River to northeast of Okondja (Figure S1). One hundred and ten specimens were the subject of a statistical, mineralogical and geochemical study. These nodules, consisting of two hemispheres with a median zone (Figures 2A-2k and 3A-3F) and designated *Akouemma*, have an essentially siliceous composition with more than 80% homogeneously distributed micro-quartz; other elements, such as Fe (9%) in the sulphated and oxidized form, Ca (3%) in the form of calcite, Al (7%) K (0.3%) and Ti (0.1%) of the clay minerals pole quite clearly

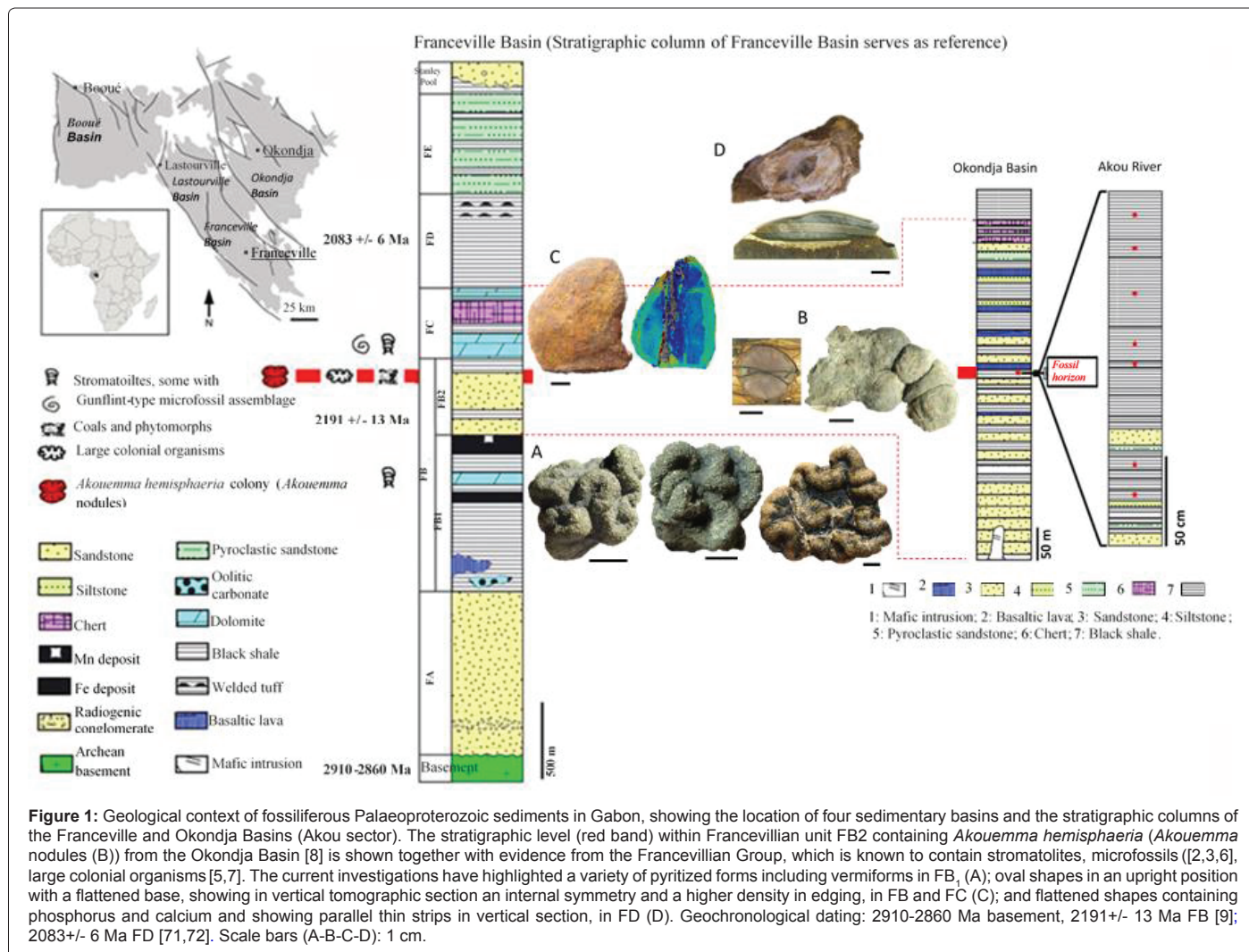
***Corresponding author:** Edou-Minko A, Université des Sciences et Techniques de Masuku, BP. 901 Franceville, Gabon, Tel: +24107173341; E-mail: edouminko@gmail.com

Sato T, Earth-Life Science Institute (ELSI), Tokyo Institute of Technology, 2-12-1 O-okayama Meguro-ku, Tokyo 152-8551, Japan, Tel: +81357342283; E-mail: sato.tbq@m.titech.ac.jp

Received January 19, 2017; **Accepted** February 06, 2017; **Published** February 10, 2017

Citation: Edou-Minko A, Moussavou M, Sato T, Tchikoundzi C, Sawaki Y, et al. (2017) An *Akouemma hemisphaeria* Organic Macrofossils Colony Hosting Biodiversity Assemblage on the Seafloor of Okondja Basin (Gabon) dated at 2.2 Ga. J Geol Geophys 6: 281. doi: [10.4172/2381-8719.1000281](https://doi.org/10.4172/2381-8719.1000281)

Copyright: © 2017 Edou-Minko A, et al. This is an open-access article distributed under the terms of the Creative Commons Attribution License, which permits unrestricted use, distribution, and reproduction in any medium, provided the original author and source are credited.



highlight the internal fabric [8]. They present negative $\delta^{13}\text{C}_{\text{org}}$ values ranging from -26 to -37‰, negative $\delta^{13}\text{C}_{\text{carb}}$ values of -17 to -26‰ and $\delta^{34}\text{S}_{\text{pyr}}$ values of -7 to 18‰, with most being higher than 7‰ [8]. These values suggest calcite precipitation and pyritization of organic matter via bacterial activity in a closed and reduced environment [15].

Materials and Methods

The geological objects under study are *Akouemma* nodules from the Okondja Basin [8], and the main analyses of these nodules are described below.

SEM-EDS

Scanning electron microscopy-energy dispersion X-ray spectrometry (SEM-EDS) analyses were performed on Os-coated samples using a Hitachi S-3400N SEM with a Bruker Xflash 5010 at the Tokyo Institute of Technology to investigate the distribution of elements such as carbon, aluminum, potassium, and iron. Measurements were performed under an accelerating voltage of 15 kV. Complementary analyses were performed with a JEOL 6360LV SEM and a Bruker SDD XFLASH 5010 at the GET of Toulouse.

PIXE analysis

Nuclear microprobe analysis using PIXE (particle-induced X-ray

emission) enables quantitative imaging of the distribution of chemical elements in various types of materials, including complex geological samples. In addition, the combination of PIXE and RBS (Rutherford backscattering spectrometry) allows full quantification of the concentrations of these chemical elements, expressed as grams of trace element per gram of sample at the micrometre level [16]. A thick section of sample AKOU16 was analysed using a PIXE microprobe at CENBG (Bordeaux Gradignan). A 1.775-MeV proton beam was employed not only to provide information on the distribution of chemical elements with atomic number >11 using PIXE but also to enhance the carbon RBS signal through carbon resonance at 1.75 MeV. The proton beam was focused down to 2 micrometres on the surface of the sample to achieve an intensity of 500 pA and then raster scanned to allow chemical imaging of $1.2 \times 1.2 \text{ mm}^2$ regions of the sample. Chemical maps were recorded in a 256×256 pixel matrix, resulting in a spatial resolution of $4.6 \mu\text{m}/\text{pixel}$. In the case of the AKOU16 fossil, 393 square zones of $1.2 \times 1.2 \text{ mm}^2$ each were analyzed to cover the entire section of the specimen (approximately 576 mm^2). Higher spatial resolution maps were also generated for specific areas such as carbonate-rich regions; in this case, a smaller beam ($0.8 \mu\text{m}$) with a reduced intensity (180 pA) was used for scanning, employing a 256×256 -pixel matrix in regions with a maximum area of $0.2 \times 0.2 \text{ mm}^2$, thus achieving the highest spatial resolution of the setup ($0.8 \mu\text{m}$). Distribution maps for Al, Si, S,

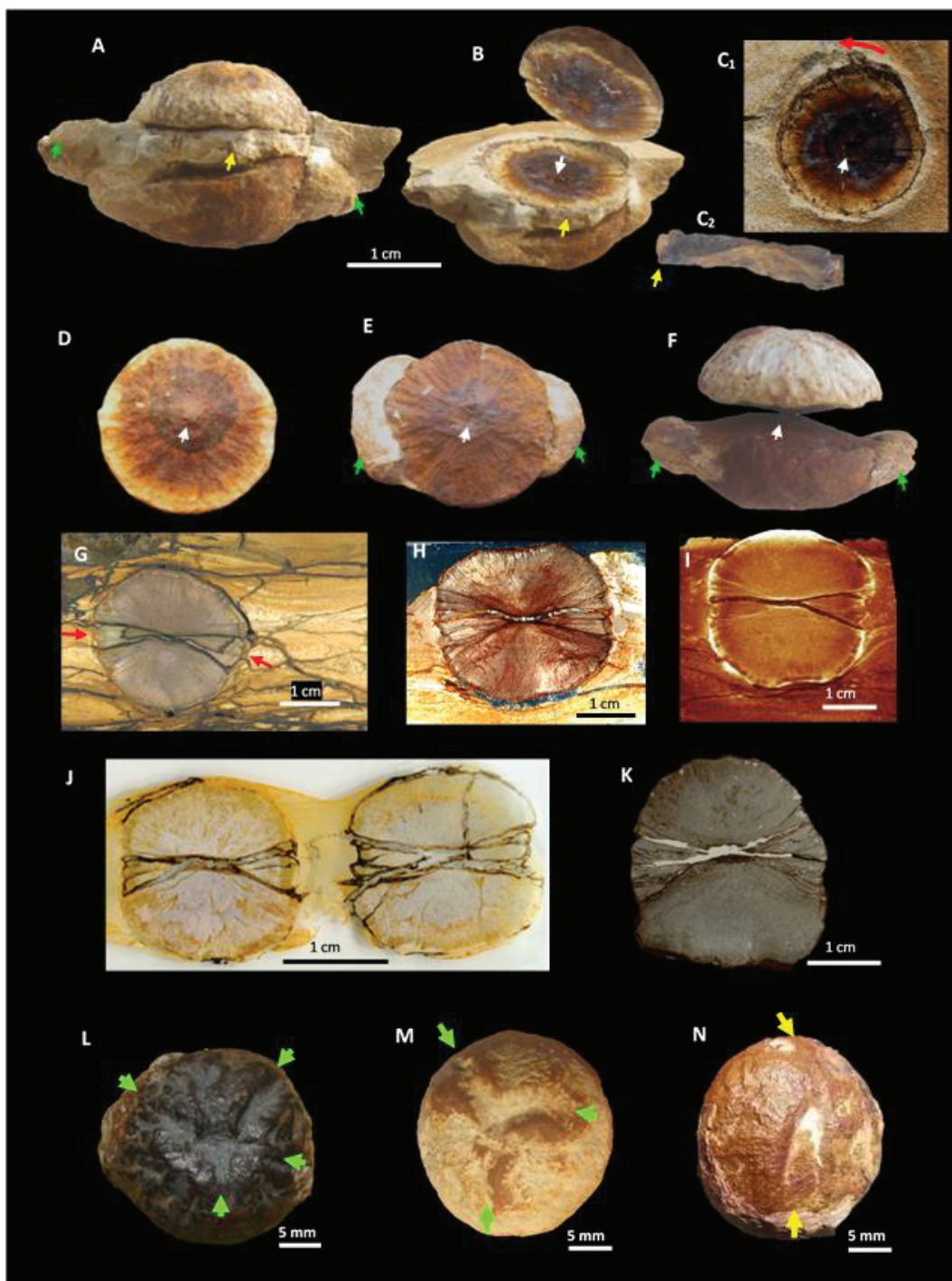


Figure 2: Morphology and internal structure of *Akouemma* nodules showing ovoid forms. (A) Complete-type specimen showing a nodule displaying a distinct median disc plus a surrounding mudstone matrix (green arrow). (B) Same specimen with the upper hemisphere raised to show the internal surfaces of the upper hemisphere and the median disc; note the central orifice on the median disc (white arrow). (C₁) View of a sedimentary plate containing a nodule in the plane of the median disc; note the central orifice in the median disc (white arrows) and the peripheral arrangement of repeated patterns (approximately 250 μ m each) on the border of the nodule and in the sediment (probable form of microbially-induced sedimentary structures (MISS) red arrow). (C₂) Profile view of the median disc; note its thickness, which decreases from the border towards the centre. (D) Internal surface of an upper hemisphere, showing radial sculpture and a central nipple-like feature. (E) Internal surface of a lower hemisphere, showing radial sculpture and a corresponding central depression. (F) Superposition of the two hemispheres at the central nipple-like feature and the corresponding central depression (likely communication point between hemispheres); note the empty space left by the median disc; (Figure S3E-S3K). (G-K) Vertical section views of five typical specimens consisting of two hemispheres and a median disc. (G) Polished plate; note the iron lines on the median disc (white arrow). (H) Thin section showing the median disc glued at the hemispheres; note the corrugated secondary crack. (I) Tomographic view showing the cracks delimiting the median disc. (J) Thin section containing two fairly similar undeformed specimens (1 and 2) with two hemispheres and a medial zone; the medial zones are very fragile, with lateral secondary cracks. (K) An isolated deformed nodule with a flattened and wave-like base (Figure S7); note the development of secondary cracks in the median disc, which was initially attached to the hemispheres (OKO 2). (L-N) Views of the top hemispheres of three nodules showing (L-M) depressions around the top (green arrows); (N) a wide dimple on the top (yellow arrows).

K, Ca, Ti, Mn, and Fe were obtained through PIXE analysis, and carbon and oxygen concentrations were determined simultaneously through RBS analysis. The quantification procedure was validated based on U.S. Geological Survey Geochemical Reference Materials BCR2 (Basalt, Columbia River) and BIR1 (Icelandic basalt).

Laboratory-based computed tomographic (CT) analysis

For sediment-enclosed nodules, data were acquired using a General Electric LightSpeed CT scanner with 0.5 mm thick slices. For single nodules and specific areas, data were acquired with a Carl Zeiss Nanotom and a Carl Zeiss Metrotom, with slice thicknesses varying from 17 μm to 70 μm depending on the size of the selected areas and the type of CT equipment. All CT and micro-CT datasets were exported using the DICOM export file format to ensure the best image quality and inter-operability, and the 2D and 3D images from the CT and micro-CT DICOM stacks were processed on a Dell Precision T7400 Dual Quad Core Intel Xeon 3.2 GHz workstation using 32 GB of DDR RAM and a Quadro FX 4600 graphics board running VG Studio Max 2.0 and 2.2×64 from Volume Graphics GmbH.

Complementary micro-CT analyses for X-strata were performed with a Micro-XCT-400 system at Tohoku University. All strata were photographed using a MOLCER 3D image viewer.

Neutron tomography

Neutron tomography is a transmission imaging technique in which neutrons are used as a radiation source to produce the radiographs required as projections to reconstruct a three-dimensional image of a sample [17]. Neutrons interact differently with matter than X-rays, and for many elements the two modalities provide completely different attenuation coefficients. Typically, neutrons are sensitive to low-atomic number elements such as hydrogen and lithium, whereas many high-atomic number elements exhibit lower attenuation. Neutrons have the ability to discriminate between different isotopes of the same element. The difference in attenuation coefficients means that neutron imaging serves as a relevant probing method for palaeontological and geological samples [18]. However, neutron imaging is a less common imaging method than X-ray CT because few strong neutron sources are available worldwide; the neutron flux required to obtain a good image quality requires either a research reactor or a spallation neutron source. This investigation was performed at the Paul Scherrer Institut using the ICON cold neutron imaging beam line [19]. The CT data were acquired using the micro-tomography setup [20], which has a field of view of $27 \times 27 \text{ mm}^2$ and a pixel size of 13.5 μm . A 20- μm -thick Gadox scintillator was employed to convert the neutrons into visible light, which was captured using a cooled CCD camera (Andor DW436). The data were reconstructed using Octopus CT reconstruction software in parallel beam mode, which results in a valid approximation due to the high collimation of the neutron beam. This procedure provided CT datasets with 13.5- μm cubic voxels, which were saved as TIFF images. Kiptool software (Paul Scherrer Institut) was then used for 3D image processing, and final visualization, rendering and animation were performed with Drishti 2.5.1 software.

Results

Akouemma specimen morphology

The spheroidal (ovoid) specimen type measures an average of 2 cm in diameter and consists of two hemispheres separated by a disc-shaped central zone designated the "median disc" (Figures 2A-2C and 2G-2K). Each hemisphere has a central cone, and the median disc

has a central orifice [8] (Figures 2B, 2C₁ and 2D-2E and Figure S3I-S3K₁). The internal surfaces of the upper hemisphere show a central nipple-like feature, and those of the lower hemisphere may show a corresponding depression (Figure 2D-2E and Figure S3E-S3K). The tripartite spheroidal shapes are similar and represent more than 60% of specimens. They sometimes have a flattened base (Figure 2K) with different structures at its edge (Figure S7B-S7I).

Elongated forms represent approximately 40% of the population. They have a diameter similar to that of the spheroidal shapes; the maximum length measured on the axis of elongation barely exceeds 6 cm (Figure 3). These specimens appear in the form of elongated nodules in a single piece (Figure 3A-3D) and in the form of elongated nodules with two or three segments [8] (Figure 3E-3G). They tend to have a bipartite structure with two hemispheres separated by a continuous median surface and a barely visible median disc at the ends of the nodule. Central nipple-like features or corresponding depressions are sometime visible on the median surface (Figures 3D₂, E₂ and 4D₁). Their external cortex, which is generally continuous on each hemisphere, is often marked by one or two external furrows that are more or less deep and are oriented perpendicular to the direction of elongation (Figure 3A-3G). The transition from spheroidal to elongated forms is progressive (Figure S2) [8].

The nodules occur in isolation (Figures 2G-2I and 5), relatively distant from each other, near each other (Figures 2J, 4A and 5), or in groups (Figures 4 and 5). When present as a group, the nodules are deformed along a bedding plane (Figures 4A and 5). Some nodules exhibit strong volume reduction and lateral spreading of matter (Figures 4E-4I and 5E-5H), distortion and rotation of hemisphere and median disc (probably around of the 'communication point'), micro-folding (Figures 4J-4K and 12C-12C₃), and vertical flattening due probably to burial compaction (Figure 4B-4C). In AKOU 16 and AKOU 35 nodules only upper hemisphere is flattened, with deformation of the sediment under AKOU 35 nodule (Figures 3B, 11 and 12A-12A₁).

External and internal organization

The external organization around the *Akouemma* specimens is discrete but complex. Macroscopic observations indicate that the surfaces of these specimens are marked by changes in relief and by a number of depressions and grooves ranging from a few millimetres to approximately a centimetre in size (Figure 2L-2N and Figure S3A-S3D). These surface structures do not exhibit a precise geometrical organization but are often aligned and rectilinear in form, and the alignments are formed by lenticular bodies ranging from a few tens of micrometres to >650 μm long. They can be siliceous, ferruginous, or formed from clay minerals, sometimes with relics of organic carbon (Figure 3A-3A₁ and 4K-4L and Figures S5, S6A, 5A₂, and 5A₄-5A₈). Four examples of peripheral 'encrustation' bodies are observed. Three similar examples are located on the surfaces of the upper hemispheres (Figure 3A-3A₁ and Figures S5A-S5A₁, S5B-S5B₁ and S6A, S6A₂), and one is observed at the periphery of a compressed medial disc (Figure 4K-4L), with local deformation of the nodule under the lenticular body. SEM-EDS analyses confirm also the existence of Al-K-rich lenticular bodies inside and along the edges of nodules and display their internal and peripheral alignment (Figure 9O₄ and 9P₄). Alignments of repeated patterns are also observed in the sediment and around nodules (Figures 2C₁ and 4E).

The internal organization of the nodules is essentially radial. Macroscopic samples (Figures 2B-2F, 4D₁ and 8A), scanned vertical sections (Figures 2G-2H, 2J-2K, 3A-3C, 3E₁, 3F₁, 4J-4L and 9A₁-9A₂),

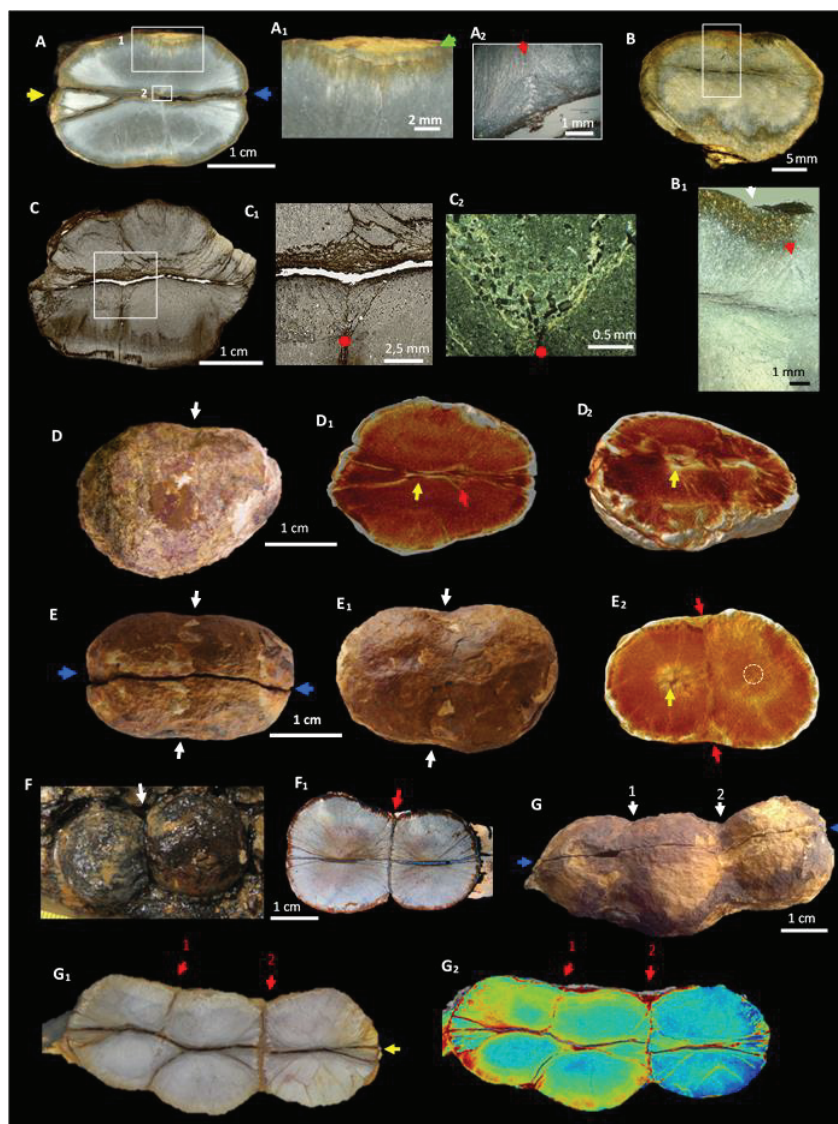


Figure 3: Morphology and internal structure of *Akouemma* nodules showing elongated forms. (A) View of an axial vertical section showing an altered border (white box 1), internal zone (white box 2) and a slight depression on the edge (white arrow); the blue arrow indicates the internal surface, and part of the median disc is indicated by the yellow arrow. (A₁) Detailed view of white box 1 in 'A' showing a yellow lenticular form (probably clay) embedded in the nodule; note the deformed zone of the nodule under the lenticular body (green arrow). (A₂) Detailed view of white box 2 in 'A' showing internal polygonal structure (red arrow) formed by abutting radial calcite bands; also seen are small radiating 'channels' filled with clay mineral and small secondary quartz grains. (B) View of a polished section showing an elongated nodule with a flattened upper hemisphere; the internal median surface is barely visible (AKOU-16). (B₁) Thin-section detailed view of the white box in 'B' showing an internal polygonal structure (red arrow) and a slight depression on the edge (white arrow) on elongated nodule AKOU-16; for more details see Figure 11. (C-C₂) View of an axial vertical section of the AKOU 14 nodule showing its internal polygonal structure (white box) and a median zone with curved lamellae. (C₁) Detailed view of the white box in 'C' showing a more-or-less degraded internal polygonal structure (red arrow). (C₂) Thin section showing internal polygonal structure formed by abutting clay mineral channels filled with opaque minerals of pyrite and iron oxides (the red dot serves as a reference). (D-D₂) Different external and internal aspects of *Akouemma* elongated nodule in a single piece: (D) Top view of the hemisphere showing a slight depression on the edge (white arrow); (D₁) Tomographic view of the vertical section of the same nodule showing two hemispheres separated by the median disc, note the communication point probable between the two hemispheres (yellow arrow) and the internal polygonal structure (red arrow); (D₂) Tomographic view of the lateral section at the median disc of the same nodule showing a central depression on the cone (yellow arrow). (E-E₂) Different external and internal aspects of *Akouemma* elongated nodules with two "segments". (E) Macroscopic view of the elongated nodule showing two hemispheres separated by a median surface; note the shallow furrow around the nodule (white arrow). (E₁) Top view of the upper hemisphere clearly showing the furrow perpendicular to the elongated axis of the nodule. (E₂) Tomographic view of lower hemisphere; view of the horizontal section parallel to the median surface showing the suture between two "segments" that connects the edge furrow, note a central depression in the left "segment" (yellow arrow), it is barely visible in the right "segment" (dotted circle). (F-F₁) Different external and internal aspects of *Akouemma* nodules with two "segments" or a "double nodule". (F) Macroscopic view of the top of the "double nodule" in the field showing two "attached nodules"; note the deep furrow that separates them. (F₁) Vertical section of the same sample through two conjoined specimens showing weathered margin, radial fabric and median sutures; note the polygonal structures on either side of the suture. (G-G₂) Different external and internal aspects of the elongated *Akouemma* nodule with three "segments". (G) Macroscopic view of the elongated nodule showing two hemispheres separated by a median surface (blue arrows); note the two furrows, one of which is shallow (furrow 1) and the other fairly deep (furrow 2) around the nodule (white arrows). (G₁) Vertical polished section of the same nodule showing two sutures, one is slightly developed (suture 1) and draws an incomplete limit between the "segments", and the other is more developed (suture 2) and shows a sharper limit between the "segments"; note the polygonal structures on either side of each suture. (G₂) Tomographic view of the vertical section of the same nodule showing the sutures between the three "segments" with net separation of "Father" specimen on the right; see also Figures S2, S23.

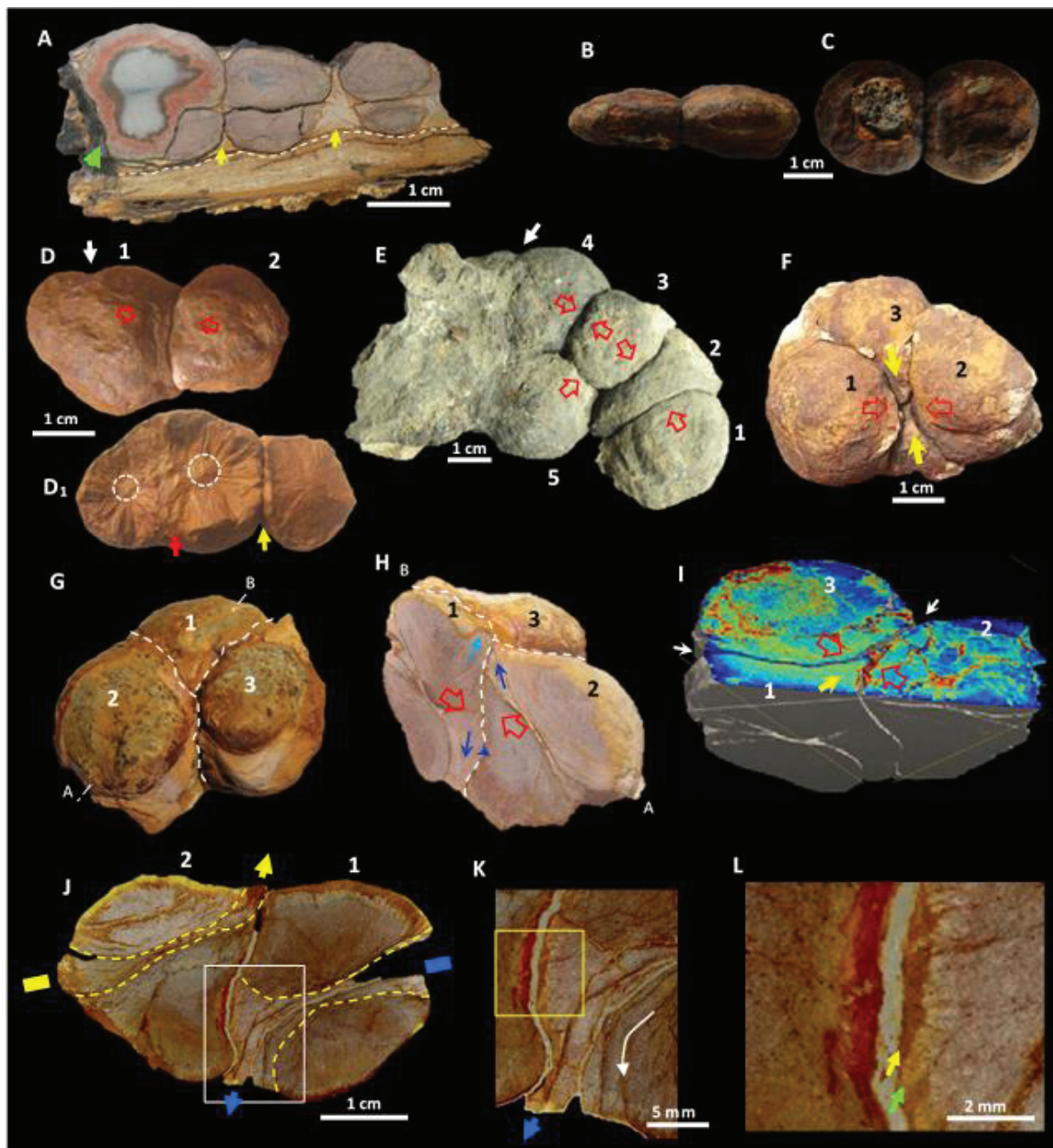


Figure 4: Morphology and internal structure of deformed *Akouemma* nodules. (A) View of a vertical section of three spheroidal nodules that are more or less weathered in sediment; two are adjoined with deformed contact surfaces and one is an isolated nodule; compacted sediment is visible between the nodules (yellow arrows). The green arrow shows a crushed contact surface; note the low ripple sediment below the nodules (dotted lines). (B-C) Macroscopic views of two joined and flattened specimens in (B) side view and (C) polar view; they seem to be covered by an 'envelope'. (D) Macroscopic view of two mutually laterally compressed specimens with elongated (1) and spheroidal (2) shapes; note the deformed contact between them (yellow arrow) and the continuity of the cortex of the elongated shape, which is marked by a slight depression (white arrow); and in (D₁), by an internal suture between two radial discs (red arrow); note the central nipple-like features on the elongated shape (dotted circle); note the difference between these two adjoined nodules and the "triple nodule" (Figure 3G-G₂). (E) Macroscopic view of five mutually laterally compressed and intensely compressed specimens contiguous with specimen (2) in the form of a 'T'; note the aligned patterns on the sediment and the curve limit between sediment and nodule parallel to the aligned patterns (white arrow). (F) Three contiguous and deformed specimens; the medial zone of nodule 3 in the middle is strongly compressed (yellow arrows). (G-L) Three other contiguous and deformed specimens. (G) Together, the three nodules present deformed contact surfaces (dashed white line). (H) Vertical section of two specimens with a highly deformed contact surface; the blue arrows indicate the direction of deformation, note the folded and raised border of nodule 1 (clear blue arrow). (I) Tomographic view of the same specimens; note that the upper hemisphere of specimen 1 is pinched between specimens 2 and 3 (yellow arrow). (J) Vertical section of the same nodules (macroscopic view) showing the deformation of the medial disc and the two hemispheres; after deformation, the median discs, which are usually in a more or less horizontal position (yellow and blue bars), are offset downward toward specimen 1 (blue arrow) and upward toward specimen 2 (yellow arrow). (K) Detailed view of the white box showing the deformation of the medial disc and the lower hemispheres; note the bending (white arrow) and dissolution of the rods of the median disc (yellow arrow). (L) Detailed view of the yellow box showing a ferruginous lenticular body (yellow arrow) with a deformed band beneath it (green arrow), similar to Figure 2A₁. The red arrows indicate the direction of mutual lateral compression.

optical microscopy (Figures S9A, S10, S11A), laboratory-based CT analysis (Figures 2I and 3D₂), nuclear microprobe analysis, energy-dispersive X-ray spectrometry and scanning electron microscopy of the distribution of chemical elements (Figures 9B₁-9S₅, 11C-11H, 12B-12C, 13 and 14 and Figures S4, S5, S6, S15-S18 and S20-S22), neutron tomography (Figure 10) revealed a highly organized initial structure in the *Akouemma* nodules in the form of a centrifugal fibro-radial and fabric.

The relatively simple system of spheroidal forms consists of a radial fabric of filaments and particles arranged centrifugally downwards in the lower hemisphere, upwards in the upper hemisphere and laterally in the median disc [8] (Figures 2G-2K, 9,10 and Figure S4).

In detail, it consists of:

1. a more or less homogeneous cone that constitutes the origin of the fan-shaped radial system (Figure 9B₁, 9C₁ and 9D₁);
2. a ramification zone (or development zone of the fan-shaped radial system) where the structuring of tufts begins, alternating with the zones of end tufts (Figure 9E₂-9J₃ and Figure S13);
3. a fan-shaped border zone (Figure 9K₄-9P₄);
4. a median zone consisting of rods arranged around the cones of the hemispheres to form the median disc, which is remarkable for its central orifice (Figure 9Q₅, 9R₅ and 9S₅ and Figure S4).

The fibro-radial fabric of elongated forms is more complex. The single-piece elongated shapes exhibit a polyphase internal fibro-radial system containing a mostly internal polygonal structure that likely form a junction (suture) between two single radial fabrics (Figures 3A, 3A₂, 3B-3B₁, 3C-3C₁, 3E₁, 3F₁-3F₂; 11C-11H, 12A-12A₁ and 12B-12B₃). In elongated forms with two or three segments (double or triple nodules), each segment consists of an internal fibro-radial fabric (Figures 3F₁, 3G₁ and 12B-12B₃). The elongated forms also display at their junctions a more-or-less-developed polygonal structure on either side of the median surface and a vertical suture that connects the outer furrow. We note that the more developed the polygonal structure, the deeper the outer furrow and the more obvious the internal suture that separates two 'segments' until individualization of the spheroidal bodies (Figure 3 and Figure S23). The polygonal structure, the outer furrow and the vertical suture would correspond to a phase of division.

Just as spheroidal nodules and undeformed nodules (in single, double or triple nodules) have non-deformed structures (fibro-radial fabrics) (Figures 3, 5, 9, 11 and 12B-12B₃ and Figures S4, S23), the deformed and laterally compressed nodules have deformed internal structures (fibro-radial fabrics) (Figures 5, 12A-12A₁, 12C-12C₃, 13L₃, 13P₅, 14J₈, 14N₉ and Figure S5B₁), essentially recorded in the distribution of Fe, (Ca), and (Ti)-K-Al-rich clay minerals.

Mineralogy and microorganisms

The *Akouemma* nodules exhibit a relatively simple mineralogy consisting mainly of micro-quartz and secondarily of oxides and sulphides of iron, organic carbon, calcite, and clay minerals including kaolinite clay, chlorite-vermiculite (K-rich clays), and lepidocrocite (Ti-rich clay) [8]. In non-deformed specimens, these minerals are arranged according to the radial system (Figures S6A-S6A₃, S7B-S7C, S8B₁-S8B₂, S9A, S10 and S11A) and crystallize in the deformed zones according to those structures (Figure 4J-4L). Micro-quartz represents over 80% of the mass and is homogeneously distributed in the specimen as grains 2 to 5 μm in size (Figure S7C-S7E), which are locally associated with macro-quartz greater than 30 μm in diameter (Figure S10E, G, and H).

Iron oxides and sulphides, calcite, clay minerals and organic matter make up less than 20% of the mass, and it is these "secondary" minerals that largely highlight the internal radial fabric of the nodules, showing its alignment, which may be continuous over a distance of 0.5 mm in the radial direction (Figures S10C and S11A) [8]. This orderly organization sometimes gives way to broken fragments dispersed in an undisturbed siliceous mass (Figure S11B). Other well-organized rows of Si-Al-Fe cell-like structures (2-5 μm in size) are disrupted with the dispersion of cell-like features in the homogenous siliceous mass (Figure S11C). Carbon particles (~5 μm) can be trapped in black "cubes" surrounded by iron in the oxidized form (Figure S7B, G-I); these iron oxides can completely replace the organic particles, and this association of iron and organic carbon may contain relatively high values of Al and Si (Figure S7I₁-S7I₃). Other carbon particles are trapped in siliceous "bricks" alongside red spherules (Figure S8G-S8H). Oxidation (and silicification) of "pyrite crystals" with bristling surfaces seems to lead to the formation of "cubes" and "bricks" with surfaces bristling with orange to orange-yellow particles, and sometimes spreading of particles (Figures S7K-S7K₂, S8B₁-S8H). Ferro-silico-aluminous spherules 2-5 μm in size and ranging in color from grey to yellow-orange to red are packaged in pockets with a thin film of silica (Figure S9C, S9D, and S9E) [8] or in 'bricks' with a siliceous outer wall, where they are arranged in a regular fashion (Figures S8E-S8H, S9F-S9N). The internal 'brick' walls are lined with a thin border of more ferruginous spherules (Figure S9I-8L). The contact between the "brick" and the siliceous mass occurs in the form of a rectilinear net with silica platelets arranged parallel to the brick walls (Figure S9J, S9K and S9N), suggesting rapid crystallization of the silica and not crystallization via epigeny. This explains the nearly intact preservation of the internal structures of the nodules.

The *Akouemma* nodules contain a few cells and pluricellular clusters that are reminiscent of an algal prokaryote or eukaryotic organism, tubule (50 μm in diameter) and ring of yellow-orange particles (5-10 μm) ferro-bacteria like, small clusters of coccus-like bacteria, broken and degraded tubules with colours varying from green to red, oblong shape bodies, red cell-like spherules, carbon particles, and a large number of cyanobacteria that produce an EPS-type calcite [8], and tubular filaments similar to Neoproterozoic mineralized tubular microfossils (Figures 6, 7 and 8 and Figures S6A₁, S7G-S7K₂, S8F-S8H, S9A-S9N, S10E-S10H, S11 and S12) [21].

Distribution of chemical elements

Organic carbon and calcium

Organic carbon is generally unevenly distributed both within single nodules and between different nodules, probably as a result of decomposition and mineralization. The maximum carbon content of the *Akouemma* specimens is 6.7%, and the average $\delta^{13}\text{C}_{\text{org}}$ value is -26.9% [8].

Organic carbon occurs in several different forms: a flattened shape with a characteristic organization of repeated patterns and various forms (Figure 13E₁ and Figure S14), including a massive form >500 μm in size (Figure 13G₁ and Figure S14_{bis}) and small encrusted oblong bodies (Figure 14D₆ and 14E₆ and Figure S19), as small-scale aligned carbon particles or filaments (Figures 13J₂, 13N₃, 13R₅ and 14H₇ and Figure S6A₁ and S17C), and as particles with varying degrees of alignment and dispersion in the siliceous mass (Figures 13K₂, 13O₃, 13S₅, 14I₇, 14L₈, 14M₈, 14P₉, and 14Q₉ and Figures S13B, S13F, S16C, S16D, S17C, S18C, S20C, S20D, S21C, S21D, S22C and S22D). Some examples of these carbon masses are encrusted within the specimens

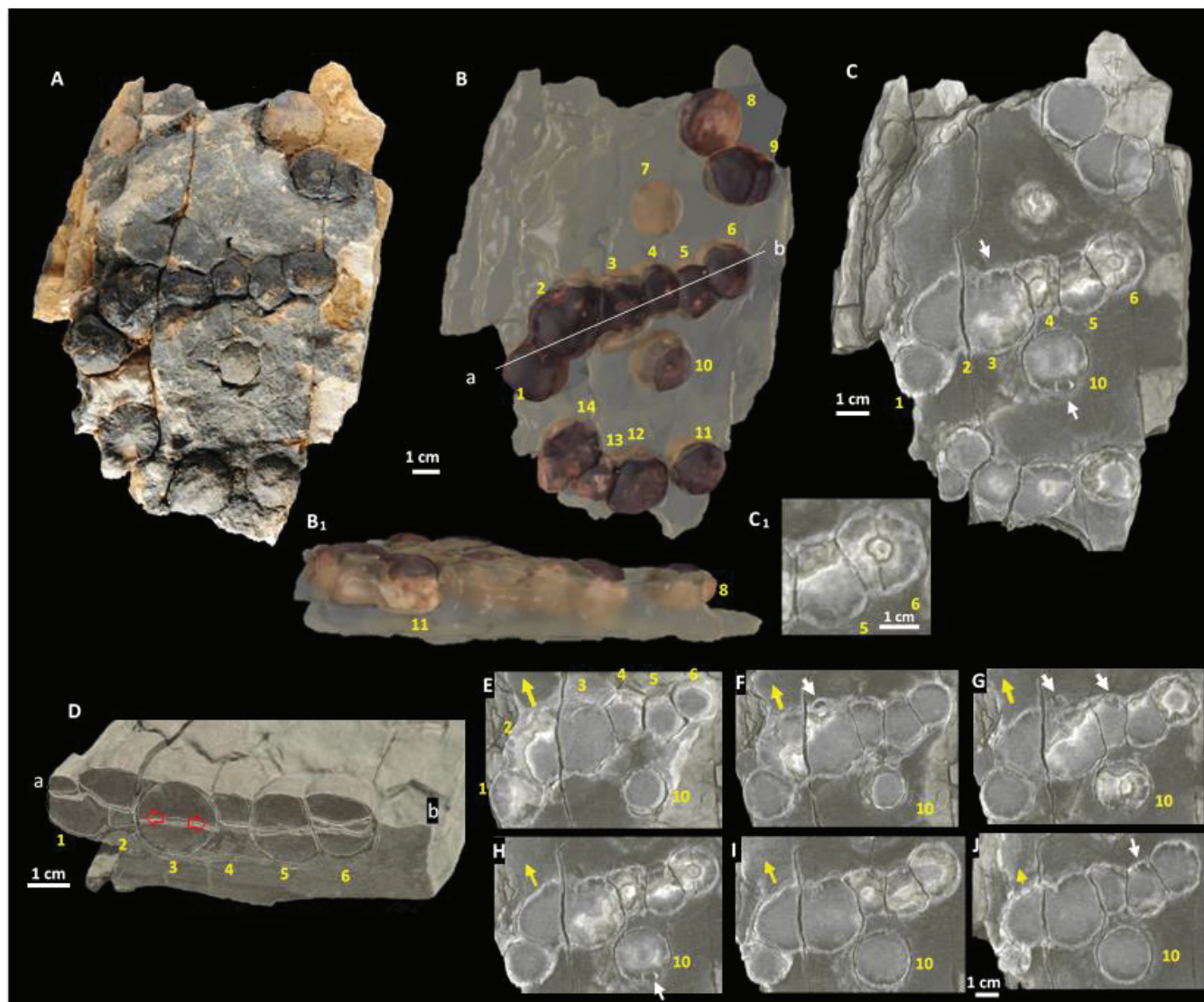
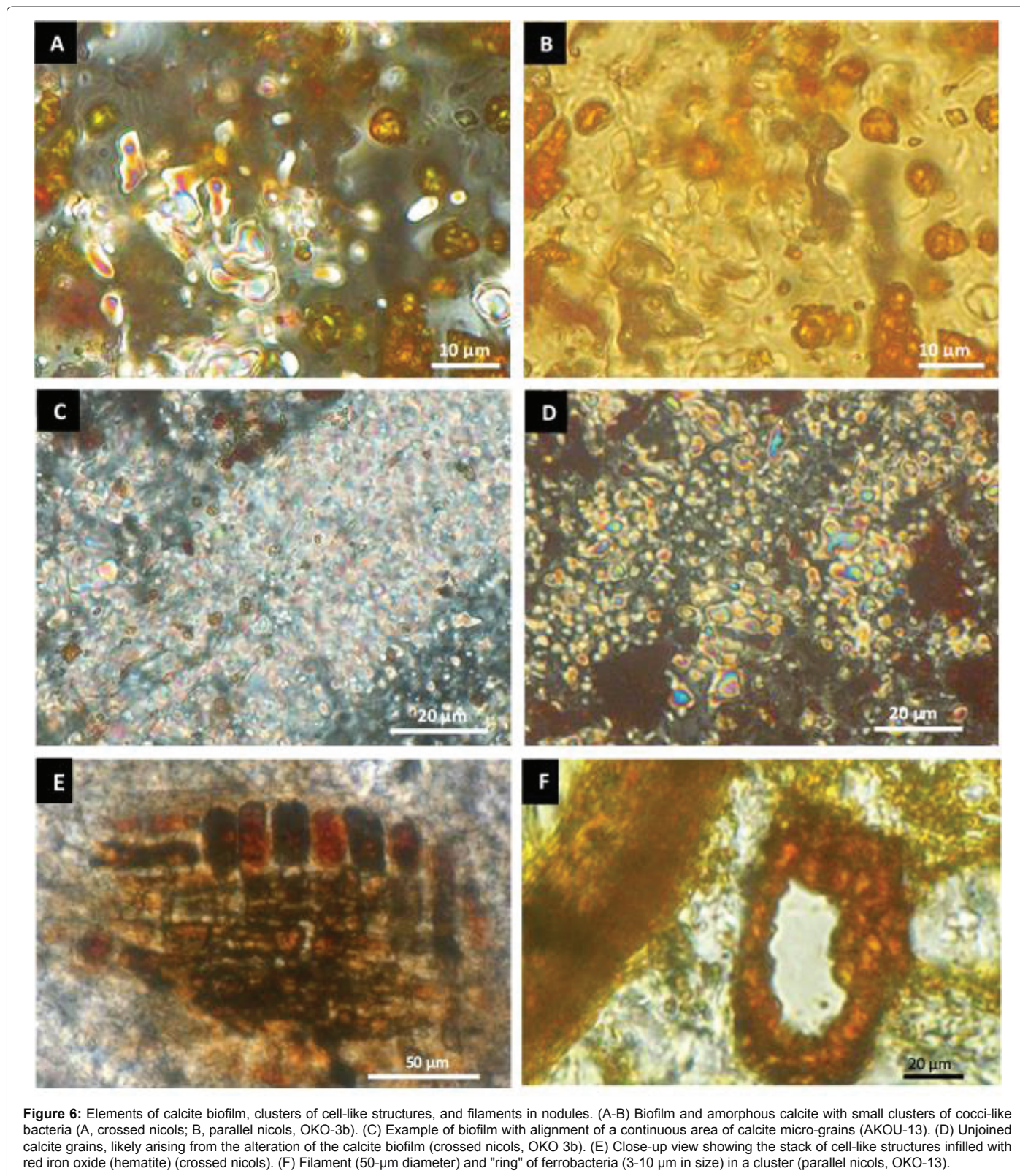


Figure 5: Undeformed tabular sedimentary plate containing undeformed isolated nodules, contiguous nodules, slightly deformed nodules and deformed nodules in a chain. (A) Macroscopic view of the tabular plate (planar, not deformed). (B) Transparent tomographic view of the same plate showing the chain of six joined and deformed nodules (1-6), undistorted isolated nodules (7, 10, 11), and contiguous and only slightly distorted nodules (8-9, 12-14), with a cutting line (ab) on the chain of nodules. (C-C₁) Tomographic view of the lateral section, clearly showing the undeformed nodules and the deformed nodules in the chain and nearby (nodules 1-6, 10); note in (C₁) the truncated median disc of nodule 6 and its central orifice showing the cone of the lower hemisphere with its central depression. (D) Tomographic view of the vertical section (ab) showing the more-or-less intense deformations of the nodules; note the significant reduction in volume of the lower hemisphere of nodule 2, the fan-shaped spreading upward of its upper hemisphere, and the fan-shaped spreading downward of lower hemisphere of nodule 4; much of the lateral constraint would come from nodule 3 (red arrows), well developed and showing no deformation. (E-J) Tomographic view of the lateral sections (top down) of the six nodules in chain and nodule 10; note the lateral spreading of matter within nodule 2 (yellow arrow); the nodule 10, adjoined to the deformed nodules in chain, does not present any deformation and highlights the median disc when moving from the upper hemisphere (E) to the lower hemisphere (J). Note the encrusted "oblong-shaped bodies" bordering the nodules (white arrows).

and show fairly clean contact with them (Figures 13G₁, 14A₁, 14D₆ and 14E₆). In the first example, the carbon mass has a sinuous edge with a rounded contour in the nodule; this latter showing a raised edge at their contact (Figure 13G₁ and Figure S14_{bis}). The second example consists of a carbon mass with an oblong form (Figure 14A₁, 14D₆ and 14E₆ and Figure S19A₁, S19C, S19D and S19E), which is similar to encrusted "oblong-shaped bodies" tomographically and observed on the edges of nodules in chain (Figure 5C, 5F-5H, 5J), to the oblong form highlighted by the potassium distribution map (Figure 12C₂), or to the oblong forms (20-100 μm) that are regularly observed microscopically, sometimes containing red spherules cell-like (Figures S8B₂, S9A-S9E,

S10A, S10C-S10D and S11K-S11L). In some of the compressed zones of the nodules, the linear carbon particles on which "filaments" of Al-K-rich clay minerals are superimposed in the siliceous mass show lateral micro-shearing and lateral stretching of the carbon particles (Figure 13P₅-13S₅ and Figure S18C and S18E).

Calcium is also unevenly distributed between nodules, but it is sometimes uniform within a nodule. The calcium content is approximately 3%, and negative $\delta^{13}\text{C}_{\text{carb}}$ values (-23.87‰ on average) indicate an organic source for the carbon present in the EPS-type calcite [8] (Figure 6A-6D). This calcite is mainly found inside the nodules in the form of micron-sized grains and is relatively poorly correlated with



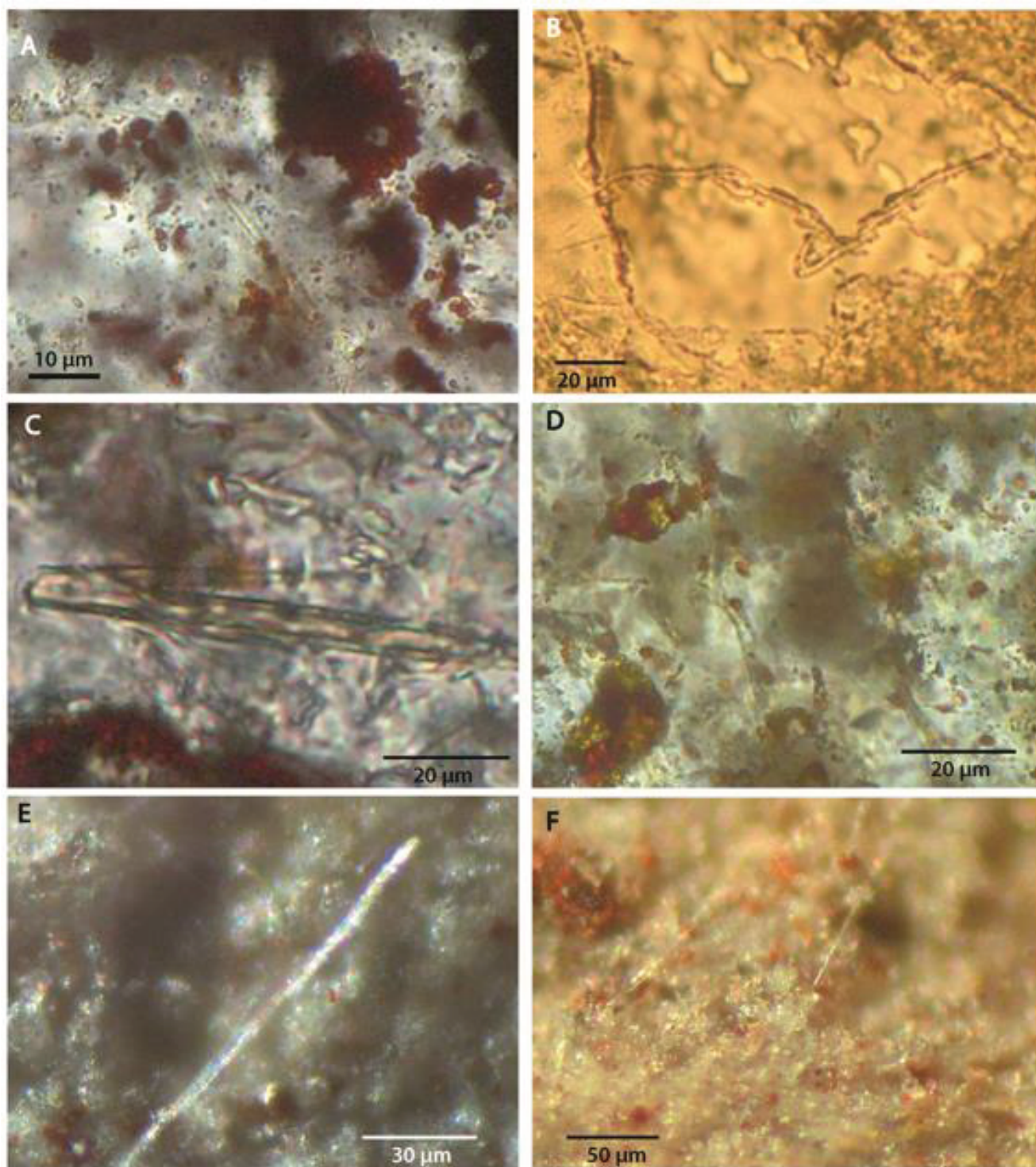


Figure 7: Example of silicified filaments observed in the mass of the chert on four samples. (A) Thin section OKO 1 (not analysed; crossed nicols). (B) Thin section FRA 13 (not analysed; crossed nicols). (C) Thin section OKO 2, tubular filament (not analysed; crossed nicols). (D) Thin section OKO 3b, branched filaments. (not analysed; crossed nicols). (E) Polished surface OKO 3b (reflected light). (F) Polished surface OKO 3b (reflected light).

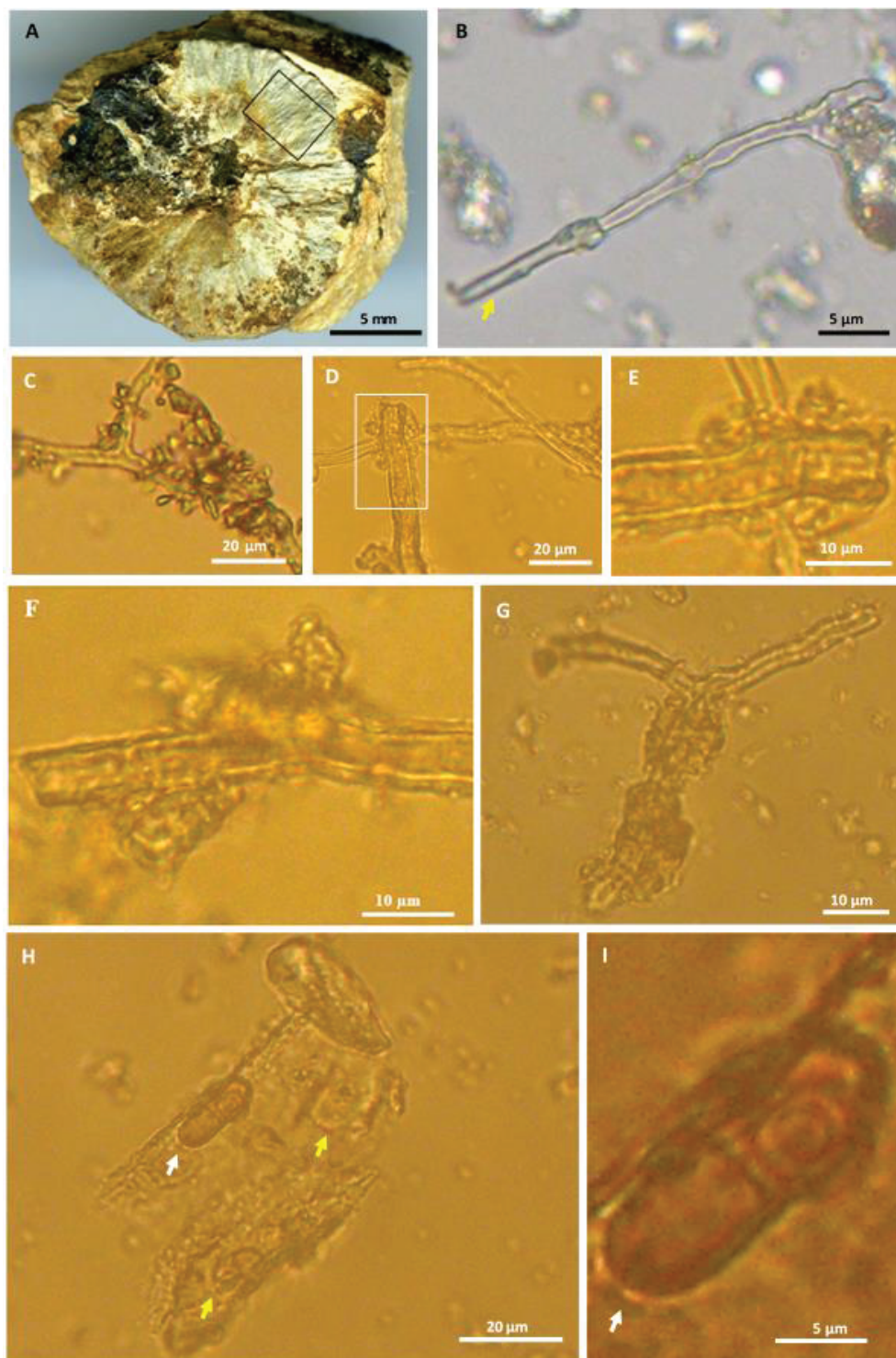


Figure 8: Examples of filaments and silicified cells obtained by scraping in the siliceous mass (chert) of the OKO 26 fibro-radial fabric. (A) Vertical section of OKO 26 and the studied surface. (B) Branched siliceous filament embedded in the chert; note the sheath at one end (yellow arrow, analysed; crossed nicols). (C) Branched siliceous filament adorned with a cluster of ovoids (2-5 µm in size) (not analysed; crossed nicols). (D) Set of hollow filaments showing their tubular shape (diameter 5-8 µm) with a wall measuring 0.5 to 1 µm thick (not analysed; crossed nicols). (E) Detail of an extremity of a hollow filament showing a "double particle" and containing granules of a few µm (not analysed; crossed nicols). (F) Extremity of the same tube with a spherule-like content (not analysed; crossed nicols). (G) Other sheathed hollow filaments (not analysed; crossed nicols). (H) Fragment of large filament (tube) showing very clearly ovoid shapes resembling cells (white and yellow arrows) (not analysed crossed nicols). (I) Detail of a protist-shaped cell (white arrow) (not analysed crossed nicols).

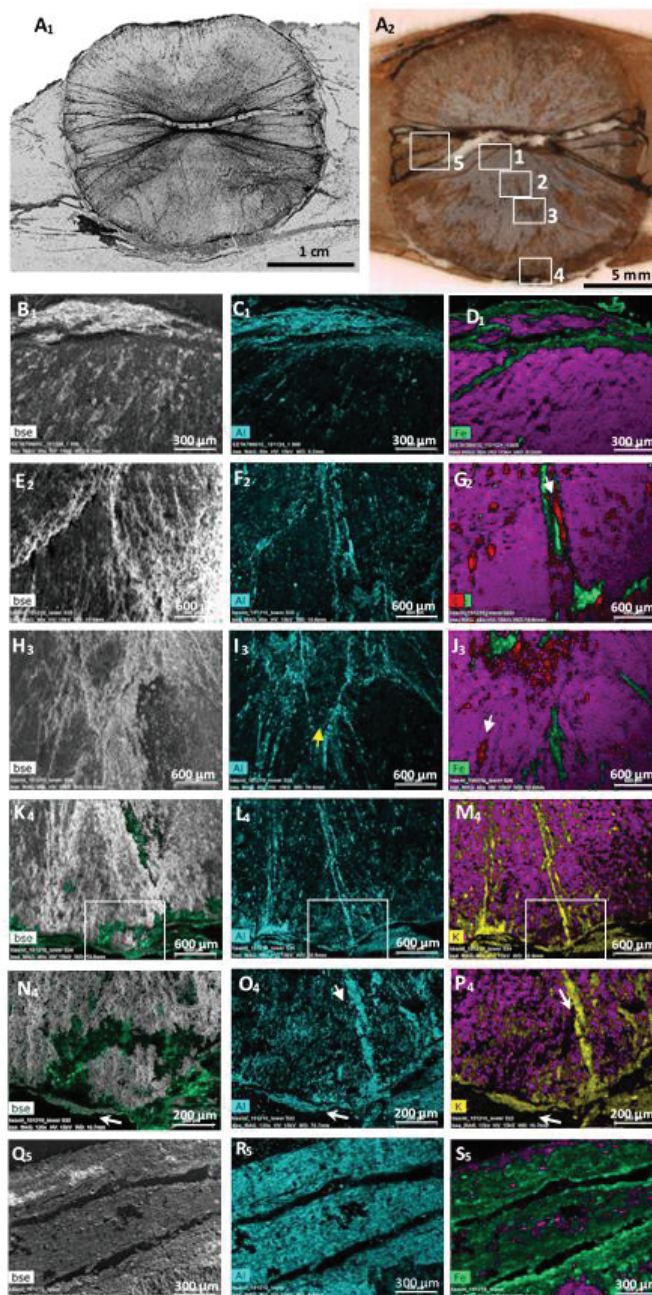


Figure 9: Internal fibro-radial system and chemical elements distribution map in *Akouemma* TS1. (A₁) Thin axial vertical section of an *Akouemma* nodule showing the radial fabric of the tufted zones. Starting from the cones of the hemispheres, this radial fabric is upwardly centrifugal in the upper hemisphere and downwardly centrifugal in the lower hemisphere. (A₂) Thin axial vertical section of another nodule and the analysed zones (1, 2, 3, 4, and 5). (B₁-D₁) Views of the lower hemisphere cone. (B₁) BSE image showing the centrifugal fibro-radial fabric from the top of the cone, which is topped with a highly aluminous mass in (C₁) that is positioned parallel to the border; the white arrow indicates the radial direction. (D₁) Distribution of silica and iron showing the relatively homogeneous distribution of silica and the peripheral position of the iron surrounding the uppermost mass, which is rich in aluminum. Iron is also present in the form of edging with a continuous radial position; this border does not appear to be a fissure but a boundary between the two domains of the cone. (E₂-G₂) View of an internal fibro-radial branching zone (individualization of a 'tuft'). The fibro-radial fabric is highlighted by the distribution of aluminum (clays), which indicates two intersecting directions. The image showing the superposition of silica, iron and carbon demonstrates the homogeneous distribution of silica, the radial arrangement of carbon particles and filaments (white arrow) in the branched area. Iron is in the form of particles and rods that are parallel to carbon in the branched area. (H₃-J₃) View of the end of a 'tuft' (yellow arrow) associated with several branches in a fan shape, with the entire structure highlighted by aluminum; carbon, again arranged in the radial direction, is concentrated in the central part of the tuft. Note the two carbon-rich patterns (white arrow). (K₄-M₄) View of the wavy border of the lower hemisphere, ending in a fan; the radial system is highlighted by aluminum and potassium. Note that the edging is composed of iron, aluminum and potassium, suggesting an envelope along the wavy edges of the nodule. Silica shows a fairly uniform distribution; iron is distributed either in fissures or particles according to the radial system or as a border at the wavy edges of the nodule. See the white boxes for details. (N₄-P₄) Details of the white boxes on the edge of (K₄-M₄). (N₄) Overlay of the BSE image and iron showing the fissures (dark areas) and the form of a border around the nodules (white arrow). (O₄) Distribution of aluminum, highlighting the radial and peripheral systems; note the aligned lenticular forms (more than 200 μm in length) within and around the nodule (white arrows). (P₄) Superimposed images of silicon and potassium that clearly show lenticular forms (white arrows). (Q₅-S₅) View of the median zone showing rectilinear rods; iron is more concentrated at the borders of the rods.

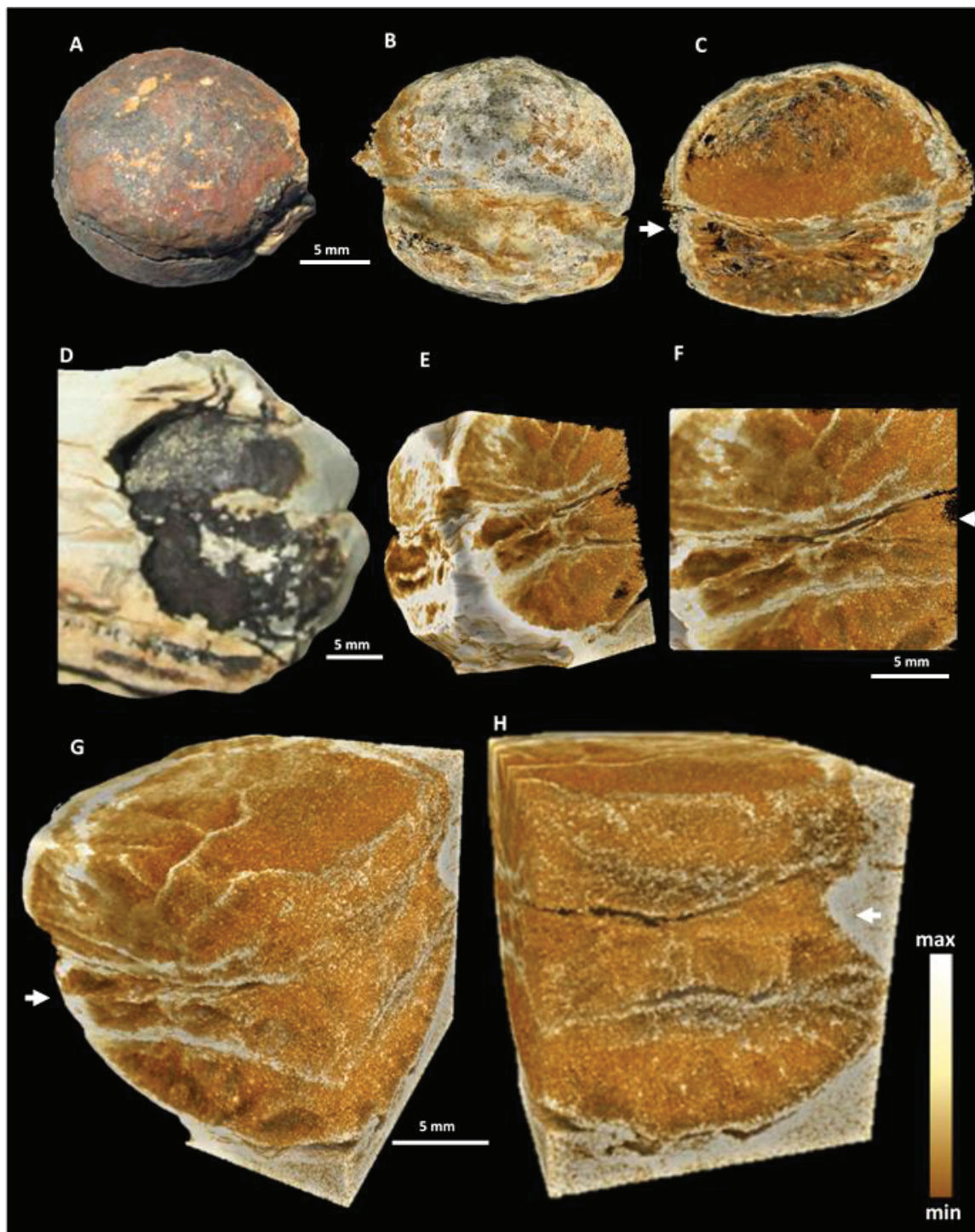


Figure 10: Neutron micro-tomography of *Akouemma* specimens. Neutron attenuation is globally more sensitive to light atoms (see Materials and Methods for details). Three-dimensional images of two reconstructed *Akouemma* specimens, FRA0213 (A, B, and C) and FRA0321 (D-H), obtained with 13.5- μm voxels. The data were filtered and thresholded to facilitate visualization of the internal structures, which are characterized by lower density and by the presence of iron particles and filaments that are generally arranged centrifugally downwards in the lower hemisphere, upwards in the upper hemisphere and laterally in the median disc (white arrow). Note the clearer internal partitions and the edges of the specimens, which are most likely composed of higher concentrations of iron oxide and/or manganese, as well as cracks (in transparency) at the median disc. The colour scale represents the neutron attenuation coefficients.

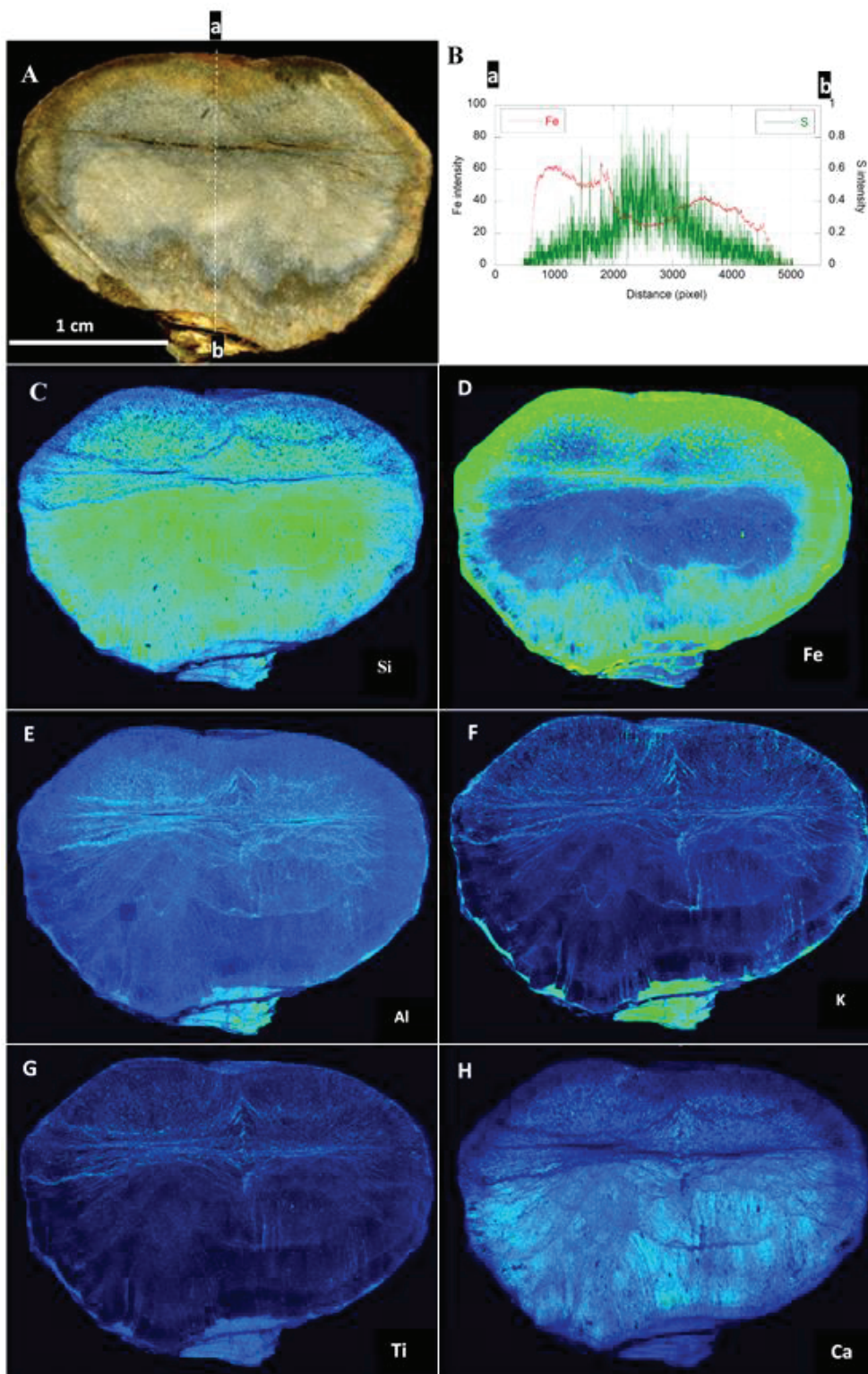


Figure 11: (A) Vertical section of elongated Akou nodule (AKOU 16). (B) Transect (a-b) showing the distributions of Fe and S. Sulphur is more concentrated in the 'core' of the specimen as pyrite. (C-H) Micro-PIXE images of a vertical section of AKOU 16 showing the distributions of silicon, iron, aluminum, potassium, titanium and calcium. The polygonal structure is clearly highlighted by Al, K and Ti of the clay minerals and by Ca.

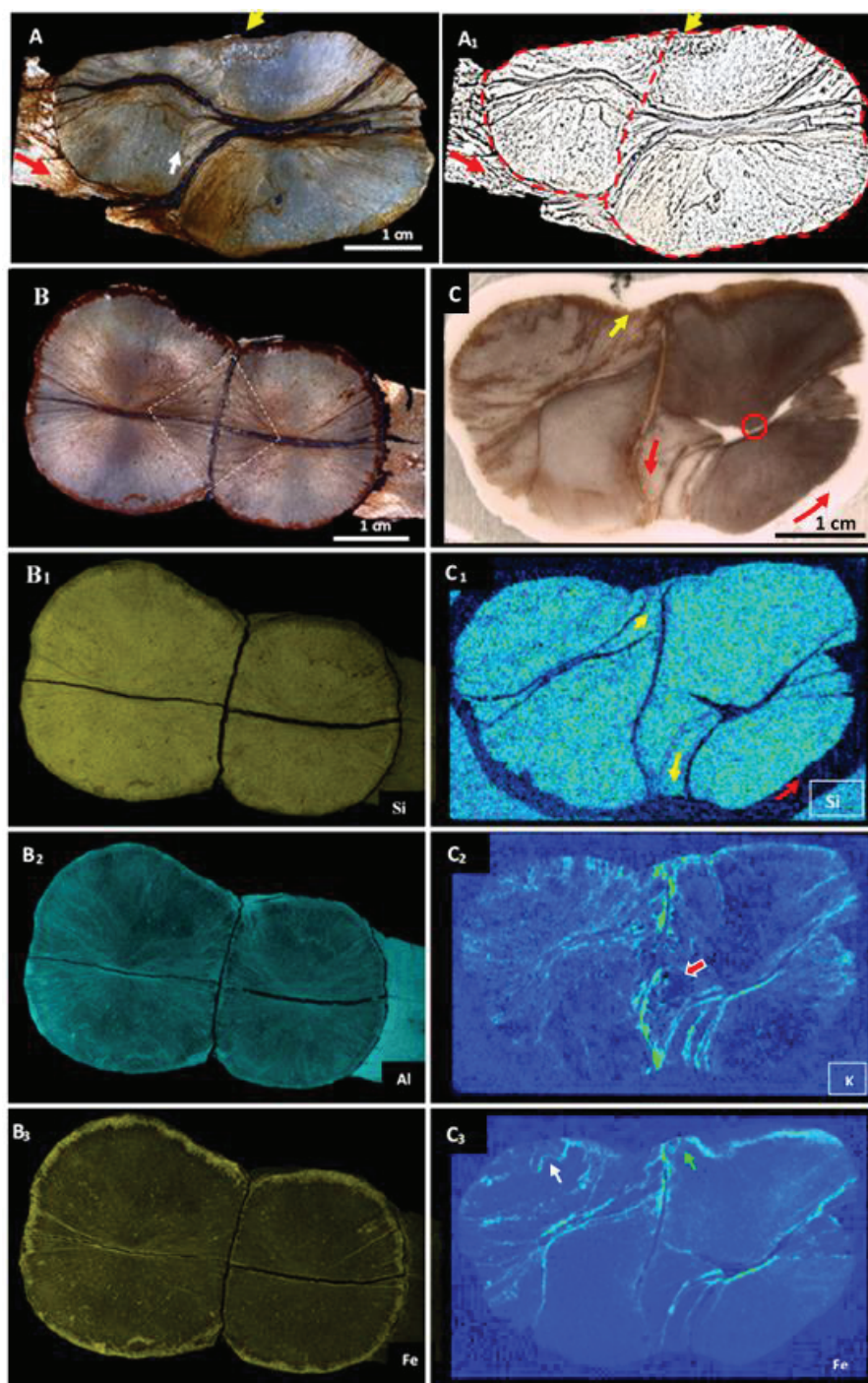


Figure 12: Examples of flattened elongated AKOU 35 nodule and two nodules joined together. (A-A₁) Vertical section of flattened elongated AKOU 35 nodule showing in (A) a flattening of the upper hemisphere (yellow arrow) and a folding of sediments below (red arrow); note the internal polygonal structure (white arrow) (A₁) the scan of same sample shows a distorted internal structure of the upper hemisphere, including the internal polygonal structure (arrow yellow); note the 'duplication' of nodule (red dotted line). (B-B₃) Two non-deformed nodules (double nodule) in vertical section (B); with distribution maps of the elements Si, Al, Fe (B₁-B₃); note the median surface continuous on both nodules, also iron ring is continuous on the periphery of the nodules, and the internal fibro-radial fabrics of the two nodules form a polygonal structure (Box in dotted line) on either side of the suture, that is highlighted by Al. (C-C₃) Two contiguous and deformed nodules, in vertical section (C); with distribution maps of the Si, K, Fe elements (C₁-C₃), which show an intense deformation of the hemispheres, with displacement of the median discs (yellow arrows), hemisphere rotation (red arrow) around a communication point probable (red circle), micro-folds (white arrow) and raised edge (green arrow); note encrusted oblong shape (red-white arrow). Clay minerals (represented by Al and K) clearly show the internal structures of undeformed nodules and deformed nodules. As the "triple nodule" (Figures 3G-3G₂ and Figure S23), the non-deformed "double nodule" suggest a progressive evolution from the elongated forms into single piece (of Figures 3A-3D and 11 and AKOU 35 for example), via the intermediate step (Figure 3E-3E₂), while the adjoining deformed nodules suggest a "confrontation" between two completely independent bodies.

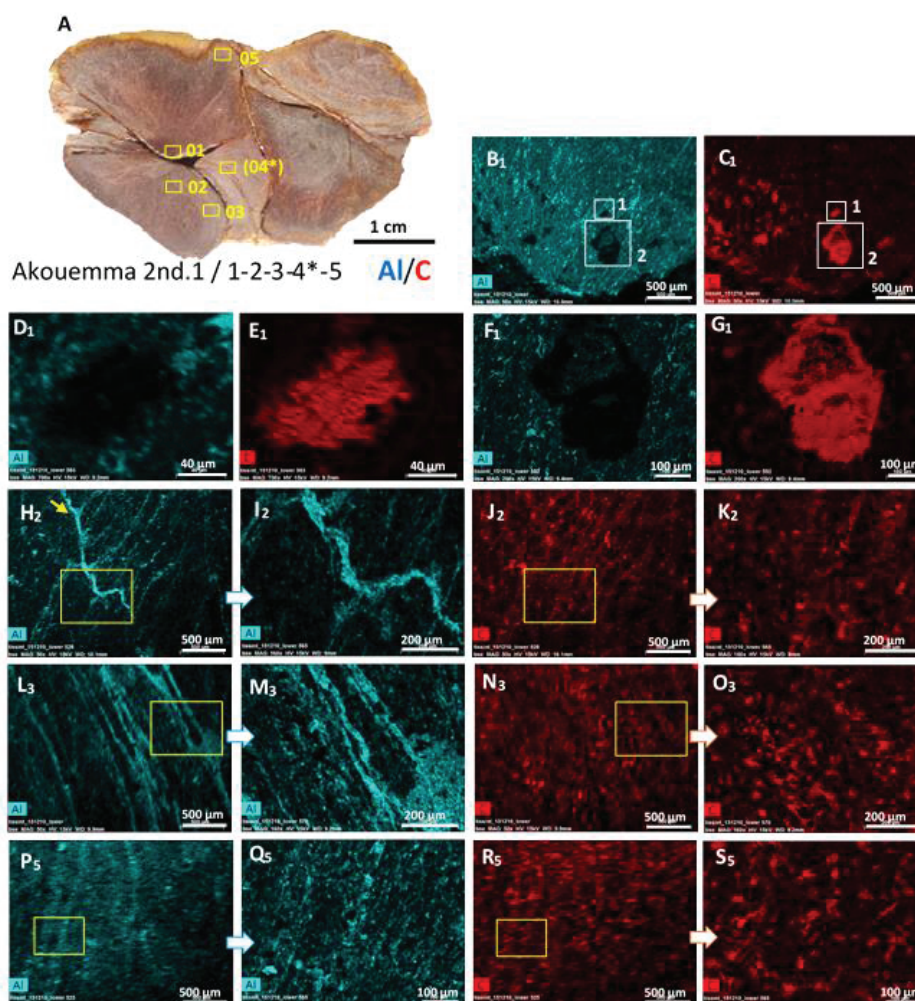


Figure 13: Internal structures of contiguous and deformed *Akouemma 2nd*, nodules in a polished section, showing the distribution maps of aluminum and carbon. The internal structures of the nodules are clearly shown by aluminum and potassium neoformation clays and, more globally, by organic carbon. (A) *Akouemma 2nd*, and the five zones analysed (1-5); for zone 4, see Figure S17. (B₁-G₁) Undeformed cone, zone 1. (B₁) Distribution map of aluminum, showing a simple radial and centrifugal system originating from the cone; note the dark spots scattered throughout the cone. (C₁) Distribution map of carbon, showing its presence in spots corresponding to the dark spots present in (B₁); two zones (1 and 2) were chosen for magnification. (D₁) Magnification of the aluminum image in box 1 of B₁. (E₁) Magnification of the carbon image in box 1 of C₁; note the arrangement of the patterns in the image. For further details, see Figure S14. (F₁) Magnification of the aluminum image in box 2 of B₁. (G₁) Magnification of the carbon image in box 2 of C₁. The carbon is more massive and shows finer patterns, and the aluminum and carbon distributions do not overlap. For further details, see Figure S14bis. (H₂-K₂) Undeformed zone 2 highlighting the fibres and the limits of a tuft or ramp; the parallel fibres are visible and superimposable for the two elements, whereas the limit of the ramp is only made visible by aluminum. (I₂) is the magnified image of (H₂); (K₂) is the magnified image of (J₂). For further details, see Figure S15. (L₃-O₃) Arrowed zone 3 highlighting the filaments and curved tubules. Although the filaments and carbon particles follow the trend, aluminum clearly highlights these structures. (M₃) is the magnified image of (L₃); (O₃) is the magnified image of (N₃). For further details, see Figure S16. (P₅-R₅) Compressed zone 5 with straight filaments presenting lateral micro-shears that are clearly visible in (P₅); carbon particles present lateral stretching in (O₅). For further details, see Figure S18.

the amount of carbon present (Figure S14, S14_{bis}). Its distribution does not reveal the internal structure of the *Akouemma* specimens as well as the carbon (Figures S15H, S16H, S18G, S19J, S19K, S20J, S21J and S22J) or PIXE Ca images (Figure 11G), which sufficiently emphasize bundles in the internal structure that are probably cyanobacterial in origin and have been transformed into a calcite EPS [8].

Aluminum, potassium and magnesium

Aluminum and potassium (7 and 0.3% on average, respectively) and incidentally titanium [8] (Figure 11H), together with silica, are

the principle elements found in clay minerals and are also the elements that most clearly highlight the internal structure of the nodules. These elements outline the external and internal structures of nodules, including fibres, tubules, oblong shape bodies, tuft boundaries, lenticular bodies forming repeated patterns that are aligned inside and around nodules (Figures 9C₁, 9F₂, 9I₃, 9L₄, 9M₄, 9P₄, 9O₄, 9R₅, 12B₂, 13B₁, 13H₂, 13I₂, 13L₃, 13M₃, 13P₅, 13Q₅, 14C₆, 14F₇, 14G₇, 14J₈, 14K₈, 14N₉ and 14O₉ and Figures S5B₂-S5B₃, S13C-S13D, S13G-S13H, S15F-S15G, S16F-S16G, S17F-S17G, S18E, S19 F-S19G, S20 F-S20G,

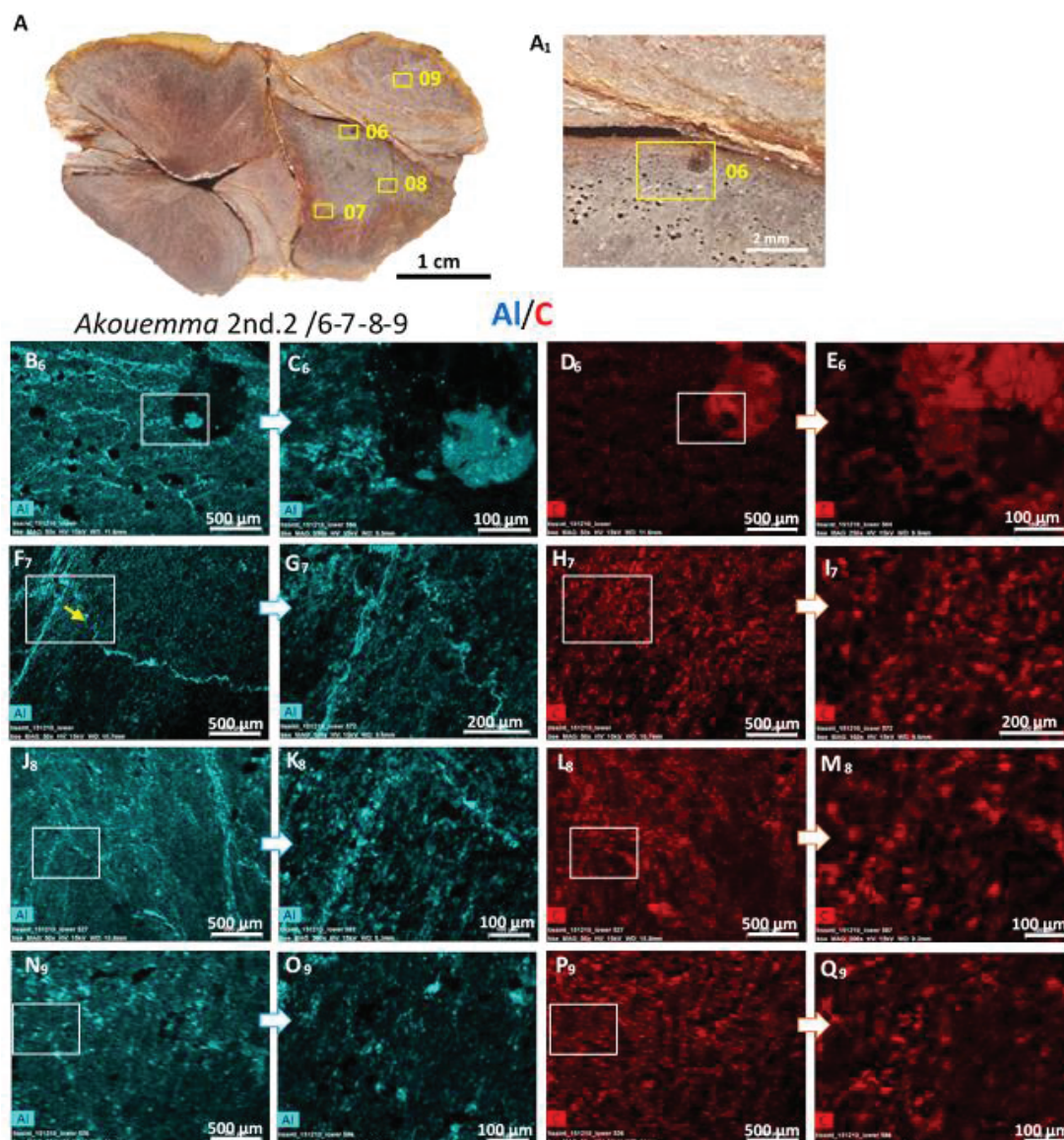


Figure 14: Internal structures of deformed and contiguous *Akouemma 2nd₂* nodules. (A) *Akouemma 2nd₂* nodules showing the four areas analysed (6-9). (B₆-E₆) The lower hemisphere cone, showing no clear radial system but instead an indistinct structure and an oblong mass of organic carbon. (C₆) is the magnified image of (B₆); (E₆) is the magnified image of (D₆). For further details, see Figure S19. (F₇ - I₇) Zone presenting two superimposed ramps and a rectilinear structure with repeating patterns highlighted by aluminum. Note the boundary between the two ramps (yellow arrow); the carbon particles that are oriented in the same direction are mostly homogenous. (G₇) is the magnification of (F₇); (I₇) is the magnified image of (H₇). For further details, see Figure S20. (J₈-M₈) Zone with corrugated structures suggesting micro-folds (but comparison of images K₈ and G₇ suggests deterioration of the structure in K₈). The structures are highlighted by aluminum and superimposed on those highlighted by carbon. (K₈) is the magnified image of (J₈); (M₈) is the magnified image of (L₈). For further details, see Figure S21. (N₉-Q₉) Zone with a disrupted structure that is more or less oriented. The Al distribution maps are superimposed on those of C; the size of the carbon particles is approximately 30 microns. (O₉) is the magnified image of (N₉); (Q₉) is the magnified image of (P₉). For further details, see Figure S22.

S20L-M, S21F-S21G and S22 F-S22G). They also are distributed according to the deformations experienced by the nodules (Figure 12C₂, 13L₃, 13M₃, 13P₅, 13Q₅, 14J₈ and 14K₈, and Figures S5B₁). Maps of the distribution of aluminum and potassium overlap fairly well with those of the distribution of carbon, and lesser in the areas with carbon masses >80 μm in size (Figures 13B₁, 13D₁, 13F₁, 14B₆). In most cases, aluminum and potassium overlay the particles and carbon filaments by highlighting their alignment (Figures 13H₂, 13L₃, 13M₃, 13P₅, 13Q₅, 14F₇, 14G₇), their dispersion and distortion (Figures 14J₈, 14K₈, 14N₉ and 14O₉, and S17 F, S17G, S18E, S20C, S21 F, S21G, S22F and S22G).

Magnesium is found in trace amounts in the nodules; it is associated with aluminum and potassium, and outlines the internal structures of the nodules poorly (Figures S15I, S16I, S19H, S19I, S20I and S22I). Although infiltrating clays are often observed in the gangue in these specimens, the clay minerals in the *Akouemma* specimens are essentially authigenic clays that reveal their internal structure; these are lepidocrocite, vermiculite-kaolinite and chlorite (Figure S10) [8].

Iron

Iron, associated with cobalt or manganese, is present as both oxides and sulphides, and its distribution and concentration vary both

within individual nodules and around nodules. Iron distribution in the nodules is radial and centrifugal in the form of particles and filaments (Figures 9 G₂, 9J₃, 10C, 10E-10H, 11D, 12B, 12B₃ and Figures S4B, S4C and S5A-S5A₃); sometimes a few particles intersect the radial direction (Figure S21M) or are dispersed within the siliceous mass (Figure S19L and S19M). Iron sometimes emphasizes micro-folds in the nodule (Figure 12C₃). The sulphide form is found more in the “core” of the nodule (Figure 11B). Iron often forms a ring at the inner border and an external rim around the nodule (Figures 10A-10C, 10D-10E, 11D, 12B, 12B₃) that is composed of a succession of lenticular bodies (Figures S5A-S5A₃, S6A, S6A4-S6A5). Iron is also concentrated in the cracks and in the interfaces between the internal structures of a specimen (Figures 9A₁, 9D₁, 9K₄, 9N₄, 9S₅ and 12C₃ and Figures S5A, S6A and S21H). Iron sulphide generally appears in the form of small crystals with a bristled surface. In its oxidized form, small cubic iron crystals exhibits fossilized clumps of 2-5 µm black carbon particles (Figure S7A, F-H in File S1) and red ferro-silico-aluminous spherules (Figure S7J-S7J₂).

Silicon and radioactivity

Silicon is the most abundant element in the nodules (80%) [8]. It is homogeneously distributed in the nodules in the form of micro-quartz (chert). In *Akouemma* nodules, aluminum and potassium record in the detail the internal and external structures, whereas silica preserves in the whole their initial morphological (deformed and undeformed) states (Figure 11C, 12B₁ and 12C₁ and Figure S4G). The rapid crystallization of silicon allowed instantaneous preservation of various internal and external states of *Akouemma* nodules, thereby preserving the organic carbon, microorganisms and other biomorphs as well as the original structures and authigenic minerals. Locally, a few “bricks” with siliceous walls, observed in nodules, contain red Fe-Al-Si-rich spherules and black carbon-rich particles (Figure S8F-S8H, S9F-S9N).

An autoradiography was performed on the AKOU 14, AKOU 15, AKOU 16 nodules and on their gangue. The distribution of the radioactivity revealed a clear discontinuity between the non-radioactive nodules in the healthy part and the radioactive sediment. The altered edges of the nodules are contaminated with radioactivity (Figure S8A₁, S8A₂).

Discussion

Silica-carbonate nodules discovered in the FB₂ formations of the Akou River were interpreted as biogenic nodules according to the following criteria:

1. Nodules with 2 hemispheres, 1 median disc, complex internal radial fabric, vertical and lateral symmetry, chains of joined nodules, indicating a complex organization;
2. Flexible deformations by lateral compression, indicating a ductile/plastic body;
3. Fibro-radial and polyphase internal complex fabric, suggesting growth;
4. Deformed sediments around and between specimens in tabular beds, suggesting growth in soft sediments;
5. ¹³C-depleted carbonaceous matter and ¹³C-depleted calcite, indicating precipitation of calcite by microbial metabolism and degradation of organic matter under anoxic photosynthesis conditions;

Radiating remnants of biofilms and calcite grains, suggesting an EPS calcite altered and replaced by silicification.

The ductile/plastic nodules with complex internal radial fabric containing linear and flattened clayey “channels”, cyanobacteria, many biomorphs (spherulites, filaments, vesicles) and multicellular clusters led to the conclusion that the Akou nodules are biogenic nodules hosting multicellular consortia; they are therefore designated *Akouemma* nodules.

The new criteria highlighted are:

1. Deformation and lateral spreading of matter;
2. An internal fibro-radial fabric consisting initially of carbon particles;
3. Decaying and dispersion of particles cell-like and broken tubules in the undeformed siliceous mass;
4. Close association between carbon and K-Al-(Ti)-rich clay minerals;
5. Likely vegetative reproduction by duplication.

The formation of silico-carbonate “abiotic” nodules by interactions between sediments and microorganisms lead to the formation of the accretion laminae observed in these nodules and in the stromatolites, from the Proterozoic [22-24] to modern analogues [25]; and microbially mediated calcification can be traced back for at least the Proterozoic [26-30]. Additionally, these “abiotic” concretions typically develop from a central point and present often a zonal concentric structure; they may contain concentric and lateral accretion laminae [31], characterized by variations in the isotopic and geochemical compositions of the different growth zones [32]. Other carbonate concretions are growing from inert clumps of organic matter, typically in fine sediments, probably as a result of the diffusion of carbon dioxide during the decomposition of organic matter through microbial processes [33-35]. These diagenetic nodules vary in shape and size within the same basin; they can be spherical, elongated, flattened and laterally extended; and can vary from a few millimetres to a few metres in size [36,37].

The preservation of organic micro- and macrofossils by clay minerals, which has received increased interest in recent years [38-44], has been widely reported from the Palaeozoic and terminal Neoproterozoic (Ediacaran) rock record [45-50]. Support for the role of authigenic clay precipitation in organism preservation comes both from experiments [51-54] and from field studies of modern environments [21,55-57]. These show that microbial mediation of clay minerals is common for the preservation of microorganisms and soft-body macroorganisms. Varieties of Fe-, Mg- and K-rich alumina-silicates have been found in close association with both well-preserved macrofossils [40,43,44,47,49] and, more rarely, microfossils [21,48,57].

Akouemma nodules contain EPS calcite as “abiotic” carbonate concretions that are characteristic of microbial activity. They differ in terms of their homogeneous form and size; they typically consist of two hemispheres with their central nipple-like feature of the upper hemisphere and corresponding central depression of the lower hemisphere. The central nipple-like feature and the corresponding central depression likely correspond to a “communication point” between the two hemispheres which are separated by the median disc with its central orifice. They differ by their centrifugal internal fabric radiates from the cones of each hemisphere in spheroidal nodules and a polyphase internal fabric with an internal polygonal structure in elongated forms. The presence of this radial internal fabric, highlighted by Al-K-(Ti)-rich clay minerals in close association with carbon particles and by Ca calcite and Fe oxides-sulphides shows that

the clay minerals (and the other minerals) precipitated during early (pre-compaction) diagenesis, preventing compaction of nodules and enclosed microfossils. The absence of radioactivity in the unaltered silicified nodules, while sediments and altered edges of the nodules are radioactive probably confirms their very early silicification, would indicate a different origin between nodules and sediments. They differ also of their mutual flexible deformation which strongly affects nodules, including radial internal fabric. The deformations by mutual lateral compression of the grouped nodules, with spreading of matter (probably due to their growth), adjoined to other non-deformed nodules or by vertical compression affecting only the upper hemispheres of nodules, causing deformations of the surrounding sediment (compaction between two nodules or micro-folding under the nodules) in the bedding planes, indicate syn-sedimentary deformations of these nodules. These latter therefore would not have any direct link with the sediment, corroborating the arrangement of the repeated patterns around nodules and in the sediment. Similarly the nodules have various marks (depressions, grooves), repeated Fe-Al-K-rich patterns in and around nodules, lenticular and oblong bodies that sometimes cause deformations on the nodules. Silica (micro-quartz) is uniformly distributed in all specimens (distorted or not) and does not present any deformation; therefore, we infer that silicification is an early process that fixes initial states, including deformations, degradations and internal degrees of dispersion and spreading of particles and fragments in the nodules. Furthermore, Neoproterozoic and Phanerozoic fossilizations are known to contain microorganisms and soft-bodied macroorganisms preserved by Fe-Mg-K-rich clay minerals [39,40,44-47]. In the *Akouemma* nodules, we highlight for the first time in the history of the earth sciences a close association of organic matter with Al-K-(Ti)-rich clay minerals in the presence of EPS-type calcite and pyrite in material from the Palaeoproterozoic at 2.2 Ga. The different associations of iron oxides with carbon particles in "bricks" with siliceous walls, and in "cubic crystals" containing carbon particles with a few grades of Si and Al, and undergoing epigenization by iron suggest that the red Fe- Al- Si-rich spherules which are very abundant in the nodules [8] arose from mineralization of the carbon particles.

Finally, the elongated *Akouemma* nodules show signs of division marked by the presence of external furrows that become increasingly deep with the progression from elongated shapes in single pieces to segmented elongated forms, with individualization of new spheroidal bodies. This process likely corresponds to a division phase, recalling the vegetative reproduction of unicellular micro-organisms [58,59] or primitive macro-organisms [60] including the enigmatic macrofossils of late Ediacaran [61].

Together with the criteria previously defined [8], the new biogenic criteria, which emphasize an initial fibro-radial internal fabric with carbon preserved by clay minerals, branched filaments and cells preserved in the siliceous mass, plastic deformation via mutual lateral compression, and "self-strangulation" similar to a cell division, support the integration of *Akouemma* specimens in the register of primitive organic macrofossils found in the Proterozoic.

Although these specimens exhibit different sizes, shapes, structures and habitats, they are added to those discovered in the Palaeo- and early Mesoproterozoic, including a eukaryotic *Grypania spiralis* found in banded iron formations in Michigan and in the Rohtas Formation (India) and dated approximately 1.6 Ga [62,64], colonies of *Horodyskia* fossils discovered in sedimentary rocks in China, North America, and Australia and dated to 1.5 Ga [65-68], and a colony of *Discagma buttonii*

fossils discovered in the palaeosols of South African and dated to 2.2 Ga [69]. This discovery of *Akouemma* specimen colony in the FB2b formations of the Okondja Basin brings a new vision to the discovery of large colonial multicellular organisms in the FB2b formations of the Franceville Basin [5,7]. Otherwise, current investigations show macrofossil-like material, including pyritous vermiforms, distributed from FB1 to FD in the Francevillian Group (Figure 1) and would entirely change our understanding of life evolution on Earth.

Background

Since 1966, several studies have reported the presence of macrofossils [2], communities of microfossils and stromatolite [3,4,6] and abundant organic matter [12,70] in Francevillian sedimentary formations in Gabon. Unfortunately, these findings had little impact on the scientific world until the publication of an article on large colonial organisms [5] renewed interest in research on the origin of life in the Francevillian basin.

A team from the Research Unit in Geosciences and Environment (URESTE) of Masuku University had in recent years already accumulated observations of and collected various specimens, including vermiform pyritized in FB1, to more than 2.1 Ga. These include *Akouemma* nodules in FB, oval shapes along the transverse plane in FB-FC, and flattened shapes containing phosphorus and calcium in FD (Figure 1) dated at 2083± 6 Ma [71,72]. There was indeed a type of biological 'proliferation' at approximately this period that corresponds to a Great Oxidation Event (GOE), a period of increased oxygenation due in particular to cyanobacterial activity [73,74]. The first published results of the URESTE team following funding from the Ministry of National Education in December 2010 and from the Faculty of Sciences of Masuku University in 2014 described the Okondja nodules as biogenic nodules [8]. Further investigations of the same nodules, mainly financed by the Inter-University Cooperation (Tokyo Institute of Technology, Japan; CENBG, University of Bordeaux, France; Paul Scherrer Institute, Villigen PSI Switzerland and Geosciences Environment of Toulouse, GET, France) led to the elaboration of this paper. These remarkable results bring a new view of life as reflected by the characteristics of organisms that lived at least 2.2 Ga.

In the context of a Memorandum of Understanding between the Tokyo Institute of Technology and the "Université des Sciences et Techniques de Makusu" and with the support of partnerships with the Universities of Toulouse and Bordeaux and with the Paul Scherrer Institute; other investigations of pyritous fossils of FB₁ and other specimens of FB, FC and FD (Figure 1) are under way. The Francevillian Group could be the oldest Konservat-Lagerstätten (a sedimentary deposit with exceptional fossil preservation), in which both micro- and macrofossils are preserved in silica, pyrite, clay minerals or phosphate. We remain open to all win-win collaborations.

Conclusion

Akouemma hemisphaeria, a colony of organic macrofossils

Although we cannot determine the precise modern analogues of the *Akouemma* specimens, we conclude that the *Akouemma* nodules formed an organic sessile macrofossil colony with a soft-plastic body, an internal carbon fibro-radial fabric and a likely vegetative reproduction by duplication. They hosted cyanobacteria, filamentous microfossils, green algae tubules, and other uni- and multicellular organisms on the seafloor of the Okondja basin at 2.2 Ga. These specimens are designated *Akouemma hemisphaeria*⁽¹⁾.

(1) *Akouemma hemisphaeria*: Fossile at two hemispheres of Akou River highlighted for the first time by Edou-Minko and Moussavou Mathieu.

Acknowledgements

We thank Harumasa Kano (Tohoku University Museum) for performing the micro-CT analysis and Tsuyoshi Komiya (The University of Tokyo) and Gérard Delorme (Comilog geologist, retired) for their helpful comments. This research was partly supported by a grant for "Hadean Bioscience (No. 26106002)" from the Japan Society for the Promotion of Science (JSPS).

References

- Ossa FO, El Albani A, Hofmann A, Bekker A, Gauthier-Lafaye F, et al. (2013) Exceptional preservation of expandable clay minerals in the ca. 2.1 Ga black shales of the Francevillian basin, Gabon and its implication for atmospheric oxygen accumulation. *Chem Geol* 362: 181-192.
- Feys R, Greber C, Pascal M (1966) A propos de l'ancienneté de la flore continentale: découverte de "charbons" et de "phytomorphes" dans le Francevillien (Précambrien du Gabon). *Bull Soc Géol France* 7: 638-641.
- Amard B, Bertrand-Sarfati J (1997) Microfossils in 2000 Ma old cherty stromatolites of the Franceville Group, Gabon. *Precambrian Res* 81: 197-221.
- Dutkiewicz A, George SC, Mossman DJ, Ridley J, Volk H (2007) Oil and its biomarkers associated with the Palaeoproterozoic Oklo natural fission reactors, Gabon. *Chem Geol* 244: 130-154.
- E Albani A, Bengtson S, Canfield DE, Bekker A, Macchiarelli R, et al. (2010) Large colonial organisms with coordinated growth in oxygenated environments 2.1 Gyr ago. *Nature* 466: 100-103.
- Préat A, Bouton P, Thiéblemont D, Prian JP, Ndounze SS, et al. (2011) Paleoproterozoic high $\delta^{13}\text{C}$ Dolomites from the Lastoursville and Franceville basins (SE Gabon): stratigraphic and syndepositional subsidence implications. *Precambrian Res* 189: 212-228.
- E Albani A, Bengtson S, Canfield DE, Riboulleau A, Bard CR, et al. (2014) The 2.1 Ga Old Francevillian biota: Biogenicity, taphonomy and biodiversity. *PLoS One*. 9: e99438.
- Moussavou M, Edou-Minko A, Mounquegui M, Ortega R, Fleury G, et al. (2015) Multicellular consortia preserved in biogenic ductile-plastic nodules of Okondja Basin (Gabon) by 2.1 Ga. *J Geol Geosci* 4: 1-13.
- Sawaki Y, Moussavou M, Sato T, Suzuki K, Ligna C, et al. (2016) Chronological constraints on the Paleoproterozoic Francevillian Group in Gabon. *Geoscience Frontiers*.
- Moussavou M, Edou-Minko A (2006) Contribution the thermo-tectonic history of the Precambrian N'goutou ring complex by geochemistry and geochronology U/Pb accessory minerals (Francevillien Okondja Basin, Gabon). *Africa Geosci Rev* 13: 53-61.
- Gauthier-Lafaye F, Weber F (2003) Natural nuclear fission reactors: time constraints for occurrence, and their relation to uranium and manganese deposits and to the evolution of the atmosphere. *Precambrian Res* 120: 81-100.
- Mossman D, Gauthier-Lafaye F, Jackson S (2005) Black shales, organic matter, ore genesis and hydrocarbon generation in the Paleoproterozoic Franceville series, Gabon. *Precambrian Res* 137: 253-272.
- Kump LR, Junium C, Arthur MA, Brasier A, Fallick A, et al. (2011) Isotopic evidence for massive oxidation of organic matter following the Great Oxidation Event. *Science* 334: 1694-1696.
- Weber F, Gauthier-Lafaye F (2013) No proof from carbon isotopes in the Francevillian (Gabon) and Onega (Fennoscandian shield) basins of a global oxidation event at 1980-2090 Ma following the Great Oxidation Event (GOE). *Comptes Rendus Geosci* 345: 28-35.
- Wacey D (2009) *Early life on Earth. A practical Guide*. New York: Springer Verlag.
- Ortega R, Maire R, Devès G, Quinif Y (2005) High-resolution mapping of uranium and other trace elements in recrystallized aragonite-calcite speleothems from caves in the Pyrenees (France): implication for U-series dating. *Earth Planet Science Lett* 237: 911-923.
- Anderson IS, McGreevy RL, Bilheux HZ (2009) *Neutron imaging and applications*. New York: Springer Verlag.
- Kaestner A, Vontobel P, Lehmann E (2010) Neutron imaging methods in geoscience. *Adv Comput Tomogr Geomater* p352-365.
- Kaestner AP, Hartmann S, Kühne G, Frei G, Grünzweig C, et al. (2011) The ICON beamline-A facility for cold neutron imaging at SINQ. *Nuclear Instrum Methods Phys Res Sect A Accel Spectrom Detectors Assoc Equip* 659: 387-393.
- Frei G, Lehmann EH, Mannes D, Boillat P (2009) The neutron micro-tomography setup at PSI and its use for research purposes and engineering applications. *Nuclear Instrum Methods Phys Res Sect A Accel Spectrom Detectors Assoc Equip* 605: 111-114.
- Kaźmierczak J, Kremer B, Altermann W, Franchi, I (2016) Tubular microfossils from- 2.8 to 2.7 Ga-old lacustrine deposits of South Africa: A sign for early origin of eukaryotes? *Precambrian Res* 286: 180-194.
- Cloud PE, Semikhatov MA (1969) Proterozoic stromatolite zonation. *Am J Sci* 267: 1017-1061.
- Hofmann HJ, Jackson GD (1987) Proterozoic minstromatolites with radial-fibrous fabric. *Sediment* 34: 963-971.
- Kuznetsov AB, Gorokhov IM, Melezhik VA, Mel'nikov NN, Konstantinova GV, et al. (2012) Strontium isotope composition of the lower Proterozoic carbonate concretions: the Zaonega Formation, Southeast Karelia. *Lithology Miner Resour* 47: 319-333.
- Reid RP, Visscher PT, Decho AW, Stolz JF, Bebout BM, et al. (2000) The role of microbes in accretion, lamination and early lithification of modern marine stromatolites. *Nature* 406: 989-992.
- Klein C, Beukes NJ, Schopf JW (1987) Filamentous microfossils in the early Proterozoic Transvaal Supergroup: their morphology, significance, and palaeoenvironmental setting. *Precambrian Res* 36: 81-94.
- Knoll AH, Fairchild LJ, Swett K (1993) Calcified microbes in Neoproterozoic carbonates: Implications for our understanding of the Proterozoic/Cambrian transition. *Palaios* 8: 512-525.
- Wright DT, Altermann W (2000) In: Insalco E, Skelton PW, Palmer TJ (eds.) *Microfacies development in Late Archaean stromatolites and oolites of the Campbellrand Subgroup, South Africa. Carbonate Platform Systems. Components and Interactions*. *Geol Soc Lond Spec Publ* 178: 51-70.
- Kaźmierczak J, Altermann W (2002) Neoproterozoic biomineralisation by benthic cyanobacteria. *Science* 298: 2351.
- Altermann W, Kaźmierczak J, Oren A, Wright DT (2006) Cyanobacterial calcification and its rock-building potential during 3.5 billion years of Earth history. *Geobiol* 4: 147-166.
- Gomez FJ, Kah LC, Bartley JK, Astini RA (2014) Microbialites in a high-altitude Andean lake: multiple controls on carbonate precipitation and lamina accretion. *Palaios* 29: 233-249.
- Mozley PS (1996) The internal structure of carbonate concretions in mudrocks: A critical evaluation of the conventional concentric model of concretion growth. *Sediment Geol* 103: 85-91.
- Dupraz C, Reid RP, Braissant O, Decho AW, Norman RS, et al. (2009) Processes of carbonate precipitation in modern microbial mats. *Earth Sci Review* 96: 141-162.
- Aloisi G, Glöter A, Krüger M, Wallmann K, Guyot F, et al. (2006) Nucleation of calcium carbonate on bacterial nanoglobules. *Geol* 34: 1017-1020.
- Spadafora A, Perri E, McKenzie JA, Vasconcelos C (2010) Microbial biomineralization processes forming modern Ca:Mg carbonate stromatolites. *Sediment* 57: 27-40.
- McBride EF, Picard MD, Milliken KL (2003) Calcite-cemented concretions in Cretaceous Sandstone, Wyoming and Utah, USA. *J Sedimentary Res* 73: 462-483.
- Raiswell R, Fisher QJ (2000) Mudrock-hosted carbonate concretions: a review of growth mechanisms and their influence on chemical and isotopic composition. *J Geol Soc* 157: 239-251.
- Gabbott SE, Norry MJ, Aldridge RJ, Theron JN (2001) Preservation of fossils in clay minerals; a unique example from the Upper Ordovician Soom Shale, South Africa. *Proc York Geol Soc* 53: 237-244.

39. Zhu M, Babcock LE, Steiner M (2005) Fossilization modes in the Chengjiang Lagerstätte (Cambrian of China): testing the roles of organic preservation and diagenetic alteration in exceptional preservation. *Palaeogeog Palaeoclim Palaeoecol* 220: 31-46.
40. Zhang X, Briggs DEG (2007) The nature and significance of the appendages of *Opabina* from the Middle Cambrian Burgess Shale. *Lethaia* 40: 161-173.
41. Page A, Gabbott SE, Wilby PR, Zalasiewicz JA (2008) Ubiquitous Burgess Shale-style "clay templates" in low-grade metamorphic mudrocks. *Geol* 36: 855-858.
42. Ushatinskaya GT (2009) Preservation of living organic structures in unicellular and multicellular organisms in the fossil state. *Palaeontol J* 43: 928-939.
43. Meyer M, Schiffbauer JD, Xiao S, Cai Y, Hua H (2012) Taphonomy of the Upper Ediacaran enigmatic ribbonlike fossil *Shaanxilithes*. *Palaios* 27: 354-372.
44. Laflamme M, Schiffbauer JD, Narbonne GM, Briggs DEG (2011) Microbial biofilms and the preservation of the Ediacara biota. *Lethaia* 44: 203-213.
45. Gabbott SE (1998) Taphonomy of the Ordovician Soom Shale lagerstätte: an example of soft tissue preservation in clay minerals. *Palaeontol* 41: 631-667.
46. Petrovich R (2001) Mechanisms of fossilization of the soft-bodied and lightly armored faunas of the Burgess Shale and some other classical localities. *Am J Sci* 301: 683-726.
47. Anderson EP, Schiffbauer JD, Xiao S (2011) Taphonomic study of Ediacaran organic-walled fossils confirms the importance of clay minerals and pyrite in Burgess Shale-type preservation. *Geology* 39: 643-646.
48. Callow RT, Brasier MD (2009) A Solution to Darwin's dilemma of 1859: exceptional preservation in Salter's material from the late Ediacaran Longmyndian Supergroup, England. *J Geol Soc Lon* 166: 1-4.
49. Cai Y, Schiffbauer JD, Hua H, Xiao S (2012) Preservational modes in the Ediacaran Gaojiashan Lagerstätte: Pyritization, aluminosilicification, and carbonaceous compression. *Palaeogeog Palaeoclim Palaeoecol* 326-328: 109-117.
50. Orr PJ, Briggs DDG, Kearns SL (1998) Cambrian Burgess Shale animals replicated in clay minerals. *Science* 281: 1173-1175.
51. Mera MU, Beveridge TJ (1993) Mechanism of silicate binding to the bacterial cell wall in *Bacillus subtilis*. *J Bacteriol* 175: 1936-1945.
52. Urrutia MM, Beveridge TJ (1994) Formation of fine-grained metal and silicate precipitates on a bacterial surface (*Bacillus subtilis*). *Chem Geol* 116: 261-280.
53. Fiore S, Dumontet S, Huertas FJ, Pasquale V (2011) Bacteria-induced crystallization of kaolinite. *Appl Clay Sci* 53: 566-571.
54. McMahon S, Anderson RP, Saupe EE, Briggs DE (2016) Experimental evidence that clay inhibits bacterial decomposers: Implications for preservation of organic fossils. *Geol* 44: 867-870.
55. Konhauser KO, Urrutia MM (1999) Bacterial clay authigenesis: a common biogeochemical process. *Chem Geol* 161: 399-413.
56. Ueshima M, Tazaki K (2001) Possible role of microbial polysaccharides in nontronite formation. *Clays Clay Min* 49: 292-299.
57. Wacey D, Saunders M, Roberts M, Menon S, Green L, et al. (2014) Enhanced cellular preservation by clay minerals in 1 billion-year-old lakes. *Scient Reports* 4.
58. Darby DG (1974) Reproductive modes of *Huroniospora microreticulata* from cherts of the Precambrian Gunflint Iron-Formation. *Geol Soc Am Bull* 85: 1595-1596.
59. Sugitani K, Mimura K, Takeuchi M, Lepot K, Ito S, et al. (2015) Early evolution of large micro-organisms with cytological complexity revealed by microanalyses of 3.4 Ga organic-walled microfossils. *Geobiol* 13: 507-521.
60. Morandini AC, Custódio MR, Marques AC (2016) Phylum porifera and cnidaria. *Mar Freshwat Tox* pp: 1-24.
61. Mitchell EG, Kenchington CG, Liu AG, Matthews JJ, Butterfield NJ (2015) Reconstructing the reproductive mode of an Ediacaran macro-organism. *Nature* 524: 343-346.
62. Han TM, Runnegar B (1992) Megascopic eukaryotic algae from the 2.1-billion-year-old Negaunee iron-formation, Michigan. *Science* 257: 232-235.
63. Sharma M, Shukla Y (2009) The evolution and distribution of life in the Precambrian eon-global perspective and the Indian record. *J Biosci* 34: 765-776.
64. Sarangi S, Gopalan K, Kumar S (2004) Pb-Pb age of earliest megascopic, eukaryotic alga bearing Rohtas Formation, Vindhyan Supergroup, India: implications for Precambrian atmospheric oxygen evolution. *Precambrian Res* 132: 107-121.
65. Dong L, Xiao S, Shen B, Zhou C (2008) Silicified *Horodyskia* and *Palaeopascichnus* from upper Ediacaran cherts in South China: tentative phylogenetic interpretation and implications for evolutionary stasis. *J Geol Soc* 165: 367-378.
66. Grey K, Yochelson EL, Fedonkin MA, Martin DM (2010) *Horodyskia williamsii* new species, a Mesoproterozoic macrofossil from Western Australia. *Precambrian Res* 180: 1-17.
67. Calver CR, Grey K, Laan M (2010) The 'string of beads' fossil (*Horodyskia*) in the mid-Proterozoic of Tasmania. *Precambrian Res* 180: 18-25.
68. Retallack GJ, Dunn KL, Saxby J (2013) Problematic mesoproterozoic fossil *horodyskia* from Glacier National Park, Montana, USA. *Precambrian Res* 226: 125-142.
69. Retallack GJ, Krull ES, Thackray GD, Parkinson D (2013) Problematic urn-shaped fossils from a Paleoproterozoic (2.2 Ga) paleosol in South Africa. *Precambrian Res* 235: 71-87.
70. Cortial F, Gauthier-Lafaye F, Lacrampe-Couloume G, Oberlin A, Weber F (1990) Characterization of organic matter associated with uranium deposits in the Francevillian Formation of Gabon (Lower Proterozoic). *Organic Geochem* 15: 73-85.
71. Horie K, Hidaka H, Gauthier-Lafaye F (2005) U-Pb geochronology and geochemistry of zircon from the Franceville series at Bidoudouma, Gabon. *Geochimica, Cosmochimica Acta* 69: A11.
72. Gauthier-Lafaye F (2006) Time constraint for the occurrence of uranium deposits and natural nuclear fission reactors in the Paleoproterozoic Franceville Basin (Gabon). *Geol Soc Am Memoirs* 198: 157-167.
73. Hamilton TL, Bryant DA, Macalady JL (2016) The role of biology in planetary evolution: cyanobacterial primary production in low-oxygen Proterozoic oceans. *Environ Microbiol* 18: 325-340.
74. Schirrmeister BE, Sanchez-Baracaldo P, Wacey D (2016) Cyanobacterial evolution during the Precambrian. *Int J Astrobiol* 1: 1-18.

Supplementary File

Figures S1 through S23 provide additional details related to the main text illustrations.

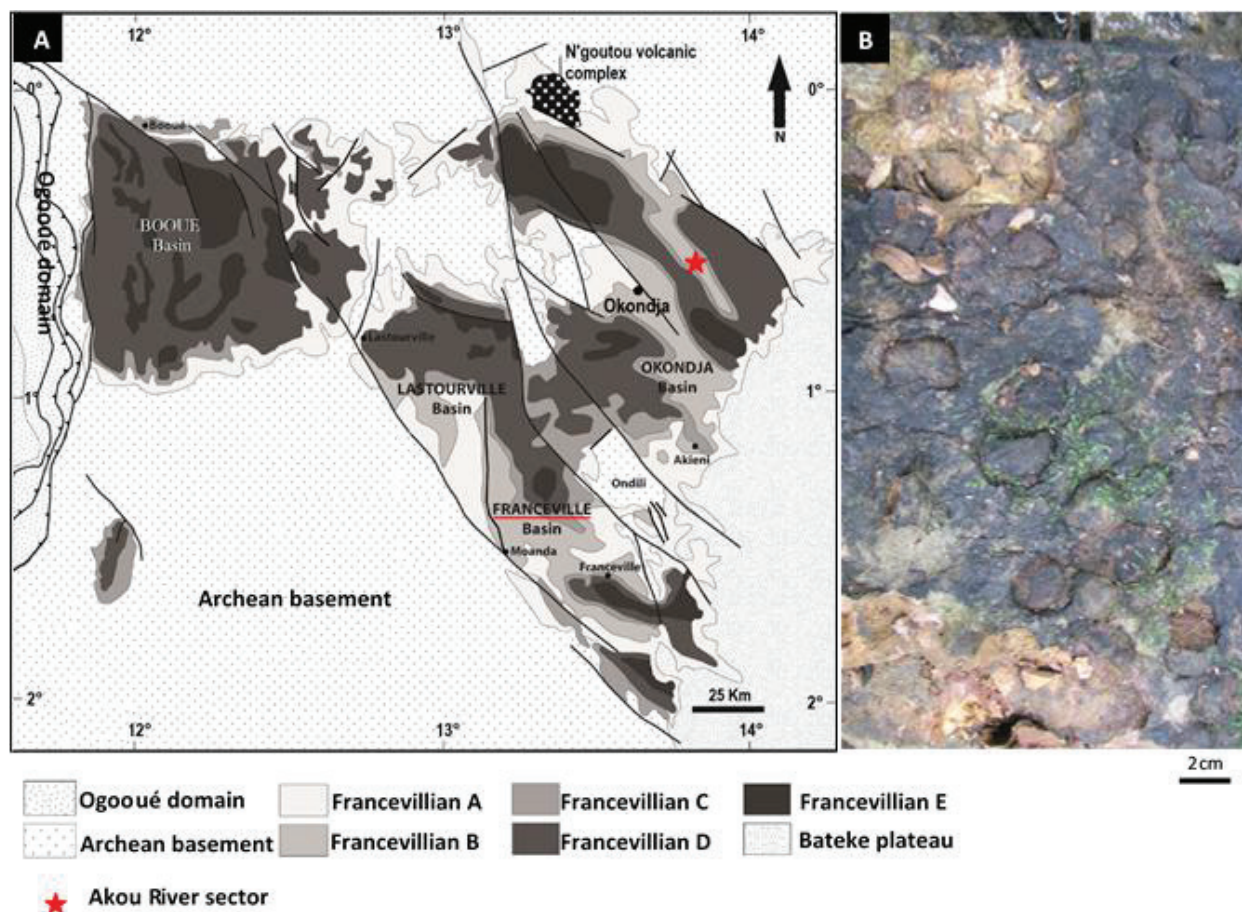


Figure S1: Geological map showing the context of fossiliferous Palaeoproterozoic rocks in Gabon. (A) Archean basement is overlain by four sedimentary basins, including the Okondja Basin which contains the Akou nodules reported here. (B) View of a bedding plane of the fossil level in the field, showing a dense packing of subspherical to elongate nodules.

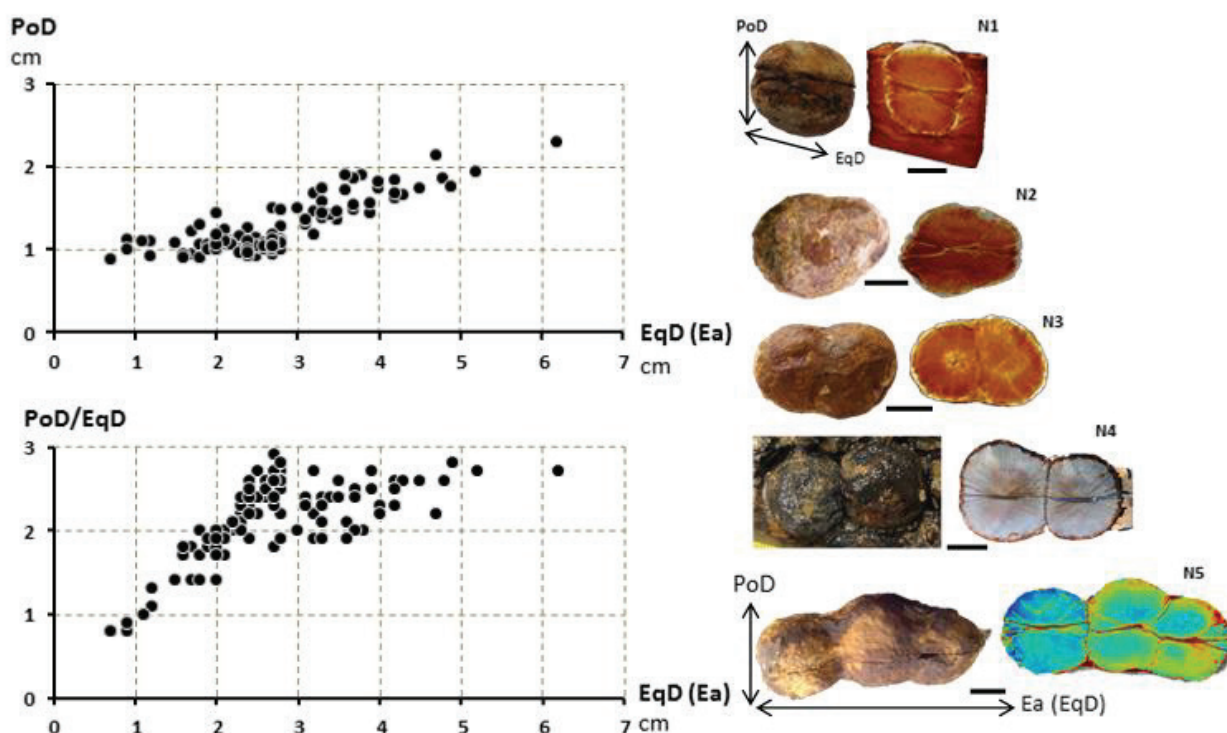


Figure S2: Graphs showing the range of polar diameter (PoD) and equatorial diameter (EqD) in the Akouemma nodules. These show a tendency for typical specimens to be ovoid (N1) and the elongated shapes showing a tendency towards lateral growth (N2-N5), “self-strangulation” (external furrow) and division (internal suture) (N3-N5). Ea: elongation axis) [8] modified. Scale bars: 1 cm.

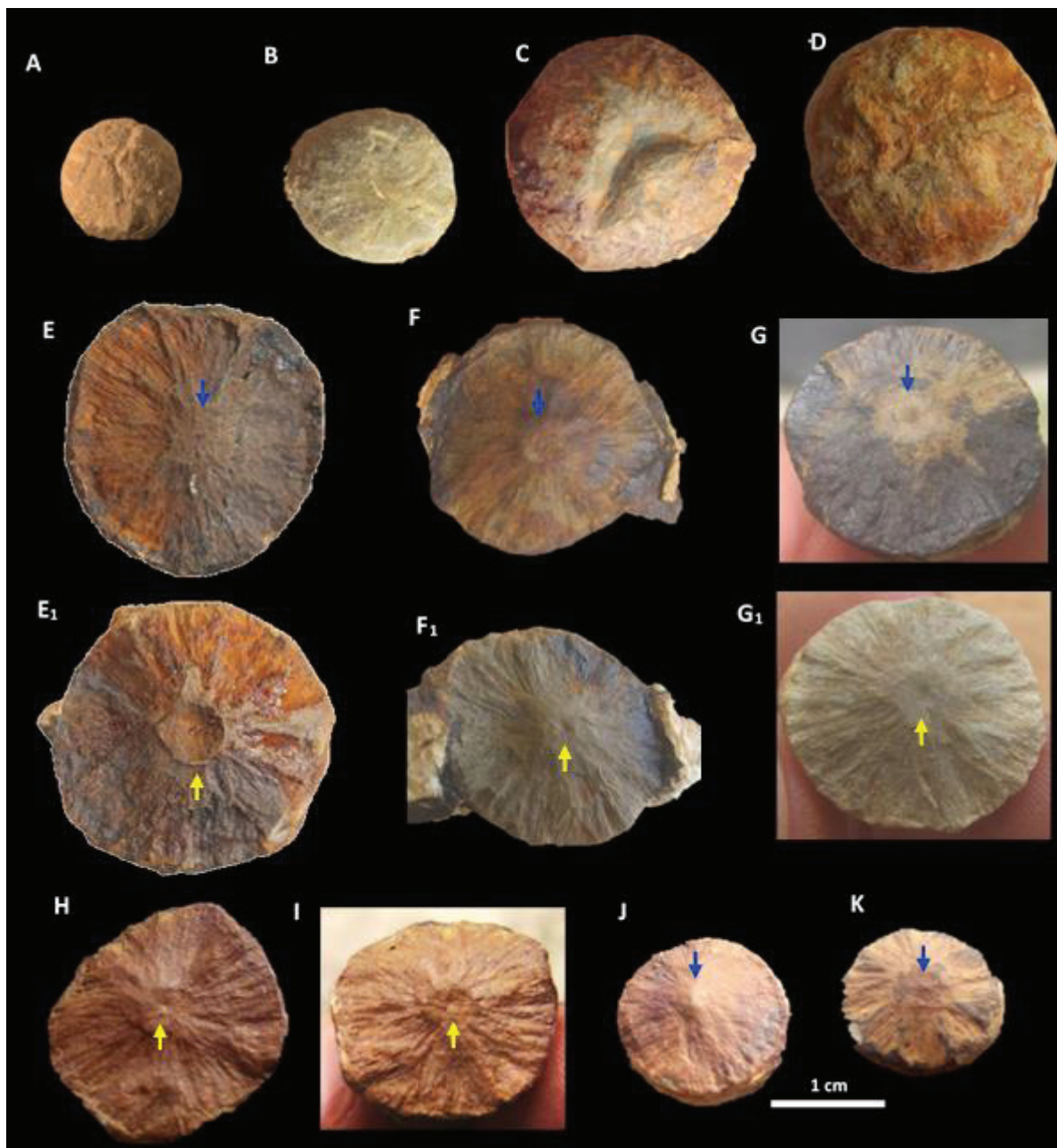


Figure S3: Morphology of the top of upper hemisphere and internal surface of hemispheres of ovoid forms nodule showing. (A-D) Views of the top hemispheres of four nodules of different sizes showing depressions around the top, dimples, lenticular shapes in relief. (E-G) Internal surface of upper hemispheres, showing radial sculpture and a central nipple-like feature (blue arrow). (E₁-G₁) Internal surface of lower hemispheres of same nodules, showing radial sculpture and a corresponding central depression (yellow arrow). The structures of the hemispheres G, G₁ of this nodule are well preserved compared to others. (H-K) Four hemispheres of four different nodules with nipple-like features and central depressions more or less well preserved.

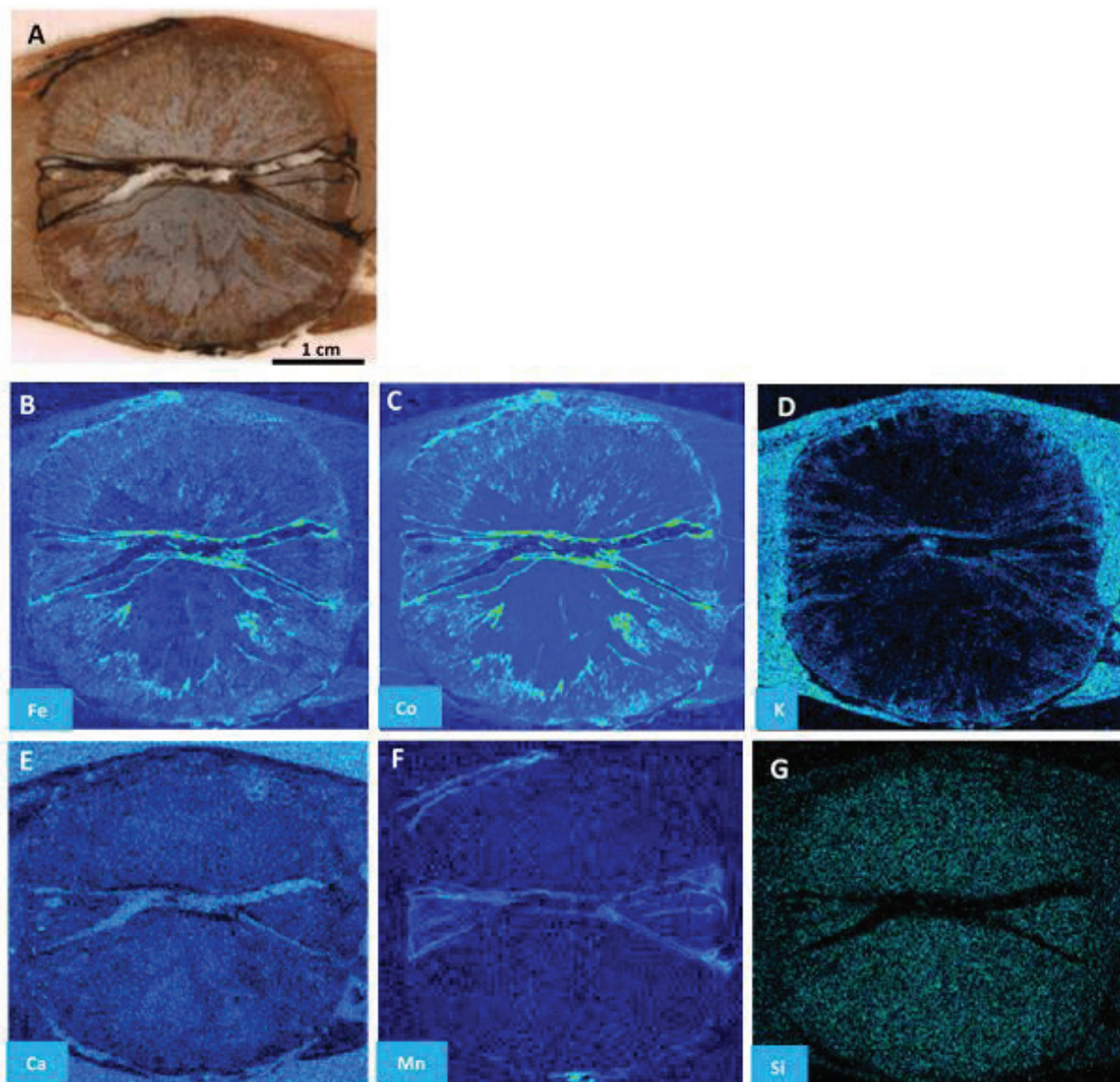


Figure S4: Images of distribution maps of chemical elements in a vertical axial section of *Akouemma* TS1 showing both hemispheres and the median disc; note the centrifugal fibro-radial system extending up into the upper hemisphere and down into the lower hemisphere. (A) BSE image. (B-G) Fe, Co, K, Ca, Mn, and Si distribution maps. The median disc, very fragile and susceptible to cracking, is highlighted by the Mn distribution map (F).

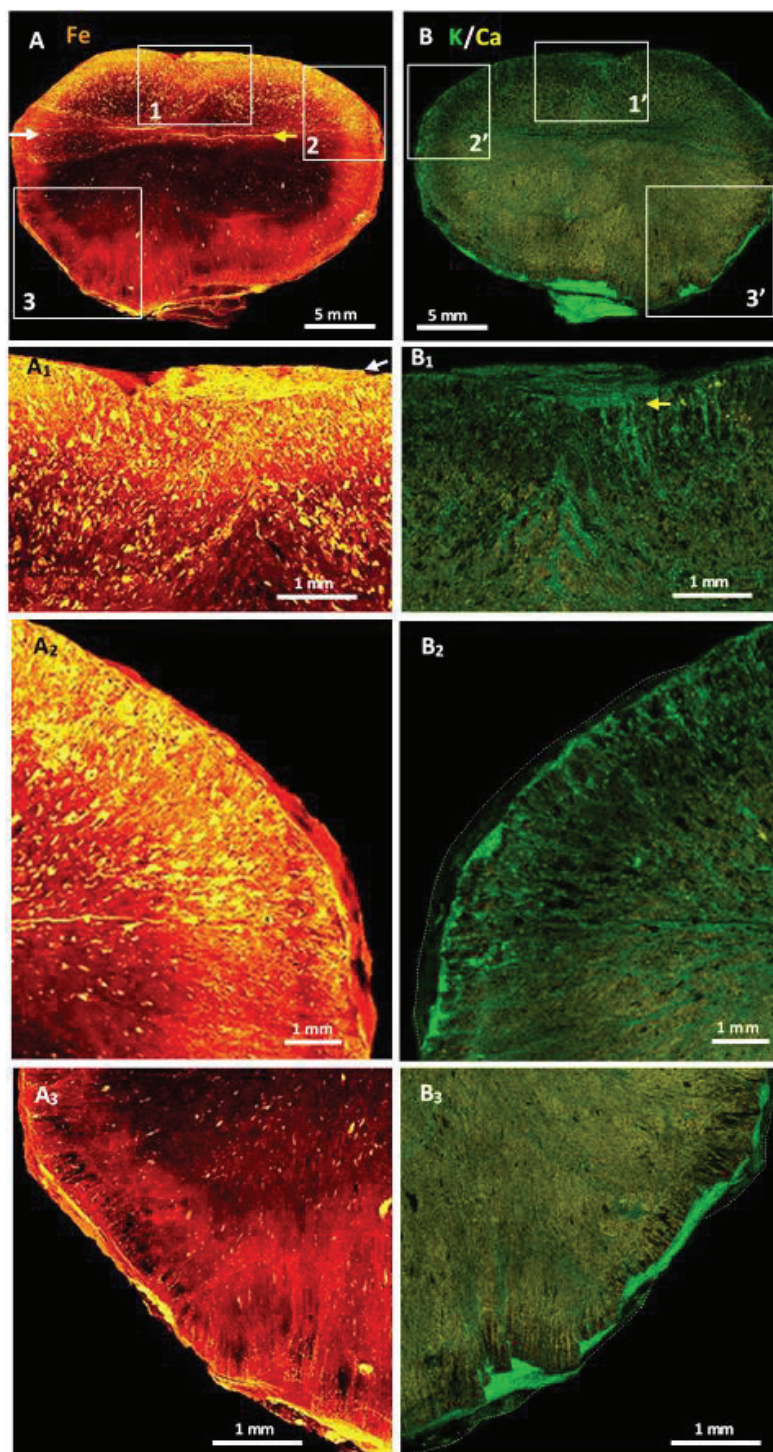


Figure S5: Particle-induced X-ray emission images of the distribution of iron, potassium and calcium in the Akou 16 nodule flattened in the upper hemisphere, highlighting its internal fibro-radial fabric and peripheral system. (A) Distribution of iron, which displays an internal radial system of fibres and particles from both sides of the median surface (yellow arrow); iron is more concentrated at the inner edge and forms a thin rim on the periphery. Note the tip of the median disc on the extreme left (white arrow). Boxes 1, 2, and 3 are shown in greater detail. (B) Distribution of potassium and calcium. Calcium has a more uniform internal distribution, whereas potassium is present in internal centrifugal fibres on either side of the median surface and forms a border around the edge of the nodule. Boxes 1', 2', and 3' are shown in greater detail. (A₁) Detail of box 1 showing a high density of iron particles and a lenticular body on the periphery (white arrow). (B₁) Detail of box 1' in the same zone showing a well-marked

radial system and the peripheral position of the lenticular body; note the flattened potassium fibres that have fossilized the deformation under the lenticular body (yellow arrow). (A₂) Detail of box 2 showing a view of both the radial and peripheral systems; note the abundance of iron particles in the radial system and the repeated patterns in the peripheral system. (B₂) Detail of box 2' in the same zone showing the two systems; the iron ring (dark green) is separated from the nodule by a thin border of potassium. (A₃) Detail of box 3 showing the radial system of denser iron filaments (a few particles are shown) and the peripheral system. (B₃) Detail of box 3' highlighting the peripheral system of repeating patterns of potassium (green) and iron (dark green).

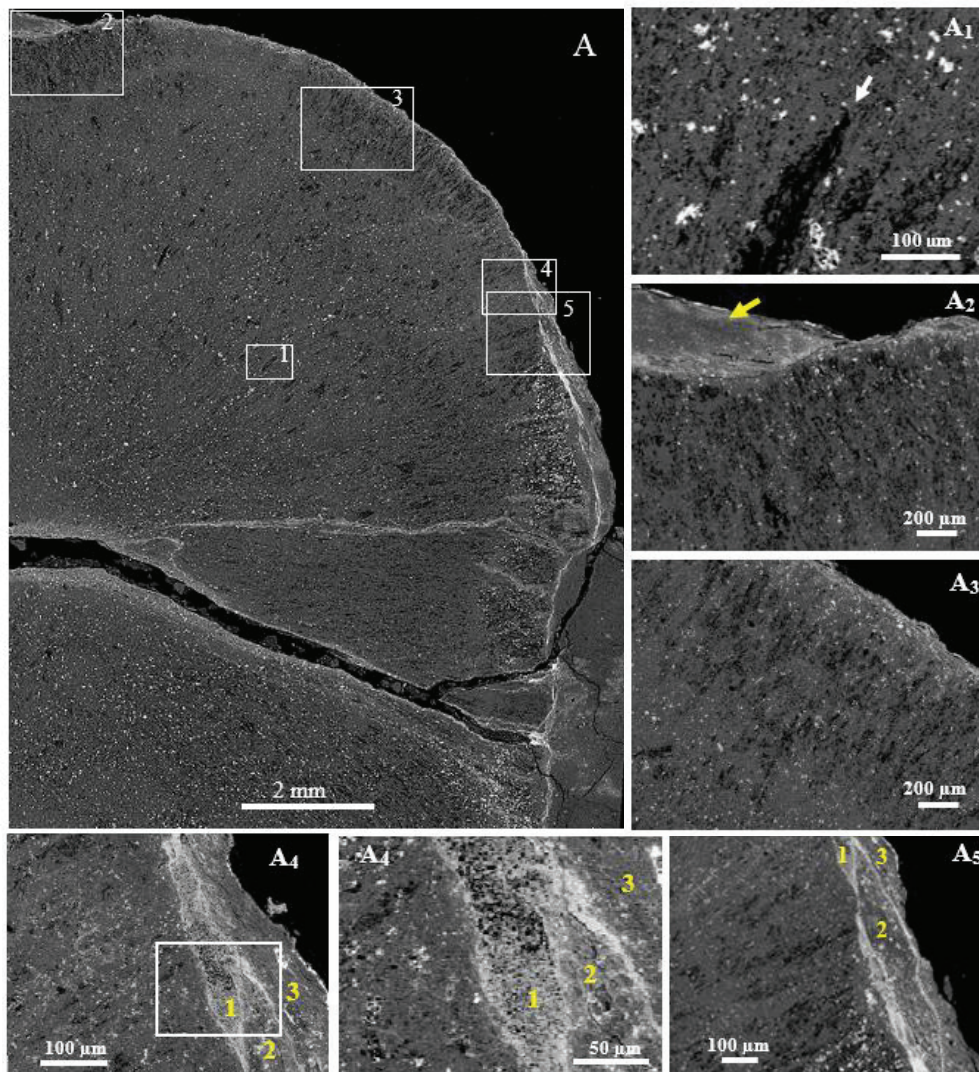


Figure S6: Scanning electron microscopic views of the internal and external aspects of an *Akouemma* nodule (Akou 3x021). (A) View of the upper hemisphere and the medial disc. The dark grey majority consists essentially of very fine silica. The light grey particles are iron, the grey particles are calcium (hardly visible), and the black areas are carbon-rich; note the radial arrangement of black lines of carbon from the centre of the medial disc to the rim of the upper hemisphere showing repeated patterns in the peripheral system similar to Figure S5A₂, A₃; iron is particularly concentrated on the edge and on the interfaces between the hemispheres and the middle disc. Images (A₁-A₈) correspond to boxes 1-8, respectively. (A₁) Magnification of the internal linear black carbon-rich area (white arrow). (A₂) Top of the upper hemisphere with a lenticular siliceous body in a depression; note the black linear pattern of carbon perpendicular to the rim. (A₃) The black pattern of carbon is densely distributed perpendicular to the rim. (A₄) View of lenticular bodies (1, 2, 3) parallel to the edge and the linear pattern of the carbon, which is always perpendicular to the rim. Note the superposition of the three lenticular bodies; the bottom one (1), in full, is 320 μm long and 40 μm thick. (A_{4a}) Details of three superimposed lenticular bodies (1, 2, 3); lenticular body (1) shows round patterns and carbon grains. (A₅) Another silicified lenticular body (2) at least 600 μm long and 95 μm thick; below, smaller iron-rich lenticular bodies and light grey iron particles can be seen in the nodule.

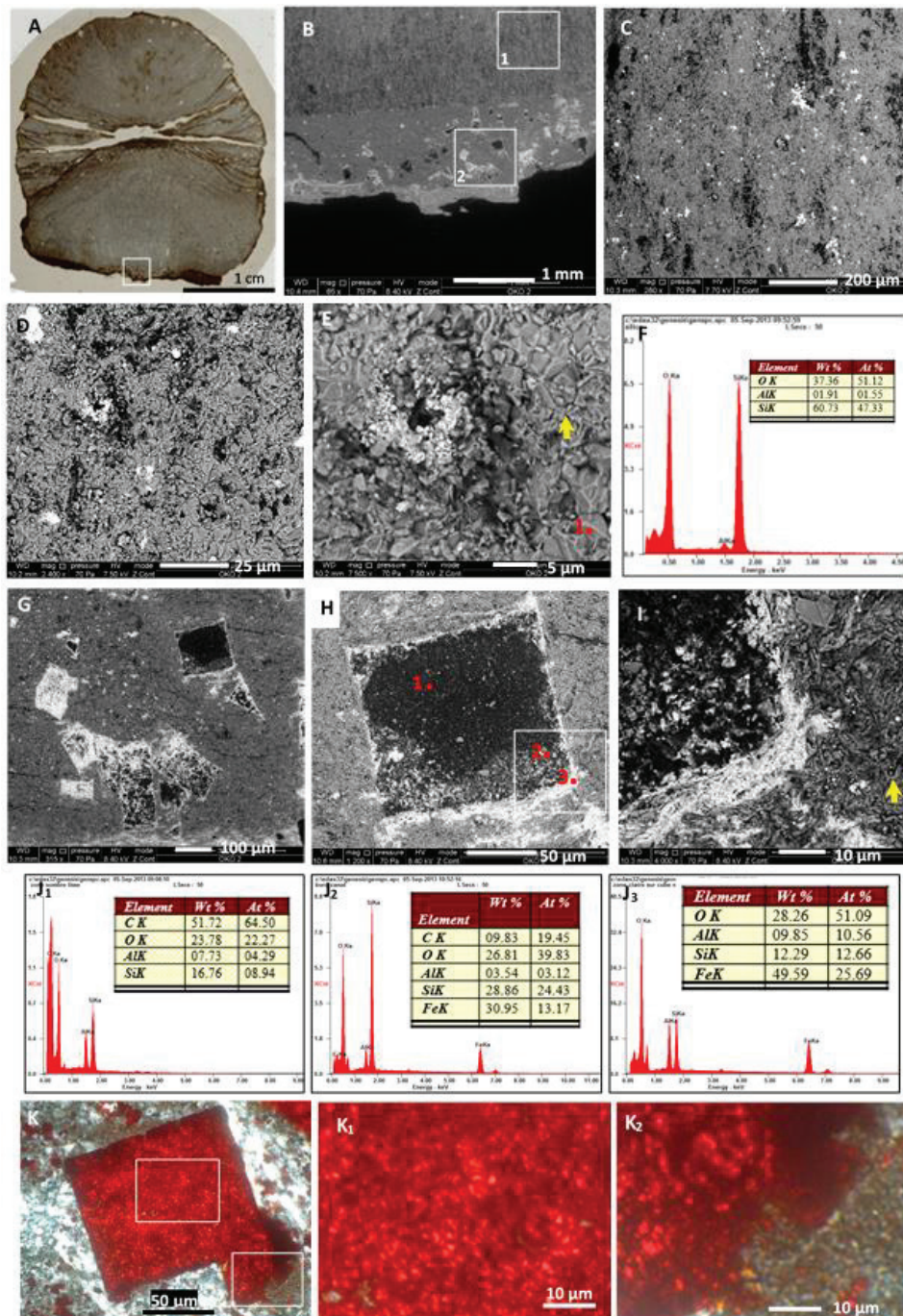


Figure S7: Some aspects of the internal structures of OKO 2. (A) Vertical section of OKO 2. The white frame on the edge indicates the area analysed. (B-I) SEM image showing in (B) the edge with two distinct zones: a radially structured zone with black traces of organic material aligned in the radial direction (Box 1) and a zone containing black and grey cubes with organic carbon and iron oxides (Box 2); the limit between the two zones is clear. (C) Detail of Box 1 showing clearly the traces of organic carbon in the radial direction and grains of iron oxide in the siliceous mass. (D) Micro-quartz siliceous background of box 1, showing in detail in (E) microcrystals of quartz approximately 2 μm in size. Analysis of point 1 indicates in (F) traces of Al in the silica. (G) Detail of Box 2 showing black organic carbon-rich cubes and light grey zones of iron oxide in a non-radial siliceous mass. (H) Detail of an organic carbon cube delimited by iron oxides. (I) Detail of the white box of (H) showing an edge of the cube in a siliceous mass with interlaced filaments (yellow arrow). The analyses of points 1, 2, and 3 are represented

in (J₁), (J₂) and (J₃). (K) "Cube" with red particles in the siliceous mass; note the net limit of the edges (AKOU 14 crossed nicols). (K₁) Magnified image of box 1 of the cube centre. (K₂) Magnified image of box 2 of the degraded border, revealing yellow-orange to greenish granules.

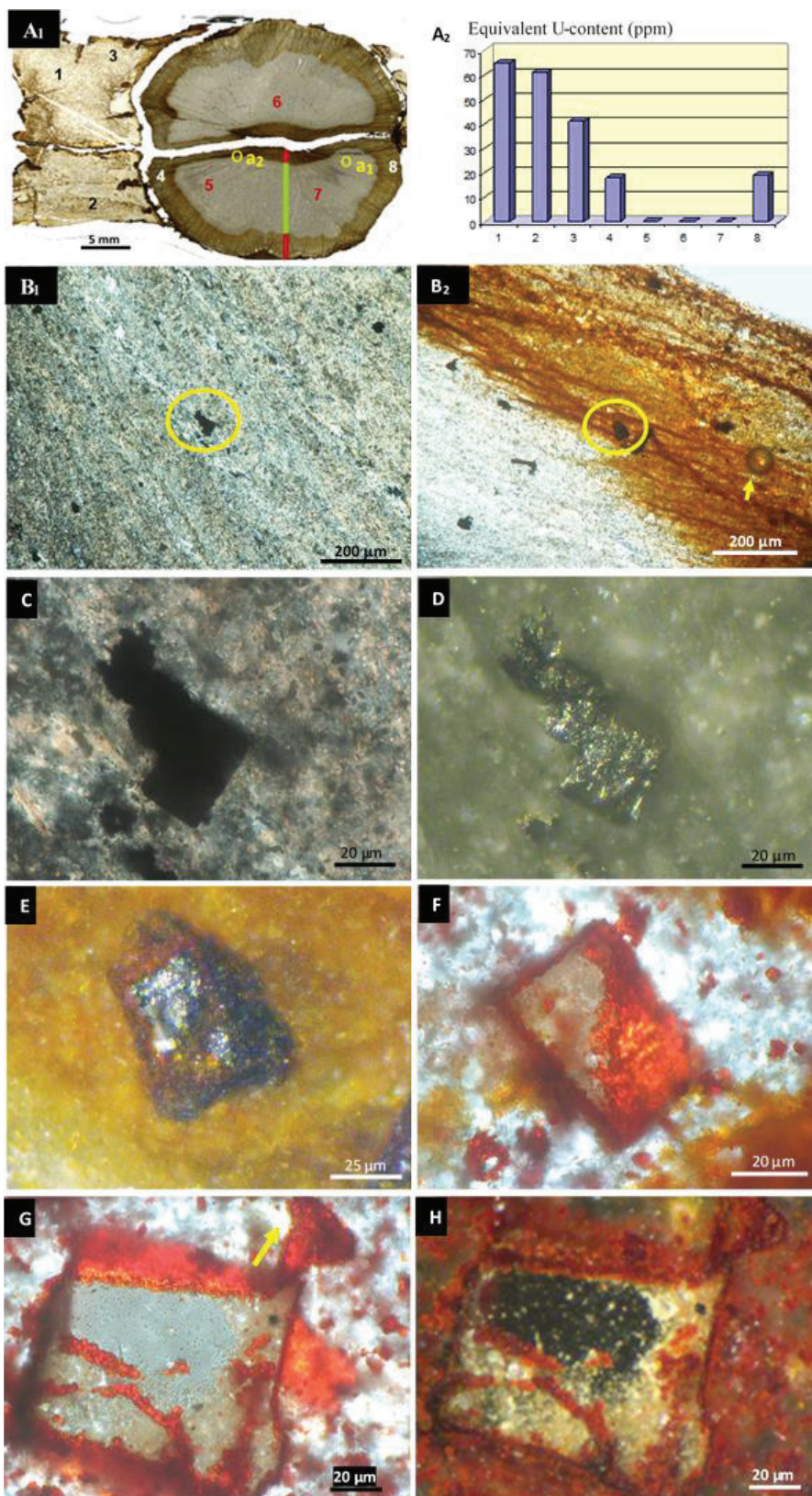


Figure S8: Radioactivity in AKOU 15 nodule and examples of pyrite and bricks with siliceous walls within the nodules. (A₁) Vertical section of AKOU 15 nodule with the gangue showing dark staining of the altered median

zone and the altered inner rim (0.2 mm wide); points 1 to 8 are analysis points of radioactivity. (A₂) Equivalent U-content (ppm) of points 1 to 8. (B₁) Thin section showing an unaltered internal zone with clay “channels” associated with opaque pyrite crystals, (circle a₁ in A₁, AKOU 15, crossed nicols). (B₂) Thin section showing an oxidized inner edge region with opaque crystals of pyrite and iron oxide; note the presence of an oblong shape with a pointed tip (white arrow) (circle a₂ in A₁, AKOU 15, crossed nicols). (C) Magnification of an opaque crystal of pyrite in the siliceous mass associated with clay minerals in ‘A’ (crossed nicols). (D) Magnification of the same crystal of unaltered pyrite; note the bristled surface of the crystal with particles in a vertical position (reflected light). (E) Magnification of the pyrite crystal in the oxidation process of ‘B’; note the surface bristling with light grey particles that are more or less aligned. (F) A brick with a siliceous wall showing a surface bristling with yellow-orange to red particles that are more or less aligned, as in figure (E) (AKOU 14, crossed nicols). (G) Another brick with a siliceous wall containing red particles that are aligned at the surface, note the “spreading” of the red particles out of the brick (yellow arrow) (AKOU 14, crossed nicols). (H) Same brick in reflected light showing black carbon particles in a siliceous wall delimited by red particles.

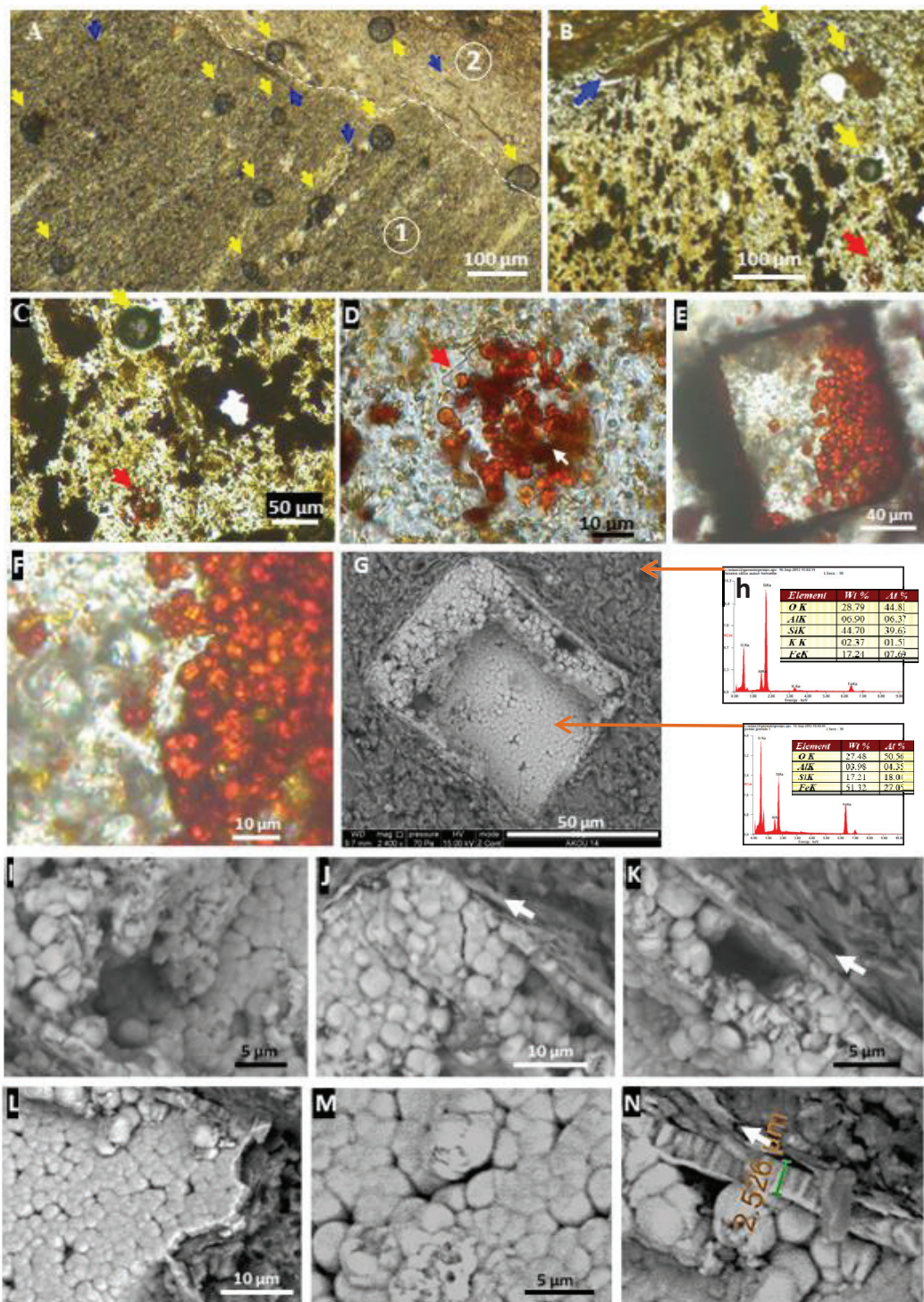


Figure S9: Oblong shapes, ferruginized spherules and particles contained in oblong forms, and ‘bricks’ in AKOU 14. (A-C) Microscopic views of oblong shapes along the transverse plane (yellow arrow); oblong-shaped bodies are dispersed in the specimen. The white dashed line separates the weathered edge (2) from the healthy part (1) (parallel nicols). Note the filaments disposed in the radial direction and intersecting this radial direction (blue arrows). (B-C) Among the oblong shapes, one contains red spherules (red arrow, parallel nicols). (D) Magnification of red spherules (cell-like) contained in a translucent silica wall and ending in a pointed tip (white arrow). (E) Microscopic

view of a silica 'brick' that contains and has on its surface greenish to red spherules; as in (D), the reddening of the spherules is not diffuse, suggesting ferruginous mineralization of these particles and spherules. (F) Magnification of greenish and red spherules on the surface of silica 'brick', some ones are decayed. (G) Scanning electron microscopic views of a 'brick' containing ferro-silico-aluminous spherules approximately 2-5 μm in size in the siliceous mass; note the regular arrangement of these particles. (H) SEM analysis of siliceous mass and spherules. (I-N) Detailed view of various aspects of the particles; note in (N) the 2.5- μm -thick ferro-siliceous wall lined on the inside by a thin ferruginous layer and the perpendicular disposition towards the exterior of rods of substantially the same size. (A-F: parallel nicols).

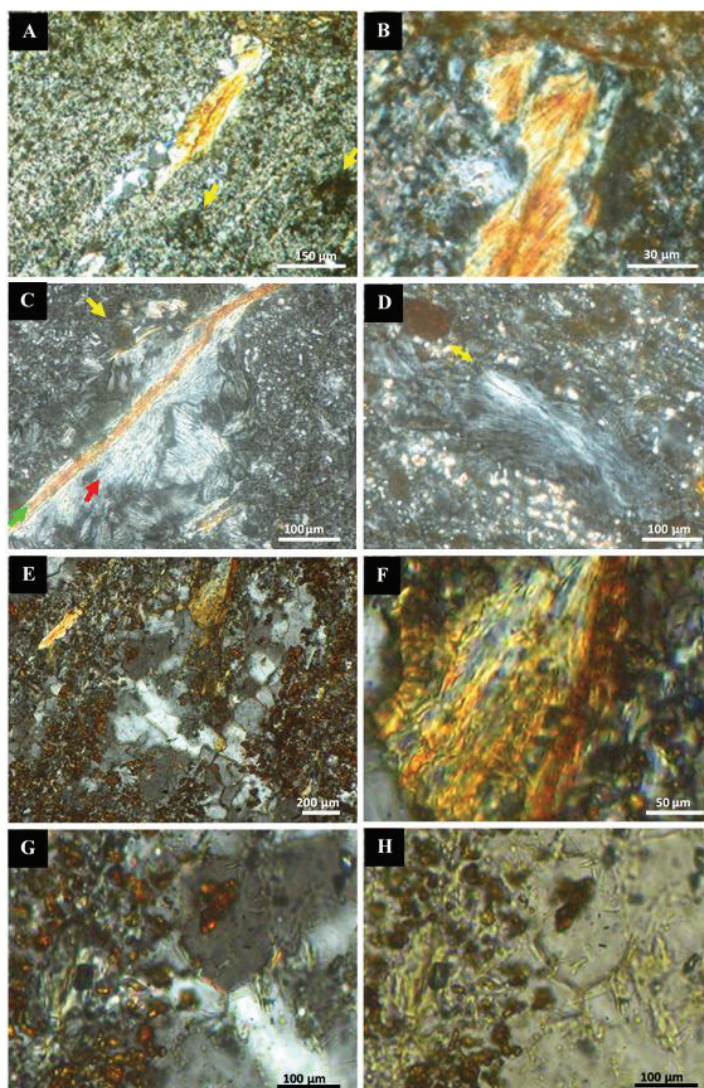


Figure S10: Various aspects of neof ormation clay minerals and other particles caught up in the micro-quartz crystals. (A) View of a yellow-orange elongated lepidocrocite similar to the silica lenticular bodies; note the alignment of dark oblong forms (yellow arrow) (Akou 16, crossed nicols). (B) Zoom of the lepidocrocite (high birefringence). (C) View of a yellow-orange filament of lepidocrocite >500 µm in length (green arrow) and a neof ormation kaolinite (red arrow); note the dark grey oblong forms along the transverse plane (yellow arrow). (D) Neof ormation clay (kaolinite) that contains conserved elongated lenticular bodies aligned with a brown oblong form (organic matter, yellow arrow). (E) View of the yellow-orange lepidocrocite, brown oblong particles (organic matter), and lenticular body aligned in the same direction and embedded within the micro-quartz crystals. (F) Detailed view of the lenticular body; note the alignment of lepidocrocite fibres on the surface and the internal arrangement of black carbon particles. (G-H) Detailed view of clay minerals, brown oblong particles embedded within the micro-quartz crystals. (A-G: crossed nicols; H: parallel nicols).

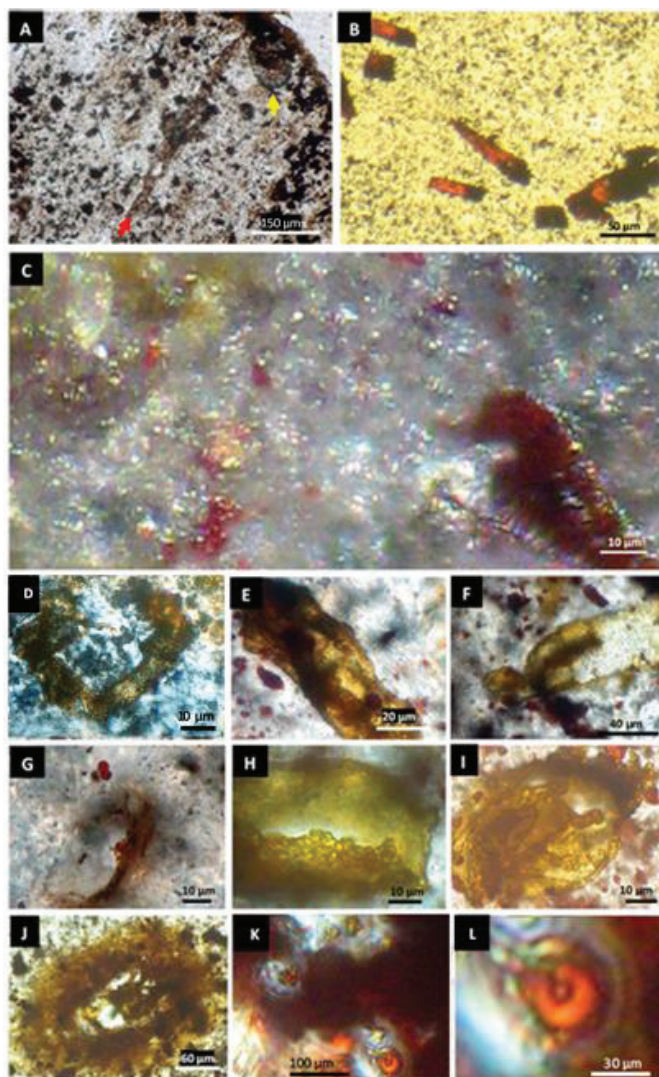


Figure S11: Linear, broken and decayed tubules, cell-like particles, and oblong shapes observed in the nodules. (A) Microscopic view of a linear tubule more than 5 mm in length in the radial direction (red arrow); note the presence of an oblong-shaped biomorph (yellow arrow). (B) Microscopic view of ferruginized broken tubules dispersed in the siliceous mass, suggesting fluidity prior to silicification. (C) Microscopic view of an organized decaying ‘multicellular’ structure with cell-like dispersion; this dispersion is limited (the detached ‘cells’ retain a certain alignment) in that it can only occur in a more or less viscous medium prior to silicification. (D-J) Various fragments of broken tubules, in decaying colored green to rust-brown likely remains mineralized of algae; note the granular walls. (K) Silico-ferruginous mass containing green and red oblong shapes well preserved. (L) Magnification of red oblong-shaped form with a pointed tip, note the net limit of the edge (C, K, L: crossed nicols; D: analysed crossed nicols, A-B, E-J: parallel nicols).

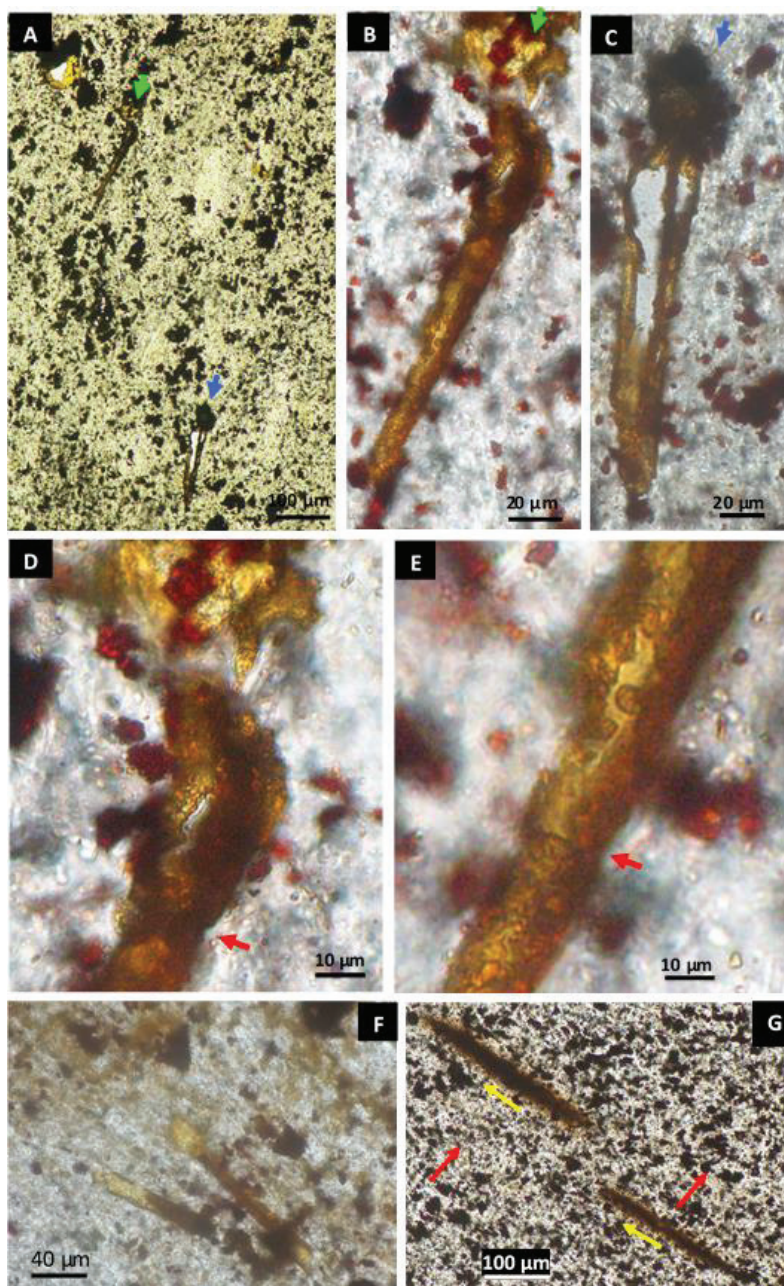


Figure S12: Other tubule features observed microscopically. (A) Views of two similar tubules in the siliceous mass associated with dark and yellow particles and areas. (B-C) Magnification of tubules showing rods, bulges and tufts probably of biologic origin (algae?). (D-E) Details of the tuft, bulges and the rod of the tubule (B); note the granulated wall and circular boundaries (red arrows), suggesting fitted-together parts. (F) Decaying parallel green filaments in the siliceous mass. (G) Elongated tubular shapes and dark particles in the siliceous mass; note two perpendicular directions (red and yellow arrows). (A-G: parallel nicols).

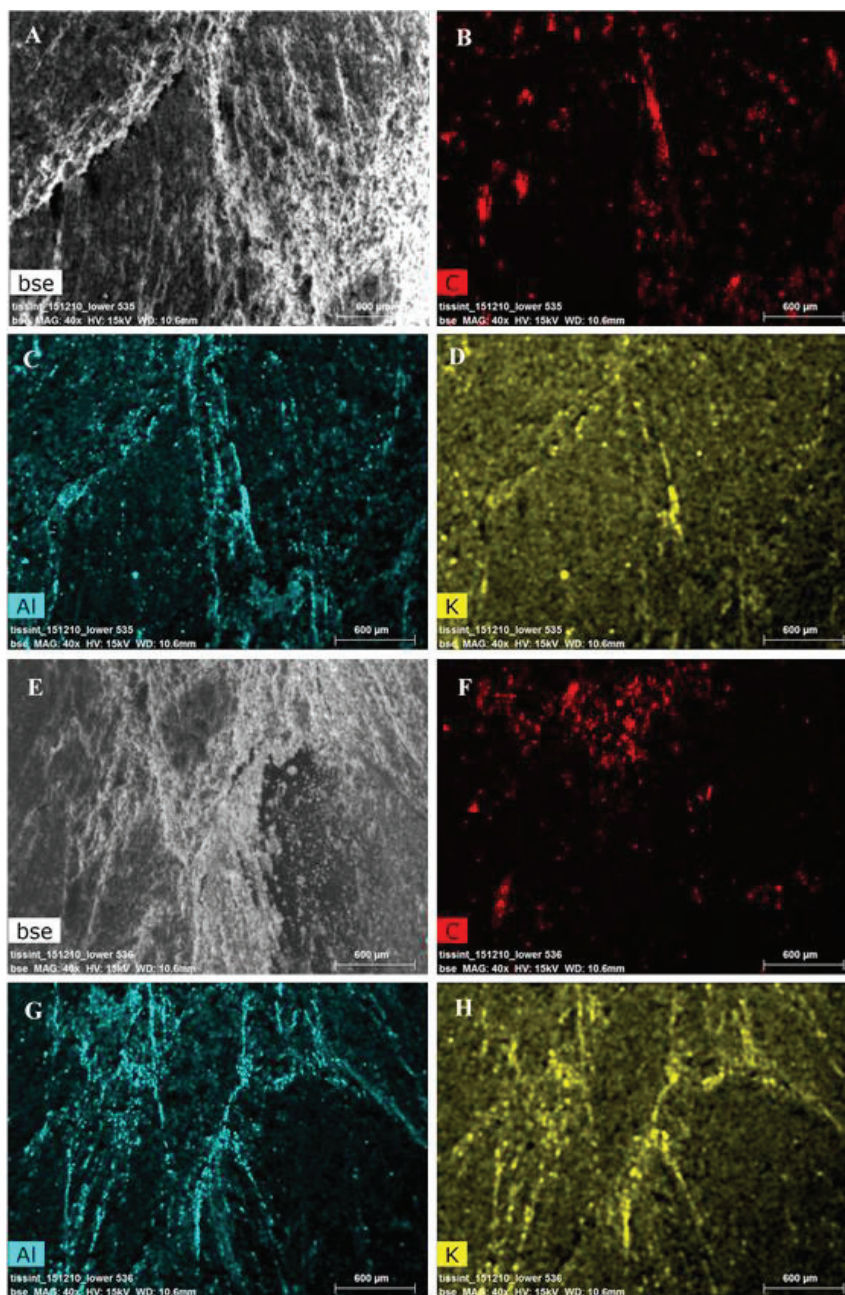


Figure S13: Internal fibro-radial fabric and chemical elements distribution map in *Akouemma* TS1. (A, E) BSE images showing the fibrous fabric. (B, F) Carbon distribution map. (C, G) Aluminum distribution map. (D, H) Potassium distribution map. Note the perfect superimposition of aluminum and potassium distribution maps with BSE images and the disposition of particles and carbon filaments more or less surimposable to aluminum and potassium.

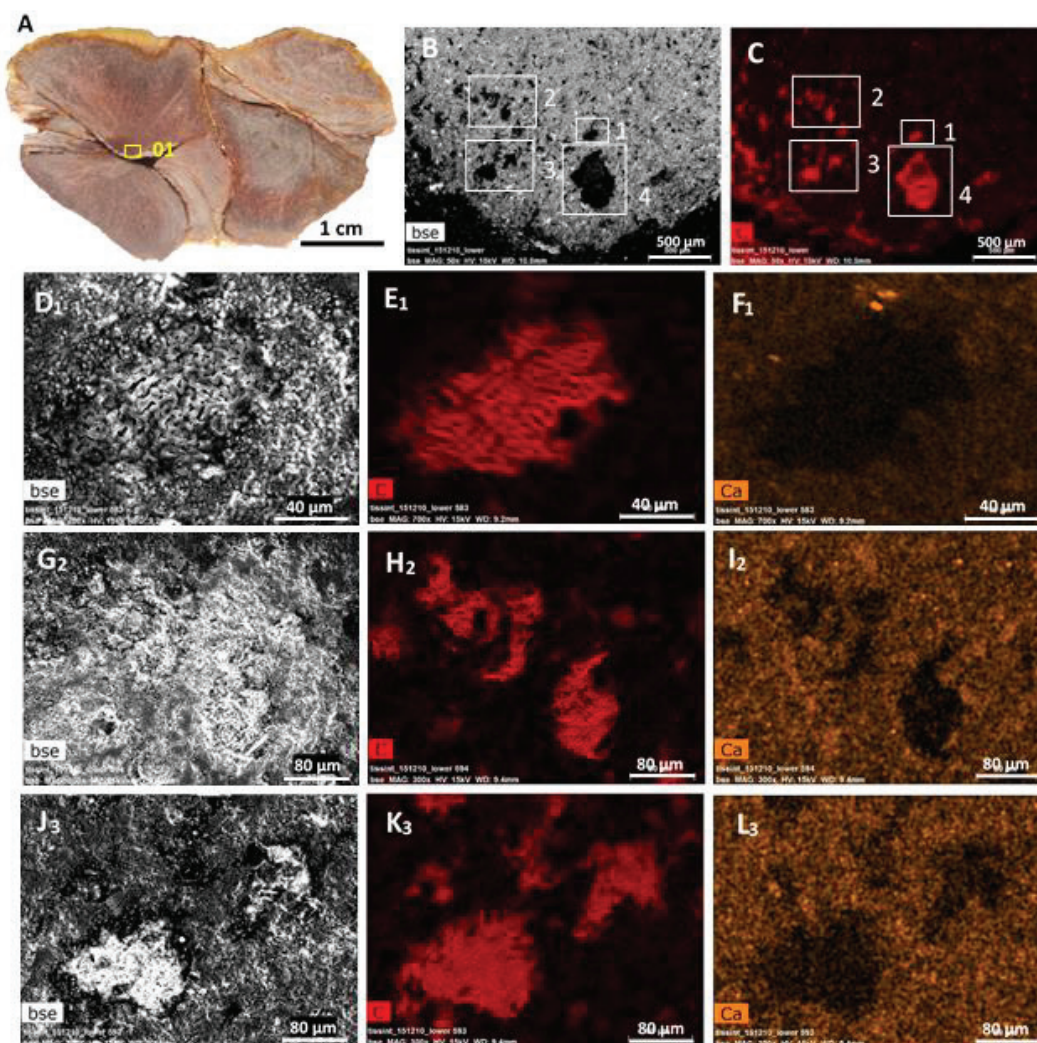


Figure S14: Internal structures of contiguous and deformed nodules of *Akouemma 2nd*. (A) Zone 1, cone of the upper hemisphere. (B) BSE image showing a centrifugal uniform radial system dotted with black spots distributed largely in the radial direction. (C) Carbon distribution map showing areas of concentration corresponding to the black spots in image (B). (D₁-F₁) Magnification of box 1. (D₁) BSE image showing a labyrinthine structure (E₁) Carbon distribution map showing a regular pattern structure. (F₁) Calcium distribution map showing grains a few microns in size around a calcium-free zone in the form of the carbon mass. (G₂-I₂) Magnification of box 2. (G₂) BSE image showing a highlighted xenomorphic structure. (H₂) Carbon distribution map showing vacuolar funnel-shaped bodies. (I₂) Calcium distribution map showing grains of a few microns around a calcium-free zone in the form of the carbon mass. (J₃-L₃) Magnification of box 3. (J₃) BSE image showing two highlighted encrusted bodies. (K₃) Carbon distribution map showing bodies with arrow-like shapes. (L₃) Calcium distribution map showing grains a few microns in size around a calcium-free zone in the form of the carbon mass.

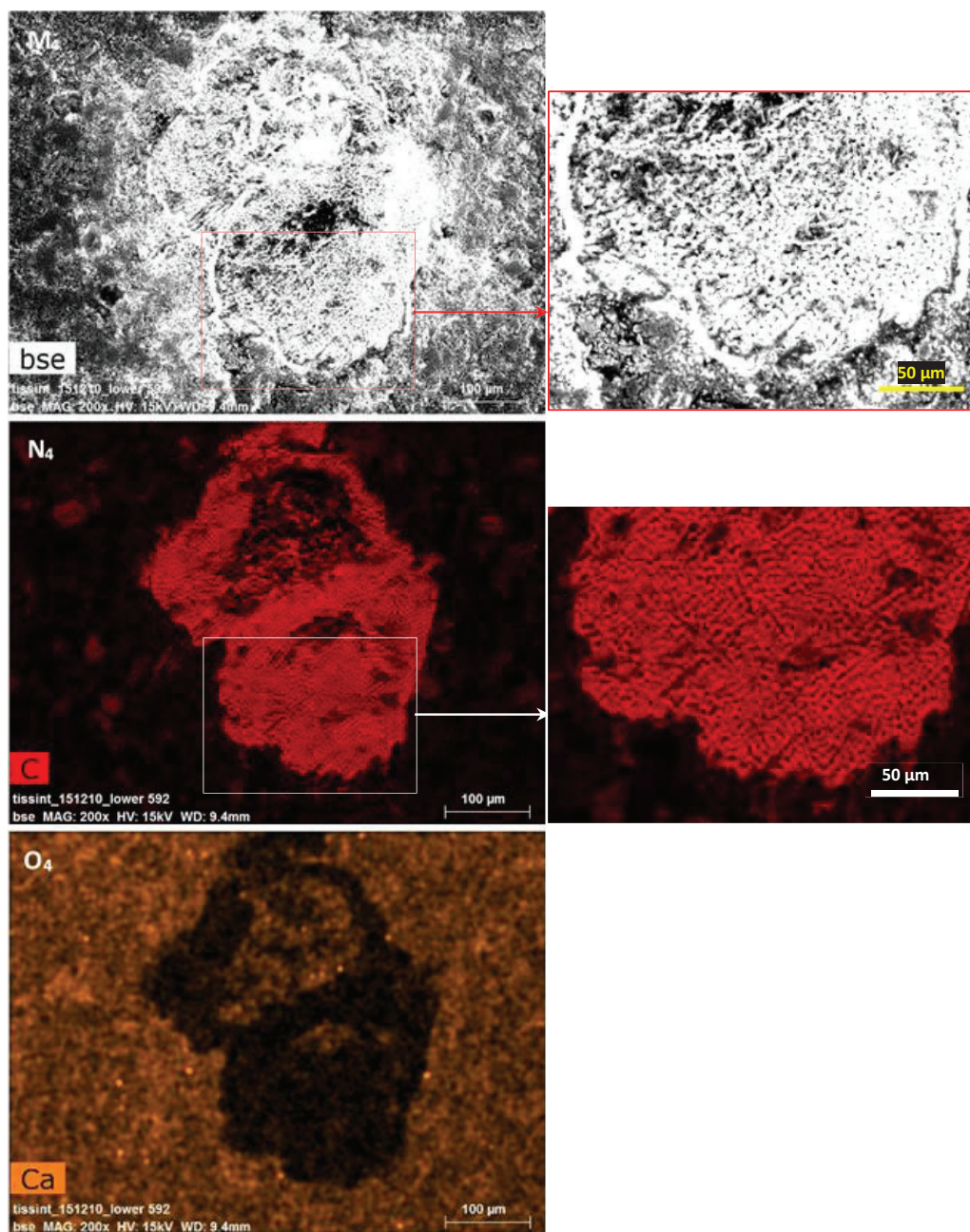


Figure S14: bis-(M₄-O₄) Magnification of box 4. (M₄) BSE image showing a highlighted circular shape. (N₄) Carbon distribution map showing an elongated xenomorphic mass with fine patterns. (O₄) Calcium distribution map showing grains a few microns in size around a calcium-free zone in the form of the carbon mass. All of the distribution maps of the chemical elements show the same configuration with respect to the carbon mass.

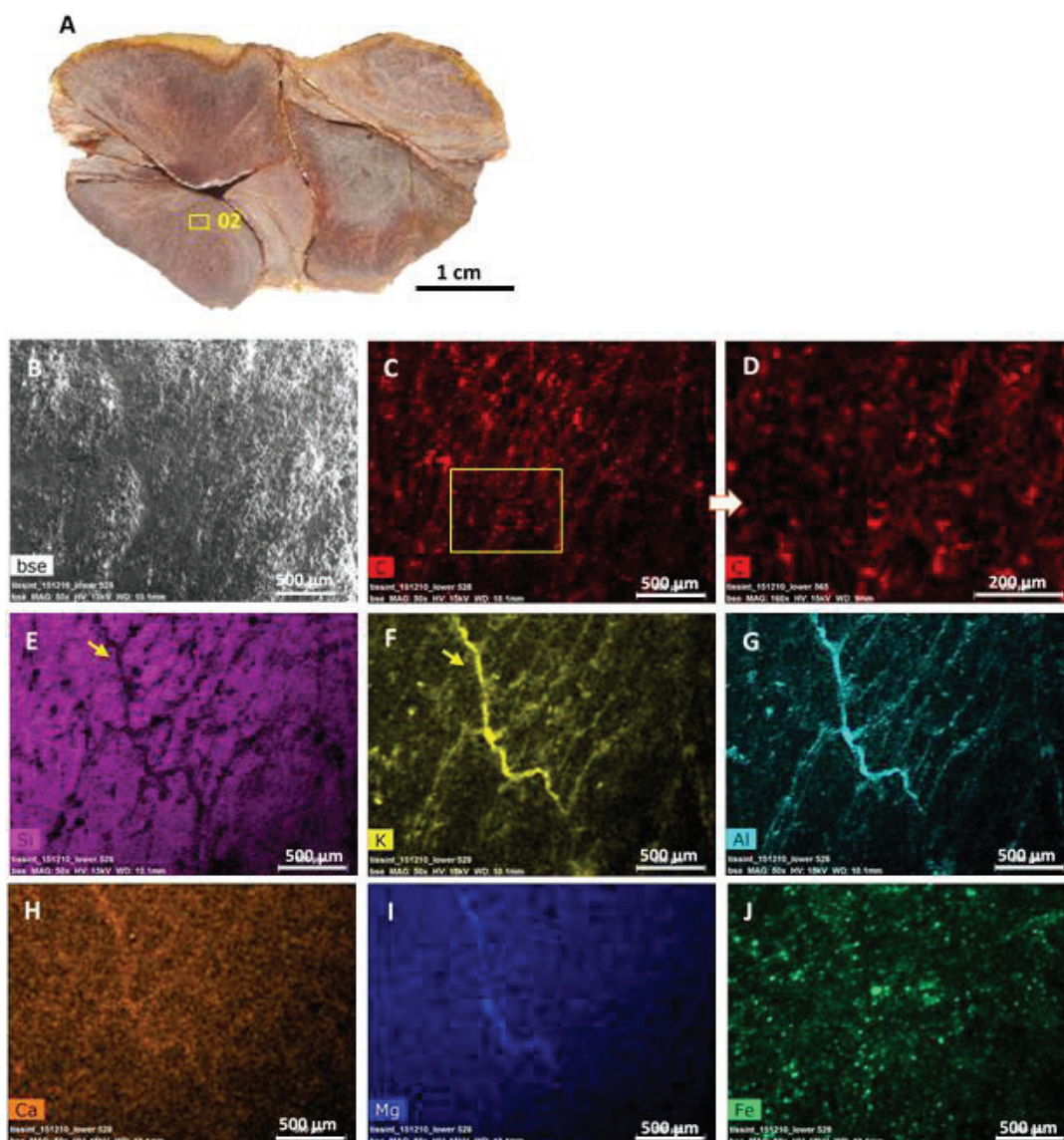


Figure S15: Internal structures of contiguous and deformed nodules of *Akouemma 2nd1*. (A) Undeformed zone 2 of the lower hemisphere, presenting a fibrous structure in ‘tufts’ and ‘ramps’. The fibrous structure, which is barely visible on the BSE image (B), is highlighted by linear carbon fibres (C-D) in the radial direction. Dark traces in the silicon, and particularly aluminum and potassium images (E-G), highlight not only filaments that are superimposed on the carbon fibres but also the limits of the ramp structure. This structure is barely made visible by calcium (H). Magnesium (I) is just visible at the limits of a ramp. Iron (J) generally follows the orientation of the carbon fibres.

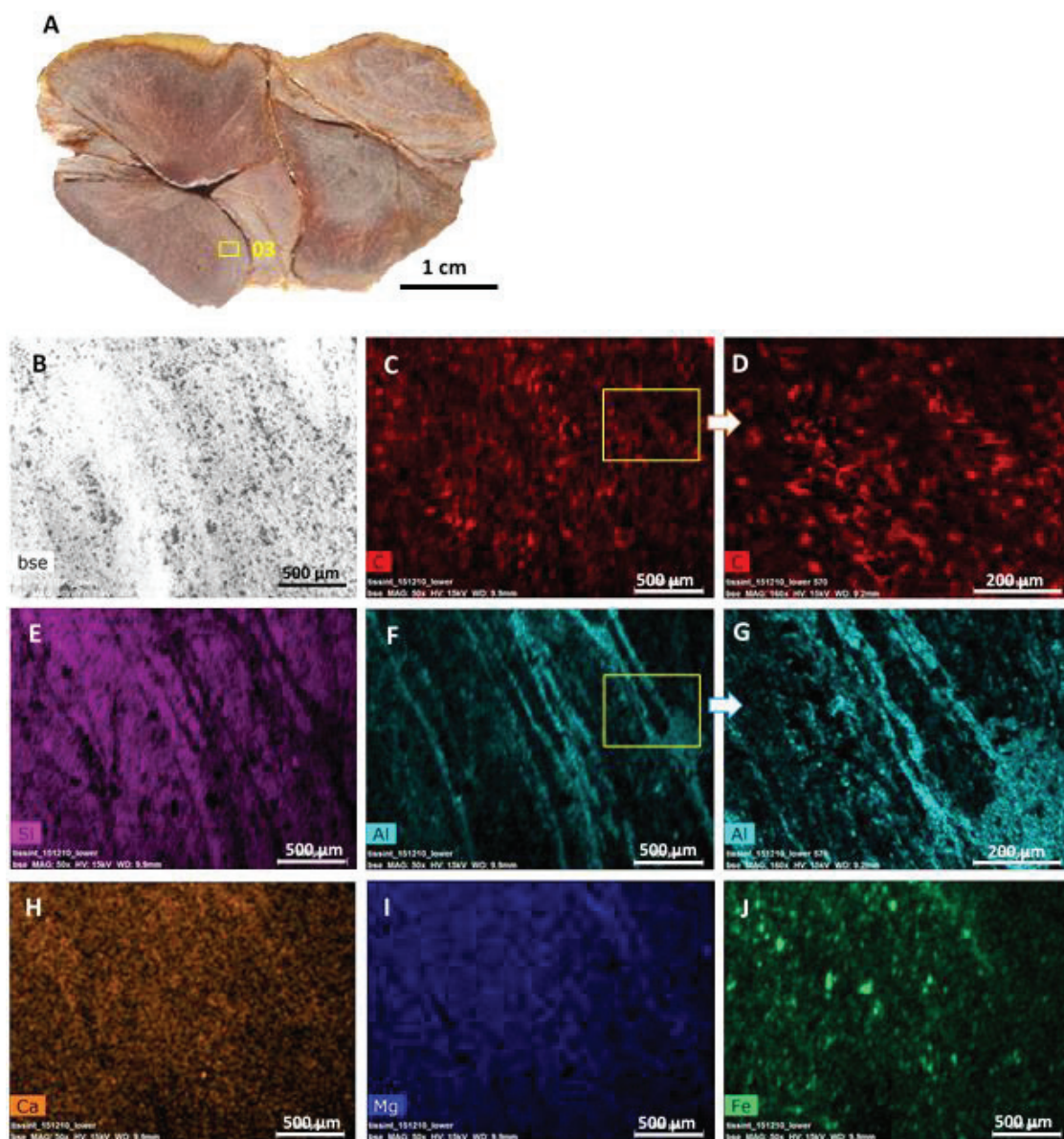


Figure S16: Internal structures of contiguous and deformed nodules of *Akouemma 2nd1*. (A) Zone 3 is deformed, showing a flexed structure. (B) BSE image showing an entire zone bent in the orientation of carbon particles (C-D). The carbon particles are arranged in the same manner as the BSE image. (E-G) Curved linear structures are highlighted by dark traces on the siliceous mass (E) and by aluminum distribution maps (F-G) that present filaments and hollow tubules. (H-I) Calcium and magnesium distribution maps show a structure that is barely visible. (J) The iron particles are oriented in two directions; one is oriented along the bent structure, the other in an oblique direction.

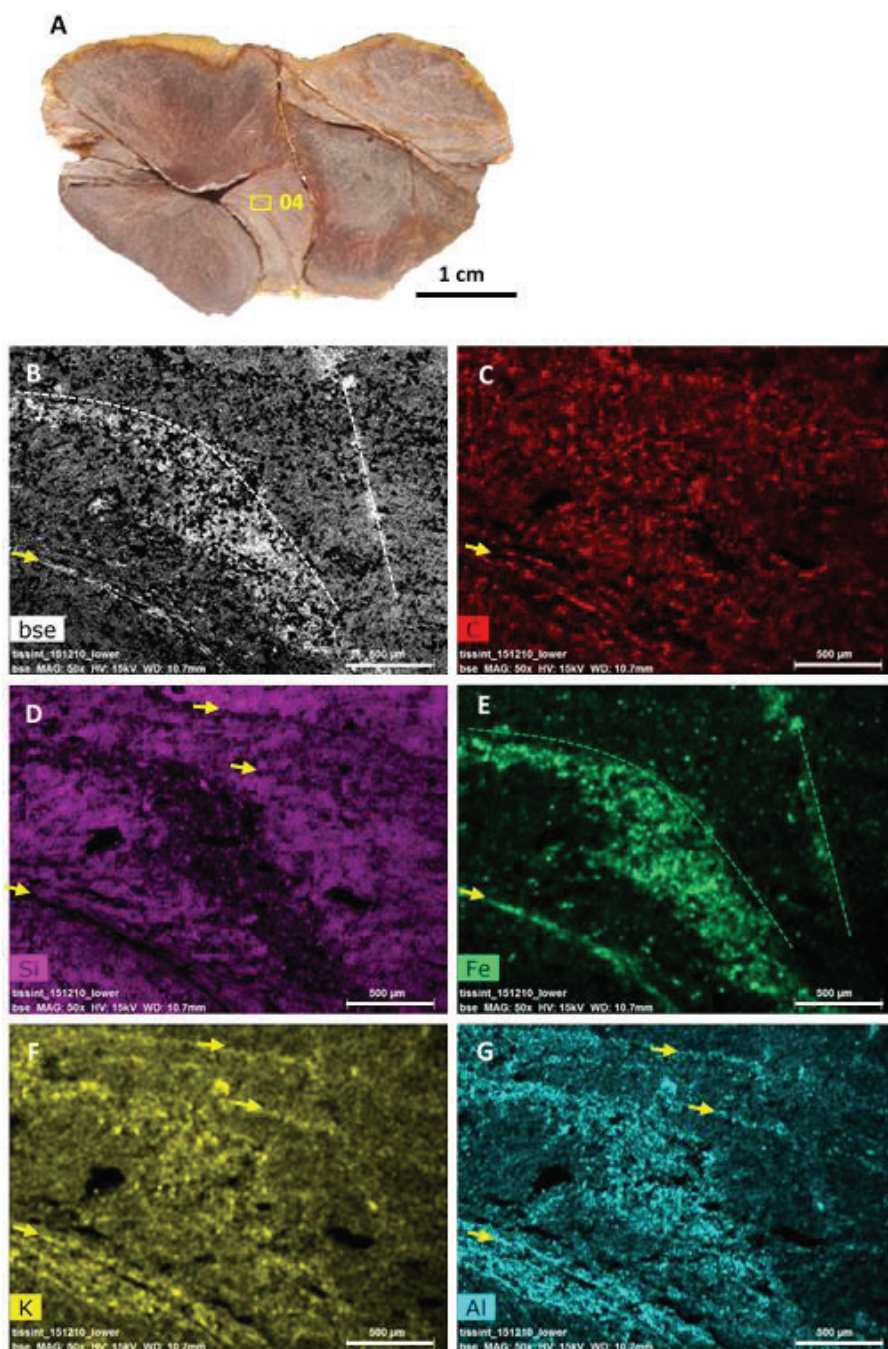


Figure S17: Internal structures of contiguous and deformed nodules of *Akouemma 2nd₁*. (A) Zone 4, compressed median disc. (B-G) All carbon, silicon, iron, potassium and aluminum distribution maps, including the BSE image, show the same deformation, with linear fibrous structures (filaments) at the lower left (yellow arrow), a turbulent zone with disorganized carbon particles above, and at least three planes with breaks in the slope (dotted lines). This suggests compression running from right to left.

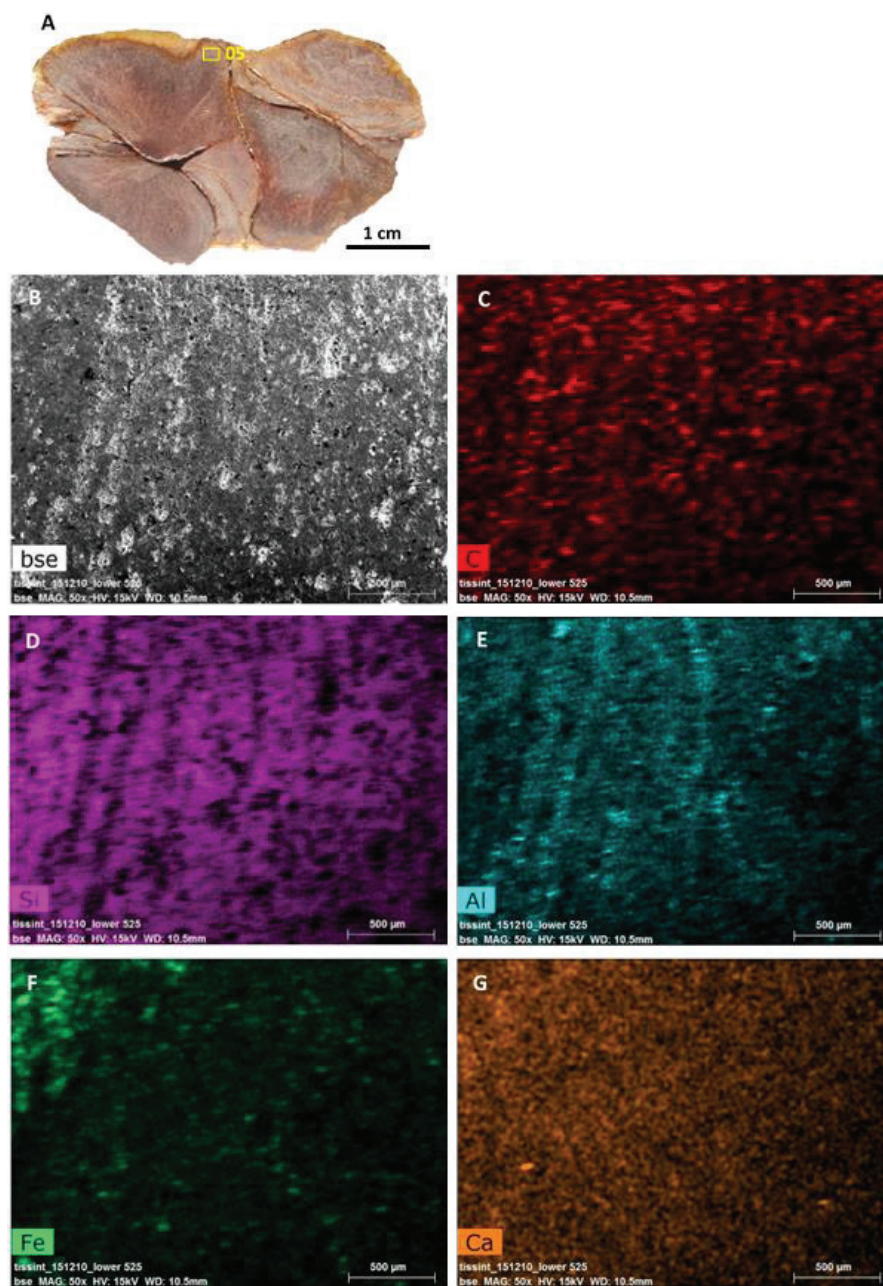


Figure S18: Internal structures of contiguous and deformed nodules of *Akouemma 2ndi*. (A) Zone 5, which is compressed in the upper hemisphere. The compression zone 5 is accompanied by a reorganization of the internal structure. (B) BSE image showing discontinuous vertical structures. (C) The carbon distribution map shows vertically aligned and laterally stretched particles. (D) Dark vertical lines and lateral micro-shears in the siliceous mass. (E) Aluminum highlights straightened filaments that have been laterally micro-sheared off. (F-G) These deformations are very poorly (or not at all) recorded by iron and calcium. Note the similarities between the distributions shown in maps Al and C.

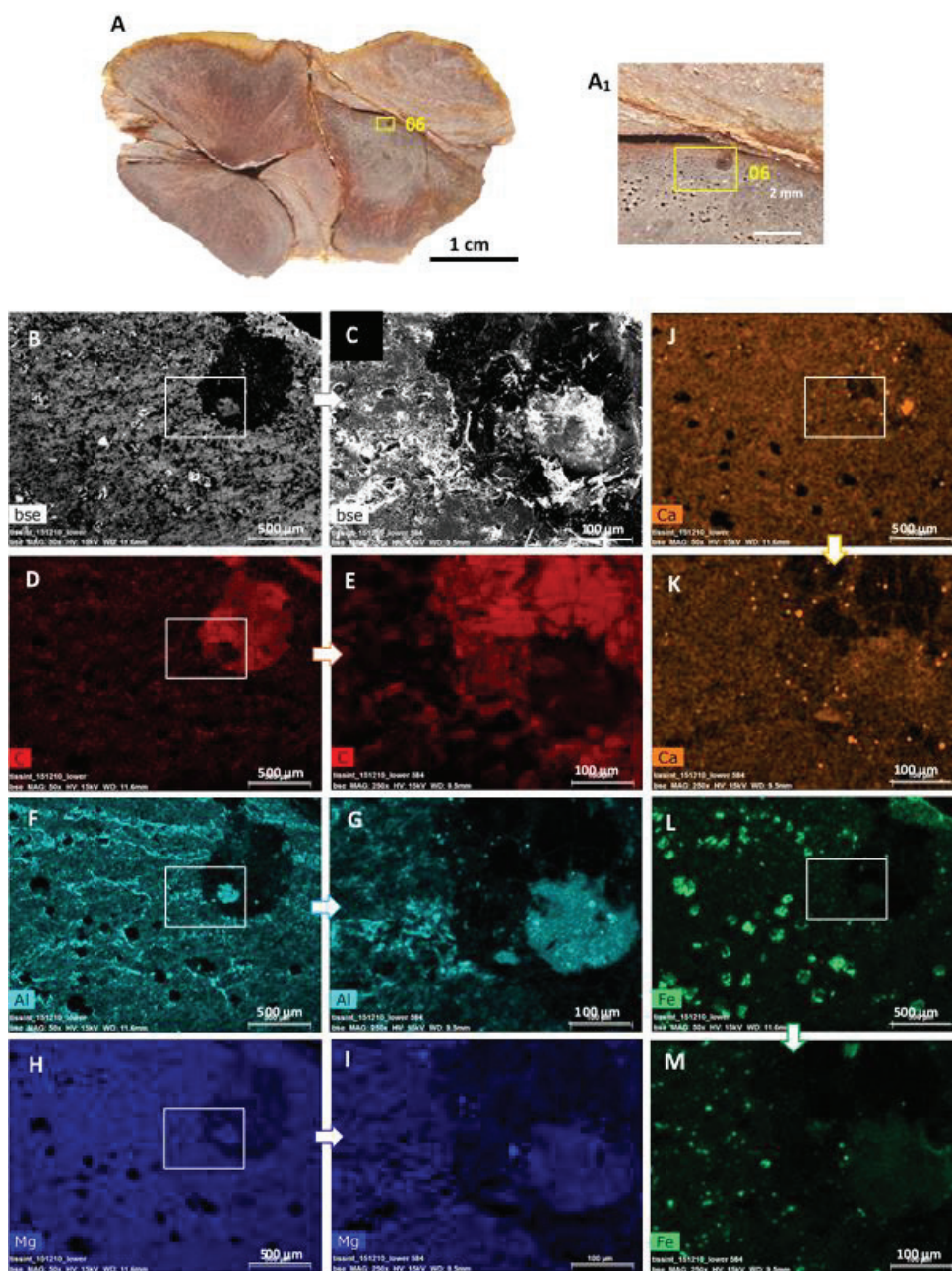


Figure S19: Internal structures of contiguous and deformed nodules of *Akouemma 2nd2*. (A) Zone 6, undeformed cone of the lower hemisphere. (A₁) Macroscopic view of an oblong biomorph approximately 600 μm in diameter embedded in the nodule; note the surrounding scattered dissolution cavities. (B) Mottled grey BSE image showing black and white dots with no clear orientation and an oblong-shaped dark form within which there is a clearer, round zone. (C) Magnification of the box showing a clear zone with a pointed tip surrounded by dark and light zones. (D-E) Carbon distribution maps with magnified image (E) showing an oblong carbon form with a round dark zone at its tip. (F-G) Aluminum distribution maps with magnified image (G) showing no particular organization but displaying curving lines and scattered dark spots; aluminum seems to be present in zones with little or no carbon. (H-I) Magnesium distribution maps with magnified image (I) showing the same configuration as that of aluminum; the magnesium distribution is more homogeneous. (J-K) Calcium distribution maps showing a pervasive distribution of

calcium except in very carbon-rich areas and scattered dark spots. (L-M) Iron distribution maps showing concentrations in dispersed points (probably pyrite dissolution cavities) and secondary concentrations in less carbon-rich areas.

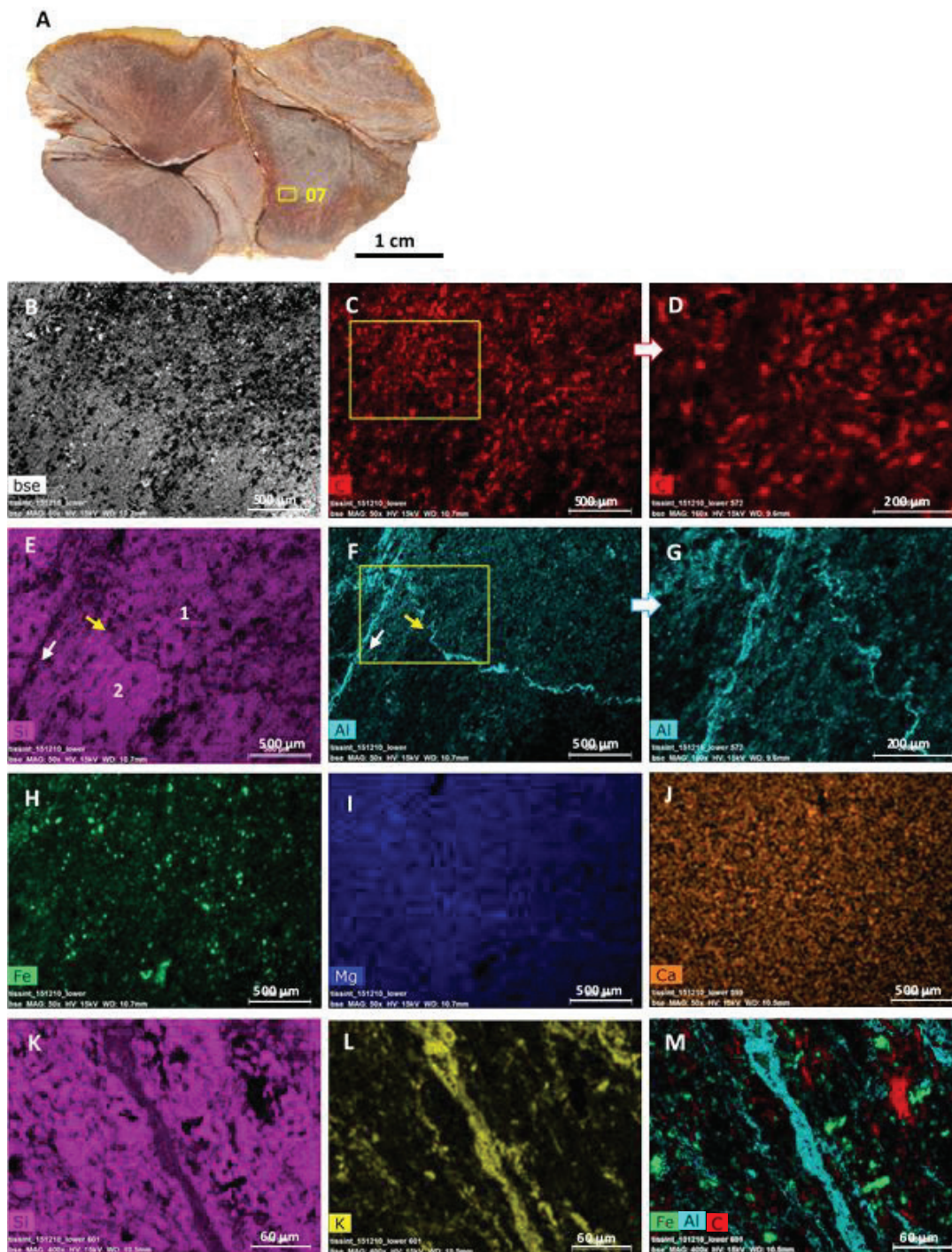


Figure S20: Internal structures of contiguous and deformed nodules of *Akouemma 2nd₂*. (A) Zone 7, undeformed lower hemisphere. (B) BSE image showing a marked oblique direction and a large number of dark particles in the upper half. (C-D) Carbon distribution maps with magnified image (D) showing the arrangement of particles in the same oblique direction as the BSE image. (E) Silicon distribution map showing a lateral line (yellow arrow) that seems to separate ramps 1 and 2 (ramp 1 covers ramp 2) and a linear structure extending in the radial direction (white arrow). (F-G) Aluminum distribution maps with magnified image (G), highlighting the limits of ramp 1 and the linear structure made up of juxtaposed patterns in the radial direction (clearly visible on (G)). (H) Iron distribution map showing the same configuration as the BSE image (B), with a higher particle density in the upper half of the map. (I) Magnesium distribution map; the linear structure extends in the radial direction, whereas the limit of the ramp is barely visible. (J) Calcium distribution map showing no orientation. (K-M) Distribution maps of silicon, potassium, aluminum, carbon and iron in thin section all show the same continuous or particulate linear structures in the radial direction (calcium, aluminum, carbon and iron) and discontinuous particulate structures that intersect in the radial direction (iron).

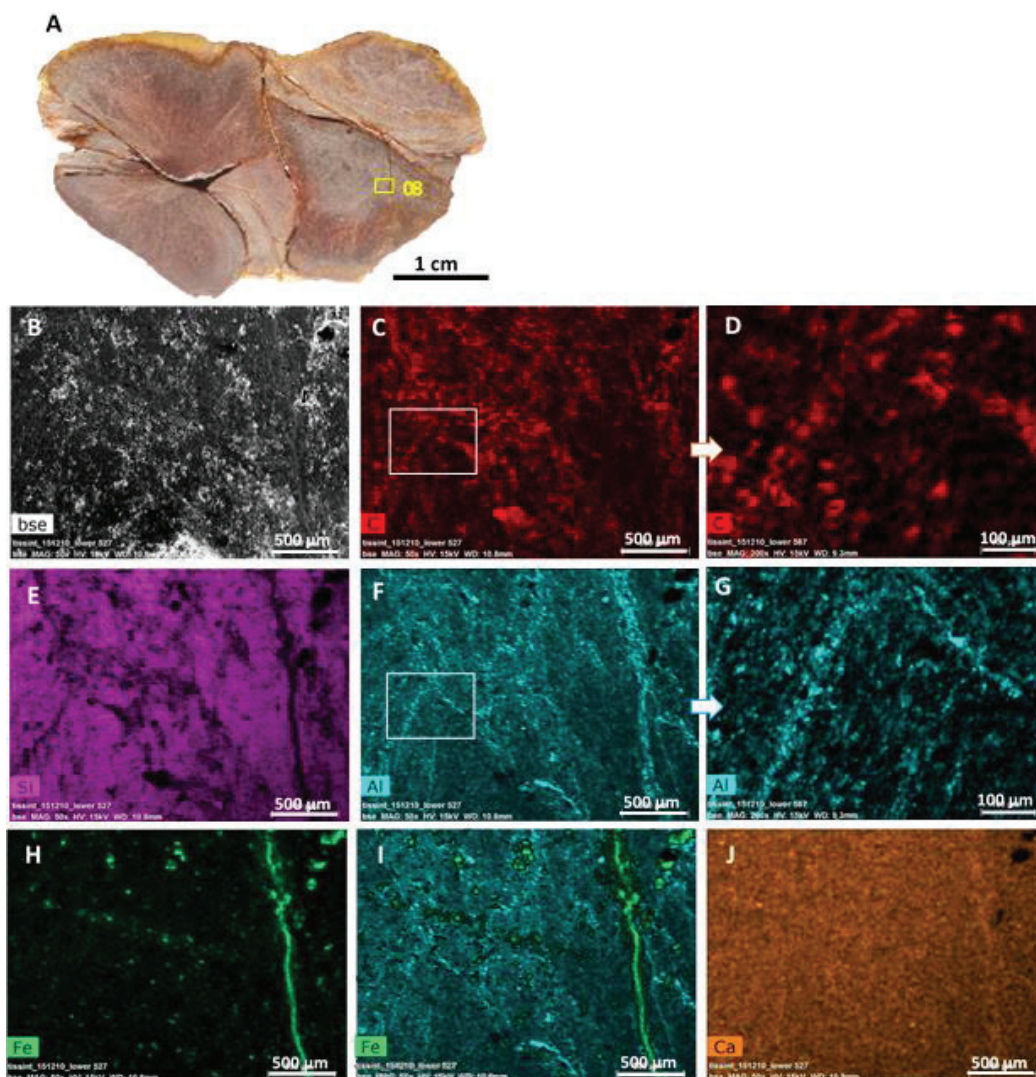


Figure S21: Internal structures of contiguous and deformed nodules of *Akouemma 2nd₂*. (A) Zone 8, partially destructured in the lower hemisphere. (B) BSE image showing curvilinear structures. (C-D) Carbon distribution maps with magnified image (D) showing a corrugated and heckled structure; particle size is approximately 30 μm. (E) Silicon distribution map showing gross curvilinear and linear structures. (F-G) Aluminum distribution maps with magnified image (G) showing these two structures in detail. Note the beautiful ‘folded’ structure associated with thin filaments in (G); this is superimposed on the carbon structure in (D). The thin filaments are parallel to each other and intersect the edges of the ‘folded’ structure; this zone appears to be degraded. (H) Iron distribution map showing a concentration of iron in the linear structure. (I) Superposed aluminum and iron distribution maps showing perfect juxtaposition of the two elements on the linear structure; the distribution of iron particles appears to be independent of the corrugations. (J) Calcium distribution map; the linear structure is only barely visible.

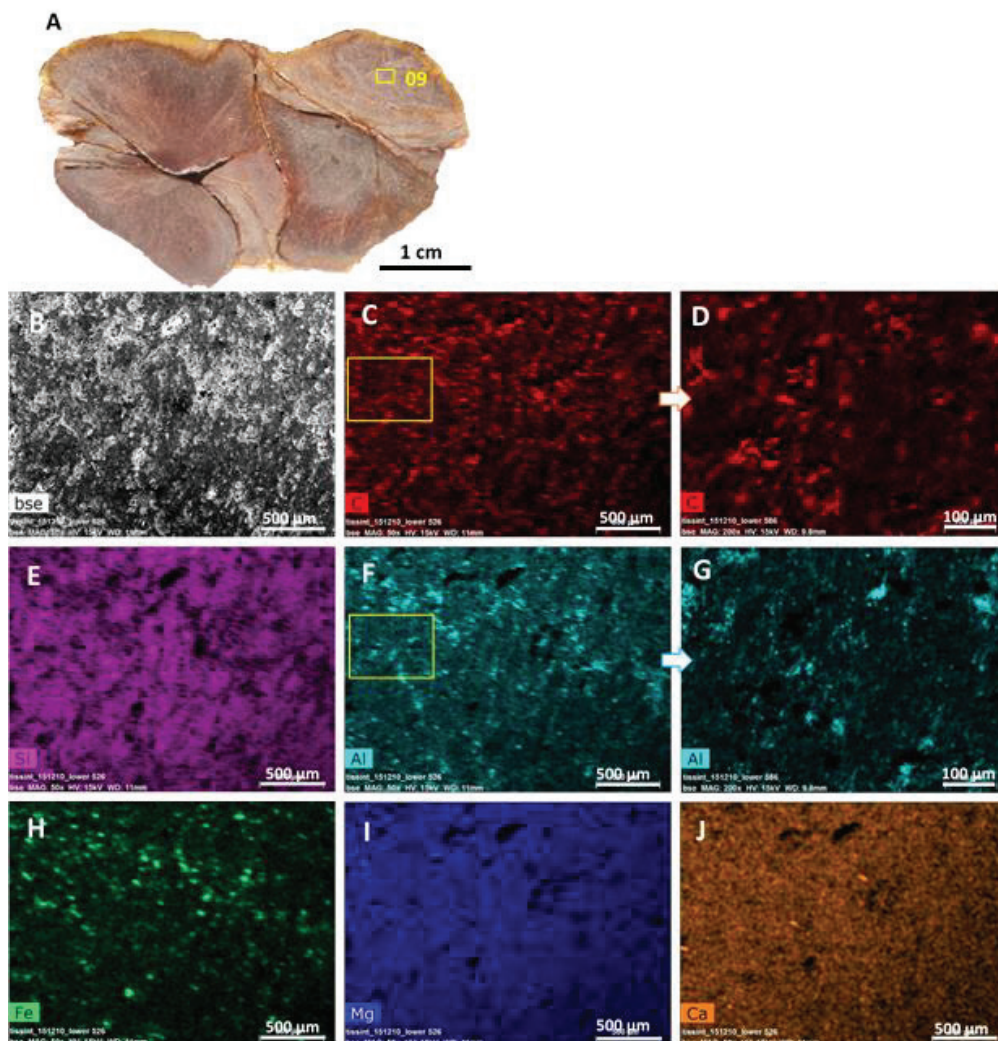


Figure S22: Internal structures of contiguous and deformed nodules in *Akouemma 2nd*. (A) Zone 9, undeformed. (B) BSE image showing an overall oblique orientation of linear structures in the lower half; the structures appear worn in the upper half. (C-D) Carbon distribution maps with magnified image (D) showing an overall particle orientation in the same oblique direction and details of the layout of curved carbon particles. (E) Silicon distribution map showing a complex structure involving transverse corrugated lines suggesting the edges of the flaps and finer lines of carbon particles in the oblique direction. (F-G) Aluminum distribution maps with the same configuration as that of silicon; transverse corrugated lines are discontinuous, suggesting disorganization. The magnified image (G) shows the overall oblique aspect of the structure; note the presence of large particles approximately 300 μm in size at the top of the image. (H) Iron distribution map that has the same general configuration as that of aluminum (F). (I-

J) Distribution maps of magnesium and calcium show a structure far less clearly but highlight large dark particles in an oblique direction.

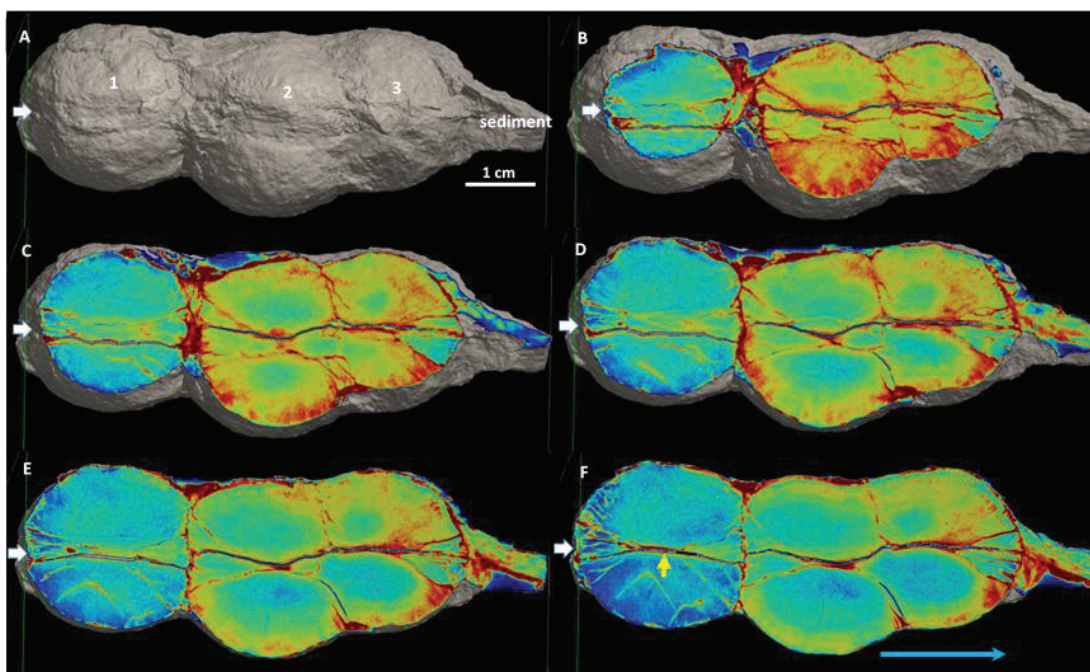


Figure S23: Tomographic views of the 'triple' nodule. (A) Whole. (B-F) Vertical sections from edge to center showing a clear separation between the 'nodule' 1 and the 'nodules' 2 and 3, and an incomplete separation between 'nodule' 2 and 'nodule' 3; Note the evolution of the median disc of the 'nodule' 1 from B to F (white arrow), the communication zone (point) between the two hemispheres appears in (F) (yellow arrow). The blue arrow indicates the growth direction.